PREDICTION OF PAVEMENT SURFACE DETERIORATION

By

Yawen Liu

Thesis submitted to the University of Nottingham

For the degree of Doctor of Philosophy

August 2016

To my parents for their unconditional love and support

Abstract

Prediction of pavement performance is important to pavement engineers. Pavement surface deterioration is a dynamic and complicated process. Moisture damage and fatigue are considered as two major causes of pavement deterioration. During a pavement's service life, the presence of water can lead to loss of stiffness and strength of the asphalt pavement structure. Apart from that, the presence of water can accelerate the propagation and severity of already existing distress. High tensile strain at the bottom of an asphalt layer results fatigue cracking in a pavement.

The goal of this research was to develop a series of computational models to predict pavement surface deterioration under the effects of moisture and traffic. The first task was to calculate the pavement surface water pressure under a moving tyre. The water is compressed underneath the tyres, generating a water pressure pulse. This pressure allows surface water to penetrate into the pavement structure. Then the asphalt pavement internal structure (voids distribution) was determined and the water pressure distribution inside the pavement structure was calculated for both fully saturated and partially saturated condition using the surface water pressure. The water pressure expands the voids inside the pavement. Consequently, stress and strain at the edge of the voids, due to frequent traffic passes can lead to failure of the pavement. A ravelling failure probability line was then predicted with the help of cavity expansion theory and asphalt crack propagation law.

The case study for the performance of four different asphalt types (HRA, SMA, AC, DBM) using the failure probability calculation shows a good correspondence with their real performance which indicates that this process of predicting failure probability is generally acceptable.

Acknowledgement

I would like to thank all the people who have provided their assistance, advice and encouragement without which this research would not have been possible.

First of all, I would like to express my sincere gratitude to my supervisor, Dr. Nick Thom, to whom I am deeply grateful for his guidance and assistance throughout my research period in university of Nottingham. His scholarly advice was essential for this research. This thesis would never have been possible without his guidance and assistance. I am greatly appreciated for his continuous support and I will never forget.

Secondly, I want to express my sincere appreciation to my second supervisor, Professor Gordon Airey for his help and support through my research. His advice and comments were extremely valuable.

I am grateful to all the staff and my colleagues in Nottingham Transportation Engineering Centre (NTEC), for their kindly help and support during my research period.

I would also like to show my special thanks to my parent for their unconditional support, encouragement and love.

Declaration

I declare that the work is my own and has not been submitted for a degree of another university.

Yawen Liu

Nottingham

August 2016

Table of Contents

List of figures

List of tables

Chapter 1. Introduction

1.1 Research Background

The common materials used in road paving throughout the world are asphalt and cement concrete. In the UK, approximately 95% of the roads are surfaced with asphalt mixtures (ITA, 2000). Asphalt is a composite material consisting of aggregates, bitumen and filler. Like any other man-made structures, asphalt pavements deteriorate with the passage of time due to repeated traffic loading and the environment (Cox, 1979). It has been reported that almost 2.8 billion pounds are spent annually by the local authorities in England and Wales for road maintenance and rehabilitation works (ALARM, 2016).

There are different types of pavement surface deterioration such as rutting, fatigue cracking, ravelling, potholes etc. These forms of distress, particularly potholes, are signs of advanced-stage road deterioration in many cases. Over recent years, the development of potholes in roads has accelerated considerably within the UK and worldwide, leading to serious concern and wide media coverage. It has been reported that an estimated 1 in 10 mechanical failures on UK roads are caused by potholes (potholes.co.uk). According to the Annual Local Authority Road Maintenance (ALARM) Survey commissioned by the Asphalt Industry Alliance (AIA), the overall number of potholes reported in 2015 was around 2.2 million. The average cost to fill a pothole was £64 and the

total amount spent on filling potholes across England and Wales was £118 million (ALARM, 2016). The significant increase in the number of potholes on the already fragile local highway network has resulted in further deterioration and created a significant maintenance problem for local highway authorities (Baker, 2012). And if potholes are left unrepaired or with poor repair, this will not only have a longer term effect on the condition of the network and accelerate deterioration but also affect the road users and the surrounding community.

It is generally accepted that moisture damage is one of the major causes of pothole formation as well as other pavement surface distress. Due to the wet climate in the UK, distress and deterioration in a large number of pavements are the result of moisture damage. Ravelling is one phenomenon of pavement distress due to moisture damage which is quite likely to cause pothole formation. Another factor that may cause potholes is fatigue. Fatigue in bituminous pavements is a phenomenon of cracking (alligator cracking, block cracking, longitudinal cracking and transverse cracking). Severe alligator cracking can result in potholes. At this stage, scientists can describe the causes of potholes in general terms but the detailed mechanism is not very clear. Hence improving engineering understanding of pothole behaviour mechanisms including initiation and distress development is necessary.

1.2 Problem statement

Since potholes are now one of the public's main local concerns, as they are highly visible defects (Baker, 2012), specific research directly relating to pothole formation and the mechanisms which result in their initiation and progression needs to be carried out.

As mentioned previously, two main causes of pothole formation are moisture damage and fatigue cracking. However pavements are all under different ground condition support and with varied geological and climatic conditions. Potholes, therefore, occur for a variety of reasons and with the current state of knowledge it would be unreasonable to predict their occurrence or compute any specific pavement life before their occurrences. However it is necessary to have a common method to predict the formation of potholes and other surface deterioration. As a consequence, some indirect predictions can be attempted.

In this research, ravelling will be predicted as an early sign of pothole formation under the combination of moisture and fatigue influence. Different variables (i.e. voids size distribution) need to be minimised to obtain a common prediction procedure.

This research will study the stress and strain characteristics within a pavement structure in order to describe the effects of the two stated failure causes (moisture and fatigue). Considering a vehicle passing on a pavement in the presence of a certain thickness of water film on the

surface, the water is compressed underneath the tyres, generating a water pressure pulse. This pressure allows surface water to penetrate into the pavement structure which then expands the voids inside the pavement. Consequently, stress and strain at the edge of the voids, due to frequent traffic passes can lead to failure of the pavement.

1.3 Research aim and objectives

The main purpose of this research is to predict the pavement surface deterioration under moisture and traffic conditions. As mentioned before, moisture damage is one of the major causes of pavement surface distresses. With the repeated traffic loading over time, pavement surface distress will form and propagate. This process will be accelerated with the presence of water. The objectives set out below are the steps that are required for the development of the overall aim and the overall success of the project.

- Literature review based on the existing research to understand the mechanisms of moisture damage including loss of bitumen-aggregate adhesion and bond strength between layers and fatigue characteristics.

- Monitor real sites near/in the University Park to have a better understanding of real deteriorations on the pavement surface.

- Create a series of computer models to predict the distress of a pavement under different conditions. Firstly, the water pressure

generated by a moving tyre is calculated with three kinds of pavement surface models. Then a simplified pavement internal structure is designed and the water pressure distribution is calculated using the surface water pressure. After that the bond stress between bitumen and aggregate and between two layers is calculated. Finally, the cavity expansion theory and asphalt cracking propagation law are used to predict the probability to failure for an asphalt pavement.

1.4 Thesis organisation

In order to achieve the main aim of this research, the objectives stated above have been tackled and the thesis is separated into 7 chapters.

Chapter 1 has briefly introduced the background of pavement surface deterioration and modelling to analyses the combined influence of moisture and fatigue. The organisation of the final thesis is also presented in this chapter.

Chapter 2 reports on an overall literature review on moisture induced damage including loss of bitumen-aggregate adhesion and bond strength between layers and fatigue damage (cracking) of asphalt pavements.

Chapter 3 presents real time pavement performance observations and indicates a strong relationship between pavement surface deterioration and both moisture and traffic effects.

Chapter 4 describes the first step in the prediction of surface deterioration which is to calculate the surface water pressure due to traffic (tyre movement) and compares the effect of different input parameters i.e. vehicle speed, tread width and pavement surface roughness for three kinds of pavement surface.

Chapter 5 presents designs for a simplified pavement internal structure to analyse the water pressure distribution within the pavement. Both saturated and partly saturated voids are considered.

Chapter 6 develops a simplified stress calculation for loss of bitumen-aggregate adhesion and de-bonding between two layers. An asphalt cracking propagation law is used to predict the surface failure probability of an asphalt pavement.

Chapter 7 outlines the conclusion of this study and the recommendations for future work.

Chapter 2. Literature Review

The purpose of this chapter is to review the literature on moisture damage and fatigue characteristics for asphalt pavements. The first part introduces the background of asphalt pavements. The second part presents a review on moisture damage which consists of moisture damage mechanisms and loss of adhesion at the aggregate bitumen interface. After that the de-bonding between two layers is described. The last part contains approaches to characterise fatigue and the factors that affect fatigue in asphalt.

2.1 Types of asphalt pavement

A road pavement is a structure consisting of multiple layers of processed materials above a natural soil sub-grade. Generally speaking, the main function of the pavement is to spread out the load on the surface and decrease the tyre contact stress on the sub-grade to a tolerable level such that it can withstand load without deforming. And also the pavement structure should be able to deliver a surface of standard riding quality, adequate skid resistance, positive light reflecting characteristics and low noise pollution (Tom and Krishna Rao, 2007)

There are different types of pavement that are used in the construction of roads. The different pavements are classified into two main categories based on their structural performance and layer structure. They are rigid pavement and flexible pavement. The wearing course of a rigid pavement

is usually made of Portland Cement Concrete (PCC), a base course directly under the surface and above a sub-base course. The PCC acts as a slab over the underlying supporting material to give the rigid pavement a higher resistance to deflection under traffic loading. On the other hand, a flexible pavement consists of a bituminous surface wearing course underlain with a layer of granular material (Garber and Hoel, 2014). The wheel load stresses can therefore be transmitted to the lower layers by grain-to-grain transfer through the points of contact in the granular structure.

Hot Mix Asphalt (HMA) is a common type of flexible pavement material used worldwide. Based on the design and production methods, HMA can also be divided into three types. They are Dense-Graded HMA, Stone Matrix Asphalt (SMA), and Open-Graded HMA.

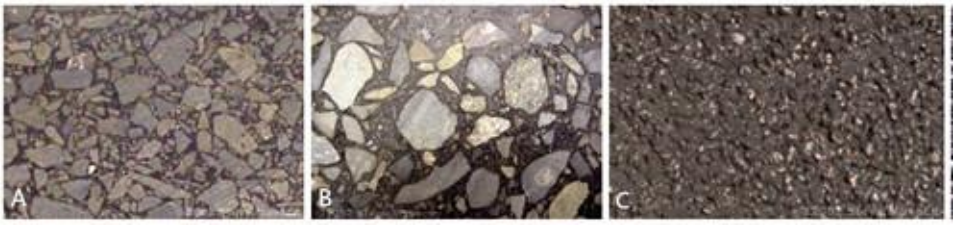

Figure 2-1 Different asphalt pavement surfaces: A) Dense-Graded HMA; B) SMA; C) Open-Graded HMA (Tom and Krishna Rao, 2007)

2.1.1 Pavement distress types

Pavement design is aimed at developing the most economical combination of pavement layers to suit the soil foundation and provide the required strength quality under traffic environmental loading during the design life. Properly designed pavements can provide many years of satisfactory

service, however pavements can still be damaged under certain conditions. A localized settlement of any one component layer of a flexible pavement structure could be enough to cause pavement failure. Flexible pavements can suffer from several categories and subcategories of distress that will lead to progressive deterioration of ride condition, structural strength, and motorist/pedestrian safety (Sorumet al. 2013). The different types of pavement distress are listed in Table 2.1 below.

Table2-1 Types of pavement distresses (Sorumet al. 2013)

Type of failure	Description
Fatigue (alligator) cracking	Series of interconnected cracks caused by fatigue failure under repeated traffic loading
Bleeding	Film of asphalt binder on the pavement surface
Block cracking	Interconnected cracks that divide the pavement up into rectangular blocks (approx. 0.1 m2 to 9 m2)
Corrugation and shoving	A form of plastic movement typifiedby ripples(corrugation) or an abrupt wave (shoving) across the pavement surface
Depression	Localized pavement surface areas with slightly lower elevations than the surrounding pavement
Joint reflection cracking	Cracks in a flexible overlay of a rigid pavement which occur directly over the underlying rigid pavement joints
Longitudinal cracking	Cracks parallel to the pavement's centerline or laydown direction (a type of fatigue cracking)
Patching	An area of pavement that has been replaced with new material to repair the existing pavement
Polished aggregate	Areas where the portion of aggregate extending above the asphalt binder is either very small or there are no rough or angular aggregate particles

Potholes	Small, bowl-shaped depressions in the pavement surface that penetrate all the way through the HMA layer down to the base course
Raveling	The progressive disintegration of an HMA layer from the surface downward as a result of the dislodgement of aggregate particles
Rutting	Surface depression in the wheel path
Slippage cracking	Crescent or half-moon shaped cracks generally having two ends pointed into the direction of traffic
Stripping	The loss of bond between aggregates and asphalt binder that typically begins at the bottom of the HMA layer and progresses upward
Transverse (thermal) cracking	Cracks perpendicular to the pavement's centerline or lay down direction is usually a type of thermal cracking
Water bleeding and pumping	Water bleeding occurs when water seeps out of joints or cracks or through an excessively porous HMA layer. Pumping occurs when water and fine material is ejected from underlying layers through cracks in the surface

2.2 Moisture sensitivity of asphalt

It has long been recognised that water is the worst enemy of asphalt pavements and it can influence both the physical and mechanical properties of the asphalt. The presence of water (or moisture) often results in two basic forms of premature failure of pavements. One of them is adhesion failure which is isolated distress caused by de-bonding of the bitumen film from the aggregate surface, and the other is cohesion failure

which means early rutting/fatigue cracking due to reduced mixture strength (Lu and Harvey, 2007).

Moisture sensitivity of asphalt has been investigated by numerus researchers in the past few decades. Most of them consider that moisture damage due to adhesion failure is more significant than that due to cohesion failure. This is manifested as stripping of the bitumen from the aggregate in the presence of water (Majidzadeh and Brovold, 1968). Kennedy et al. (1982) explained that stripping was the loss of adhesion between the asphalt binder and the aggregate due to the action of water, and Tunicliff and Root (1982) used the chemical reaction theory of adhesion to explain that stripping was the displacement of the asphalt binder film from the aggregate surface. Hefer et al. (2005) used four theories to explain bitumen-aggregate adhesion; they are: thermodynamic theory, electrostatic theory, mechanical theory and chemical bonding theory.

Thermodynamic theory

Thermodynamic theory is based on the concept that an adhesive will adhere to a substrate due to established intermolecular forces at the interface provided that intimate contact is achieved. The magnitudes of these fundamental forces can generally be related to thermodynamic quantities, such as surface free energies of the materials involved in the adhesive bond or the Gibbs free energy of the system.

Electrostatic theory

Solid surfaces can be characterized as electropositive or electronegative due to the assembly of atoms and the consequent formation of molecular dipoles. A charged aggregate surface attracts an oppositely charged or partially charged species of bitumen. The part of the attracted bitumen molecule is then available to attract other oppositely charged bitumen molecules through electrostatic interaction.

Mechanical theory

Mechanical adhesion theory involves the mechanical gripping of the adhesive into the cavities, pores and asperities of the solid surface on a macroscopic scale and it has been realised as the most intuitive adhesion phenomenon (Schultz et al., 1994). This theory assumes that the bitumen is forced into the irregularities of the aggregate surface, producing a mechanical interlock.

Chemical bonding theory

The chemical reaction is based on the premise that acidic and basic components of both bitumen and aggregate react to form water-insoluble compounds that resist stripping. During mixing, hot bitumen with a low viscosity coats the aggregate surface and tends to enter any available crevice or pore. When in contact with the aggregate surface, the short-range chemical interactions of bitumen are feasible because of

electrostatic interactions between the charged aggregate surface and the molecules attracted to the surface.

However researchers such as Kanitpong and Bahia (2003) have suggested that the probability of cohesive failure was much greater than that of adhesive failure by observation of the failure surface which showed no evidence of apparent loss of adhesion between bitumen and aggregate through the Tensile Strength Ratio (TSR) test.

2.2.1 Moisture Sensitivity Tests

In order to avoid premature failure caused by moisture in the road pavement, numerous laboratory tests have been developed over the years in an effort to predict the moisture sensitivity of an asphalt mixture. These tests examine the effect of moisture on the mix strength or the coating on the aggregate generally.

In general, there are two kind of moisture sensitivity test: tests on loose coated aggregate and tests on compacted aggregate. Tests on loose coated aggregate normally consist of immersing bitumen coated asphalt mixtures in water for a certain period of time under static or dynamic conditions at room or high temperature. And then the results are visually assessed by determine the percentage of bitumen remaining on the aggregate surface. Generally speaking, these tests are easily performed. The Rolling Bottle Test (RBT) and Boiling Water Test (BWT) can be in general agreement with the surface energy-based test results compared

to other tests (Liu et al., 2014). However they are not meaningful enough to explain the actual moisture damage mechanisms and are hard to correlate with field performance. The tests on compacted mixtures usually condition laboratory or cored asphalt samples in water to measure the mechanical property changes in the samples before and after immersion in water. There are two categories of test on compacted mixtures: immersion mechanical tests and immersion wheel tracking tests. The immersion mechanical tests measure the change of mechanical properties such as indirect tensile stiffness and indirect tensile strength of the mixture after immersion in the water for a certain period. However, none of these immersion mechanical tests consider the effect of trafficking. Therefore the immersion wheel tracking test was developed to overcome this problem. Nevertheless, none of the tests on compacted asphalt mixtures are totally reliable in terms of correlation with the field (Airey et al., 2002). Both laboratory tests for loose coated aggregate and compacted asphalt mixtures are listed in Table 2.2 below.

Table 2-2 Testing methods on loose coated aggregate and compacted asphalt mixtures

TESTS ON LOOSE COATED AGGREGATE	**TESTS ON COMPACTED ASPHALT MIXTURES**	
Static Immersion Test (AASHTO T182, ASTM D1664)	**Immersion Mechanical Tests**	**Immersion Wheel Tracking Tests**
Dynamic Immersion Test (Whiteoak, 1991)	Texas Freeze-Thaw Pedestal Test (Airey et al., 2002)	Immersion Wheel Tracking Test (Mathews et al., 1962)
Chemical Immersion Test (by use of sodium carbonate) (Whiteoak, 1991)	Immersion Compression Test (AASHTO T165, ASTM D1075)	Hamburg Wheel Tracking (Aschenbrener, 1995)
Rolling Bottle Method (Cen prEN 12697-11)	Marshall Stability Test (AASHTO T245)	
Boiling Water Test (ASTM D3625)	Duriez Test (NFP 98-251-1)	
Ancona Stripping Test (Bocci et al., 1993)	Lottman Test (Lottman, 1982)	
Boiling Water Stripping Test (Choquet et al., 1993)	Tunnicliff and Root Procedure (Tunnicliff et al., 1984)	
Ultrasonic Method (Vuorinen et al., 1999)	Modified Lottman Procedure (AASHTO T283)	
Net Adsorption Test (SHRP, M001)	LINK Bitutest Water Sensitivity Protocol (Airey et al., 2002)	
Modified Net Adsorption Test (Walsh et al., 1996)		

2.3 Moisture mechanical damage

Moisture related damage does not occur without the presence of water and traffic. Sources of moisture in an asphalt pavement can be either internal or external. The water left in inadequately dried aggregate could be one common internal source of moisture (Santucci, 2002). Warm mix technologies can also produce moisture in the form of steam by water

contacting with hot bitumen (Read & Whiteoak, 2003). The external source of moisture is mainly caused by the poor drainage of characteristics of the mixture. Moisture can enter the pavement from the surface, sides and from beneath the sub-grade. Moisture comes from rain infiltration or from beneath the surface.

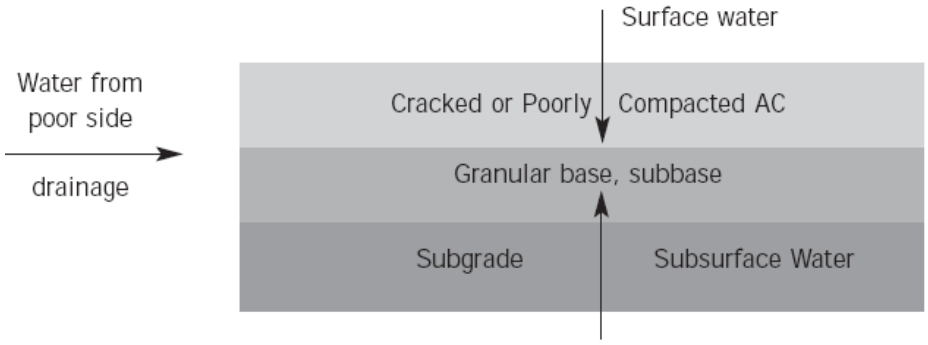

Figure 2-2 Sources of Water in an Asphalt Pavement (Santucci, 2002)

Once the moisture is in the pavement, infiltration of moisture into the asphalt mixture can break the bitumen aggregate adhesive bonds and cause cohesive failures. As shown in Figure 2.3, moisture typically reduces the stiffness of the binder and/or mastic through moisture diffusion, and degrades the adhesive bonding between the binder/mastic and aggregate particles.

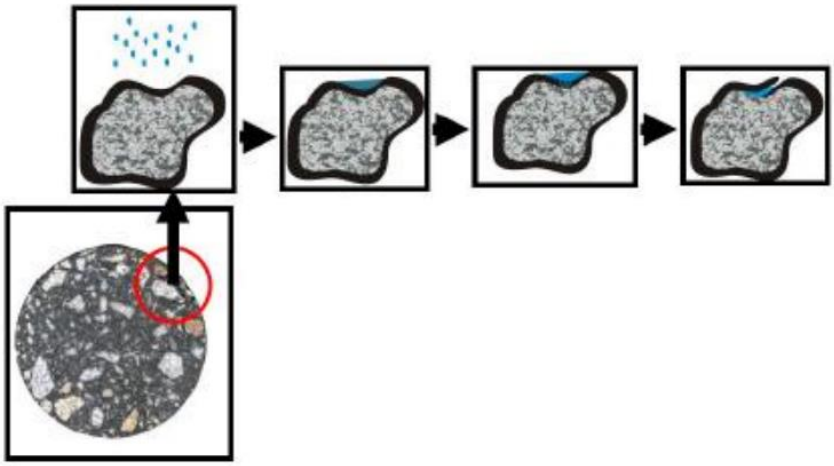

Figure 2-3 Illustration of moisture damage mechanisms (Kim and Lutif, 2006)

The moisture damage occurs when pavement materials are subjected to traffic loads and the repeated expansion and contraction effect of temperature in the presence of water. Once water is present, there are three ways it may influence an asphalt mixture: (i) a flow field, (ii) static water, and (iii) water present in aggregates (Kringos, 2005). If a flow field is present, water may wash away the mastic, weaken the binder, and cause a decrease in the cohesion and in mixture stiffness, incurring damage to the road. Static water gradually penetrates into the asphalt and aggregate interface and thus easily causes a reduction of adhesion between asphalt binder and aggregate surface. Wet aggregates become an issue if the aggregates are not thoroughly dried during mixture production (Copeland, 2007).

Apart from the physical water mechanical damage, moisture damage is also the result of traffic loads and hydrodynamic pressure. The "pumping action" caused by hydrodynamic pressure due to continuous traffic loading (Kandhal, 1992, 1994; Kiggundu, 1988; Taylor and Khosla, 1983)

can interact with the already present "mechanical damage". When some of the macro-pores in an asphalt pavement are saturated, fast traffic loads will locally cause intense water pressure fields in these pores. These pore pressures contribute extra stresses within the asphalt mixtures which then accelerate the deterioration of the pavement leading to an increased "water mechanical damage" by transporting or pumping as shown in Figure 2.4 (Kringos, 2007).

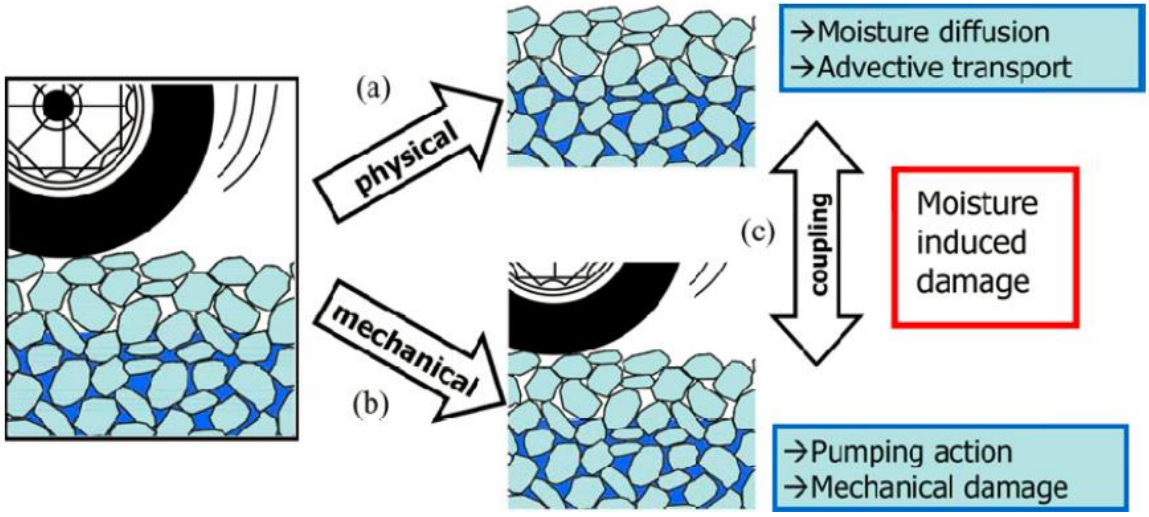

Figure 2-4 Separation of Water Damage into Physical and Mechanical Progresses (Kringos, 2007)

Repeated freeze–thaw cycles can also accelerate the distress in the pavement. Water is very easy to freeze or thaw with temperature change. If water penetrates and remains in the pavement, then the pavement would face the action of water freeze thaw cycles. The freeze thaw process generates tensile stress in the pavement structure and can create cracks, which propagate through the structure with each freeze thaw cycle. The vulnerability of the pavement depends on the characteristics of

the material, such as its condition and the permeability. In addition, frost heave freezing draws up water from the sub base increasing the amount of water in the pavement. Freezing of a pavement takes place from the surface downwards, drawing water up from lower levels (Biczysko et al., 2010; Kringos et al., 2007). Figure 2.5 shows the pothole formation due to freeze draw cycles.

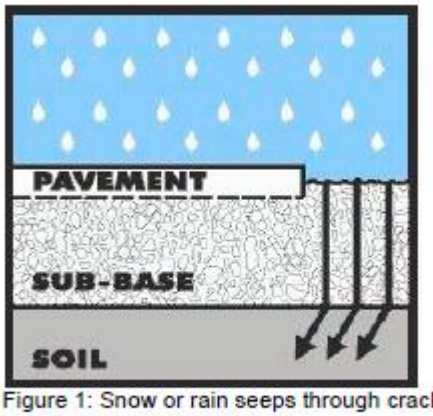

Figure 1: Snow or rain seeps through cracks within the pavement surface

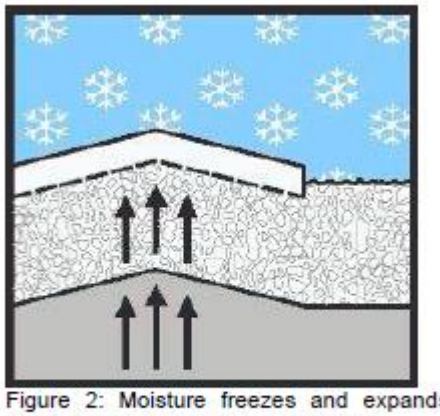
Figure 2: Moisture freezes and expands when the surface temperature drops, causing the pavement to rise up

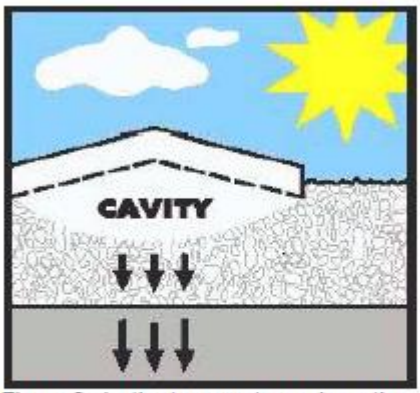

Figure 3: As the temperatures rises, the ground returns to normal level but the pavement often remains raised, creating a gap between the pavement and ground below it

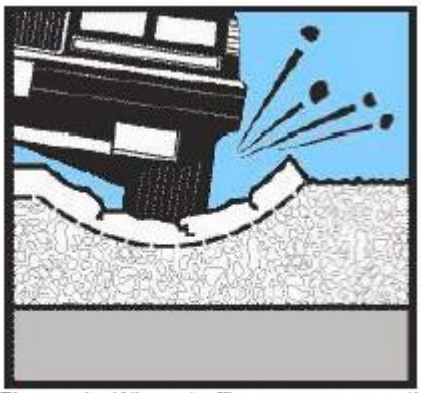
Figure 4: When traffic passes over this cavity, the pavement surface cracks and fails under traffic loading creating a pothole

Figure 2-5 The birth of a pothole; only in climates with significant frost penetration (MDOT, 2011).

In addition to the two primary mechanisms (cohesive failure of asphalt films and adhesive failure of asphalt-aggregate interfaces), other phenomena, such as displacement, detachment, and pore pressure build

up, are some of the effects in a moisture attacked pavement that lead to adhesive and cohesive failure of the asphalt (Lytton et al. 2005).

2.3.1 Moisture induced damage

There are four types of pavement distress that are directly caused by moisture damage: stripping, corrugations, ravelling and weathering together with water pumping (Naveed, 2011).

Stripping and/or ravelling (as shown in Figure 2.6) are the two processes associated with an asphaltic pavement subject to excess water and weakening of the pavement structure leading to pothole formation/progression. Stripping is identified as due to an adhesive failure between the bitumen film and aggregate surface resulting in de-bonding and with continued traffic loading aggregate tends to be displaced from the pavement surface. Stripping converts a high strength asphalt treated pavement layer to a much weaker untreated aggregate material. When it occurs in isolated spots throughout the pavement, it can rapidly develop into potholes (Naveed, 2011).

Figure 2-6 Moisture induced damage in asphaltic pavements. (a) Stripping, (b) Raveling, (c) Pothole formation (Kringos et al., 2007).

Probably the most damaging and often hidden effect of moisture is associated with reduced pavement strength (Naveed, 2011). High vertical compressive stress in a moisture-damaged pavement can result in overstressing of the underlying pavement layers and ultimately can create excessive permanent deformation or rutting in the wheel paths on the pavement surface. Higher tensile (bending) strains at the bottom of the treated pavement layer can translate into earlier than expected fatigue failure as shown in Figure 2.7.

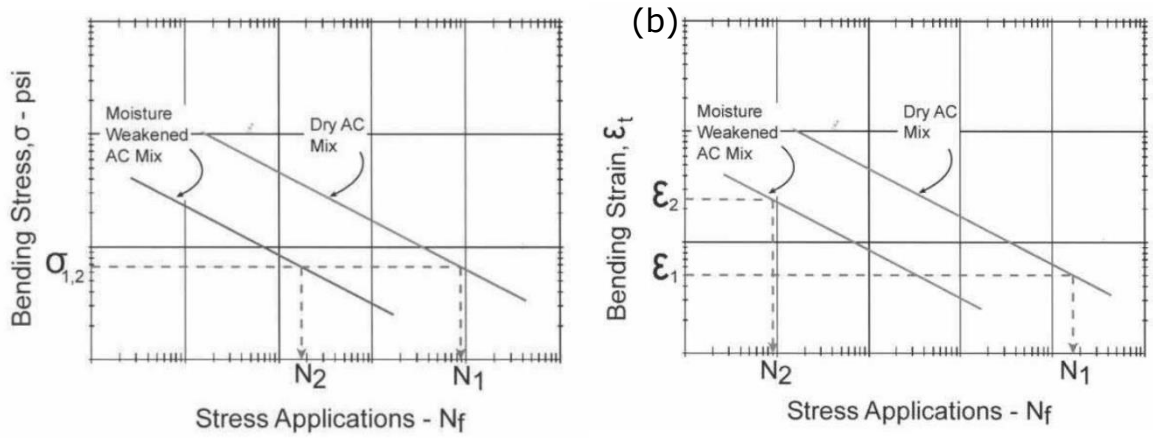

Figure 2-7 Moisture-related distress effect on fatigue: (a) σ versus N_f; (b) ε versus N_f (Santucci, 2002) where σ is the bending stress; N_f is the stress application number and ε is the bending strain

2.3.2 Loss of adhesion at aggregate bitumen interface

As discussed in the previous section, the bond strength between aggregate and bitumen plays a very important role in the behaviour of an asphalt mixture and its moisture susceptibility. With the presence of water, the bond strength will deteriorate over the moisture 'conditioning' time (Kringos, 2007). Several test techniques have been developed to measure the adhesive bond strength between bitumen and aggregate. The most commonly used methods are pull-off tests and peel tests which have been successfully used to evaluate the moisture sensitivity of the aggregate-bitumen bond by immersing specimens in water for a period of time before testing (Zhang, 2015)

Zhang et al. (2015) used three different mechanical tests to quantify the damage that occurred at the aggregate-bitumen interface with different

bitumen and aggregates. They found that for most of the aggregate–bitumen bonds, failure surfaces transformed from cohesive to adhesive with conditioning time thereby confirming the strong influence of moisture on aggregate bonds (Zhang et al. 2015). Figure 2.8 presents the effect of moisture conditioning time on tensile strength using pull-off test.

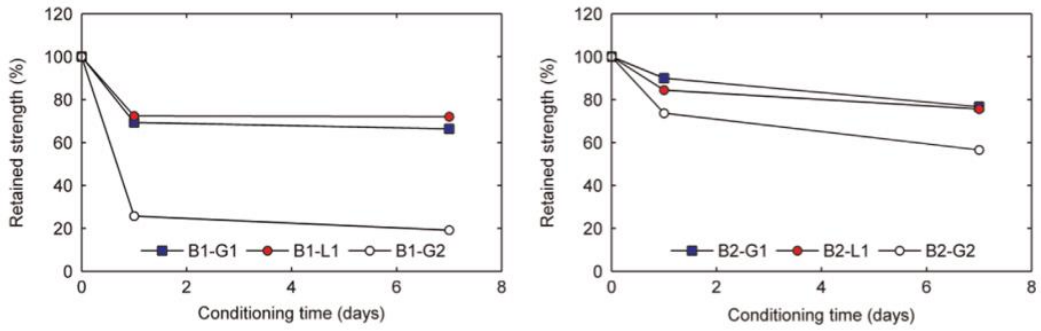

Figure 2-8 Effect of moisture conditioning time on tensile strength of different aggregate-bitumen combination. B1=40/60 pen bituminous binder; B2=70/100 pen bituminous binder; G1=granite aggregate 1; G2= granite aggregate 2 (Zhang et al. 2015)

Kringos (2007) combined the experimental results from a direct tension test and moisture infiltration simulations using the finite element tool Ravelling of Asphaltic Mixes (RoAM) to determine the bitumen-aggregate bond strength as a function of moisture content at the interface. The direct tension test gives the degradation of bond strength versus moisture conditioning time, Figure 2.9 (a), and the simulation with RoAM gives the moisture content in the interface region over time, Figure 2.9 (b), the combination of the two curves gives the wanted relation, i.e. the bond strength degradation as a function of moisture content in the interface, Figure 2.9 (c).

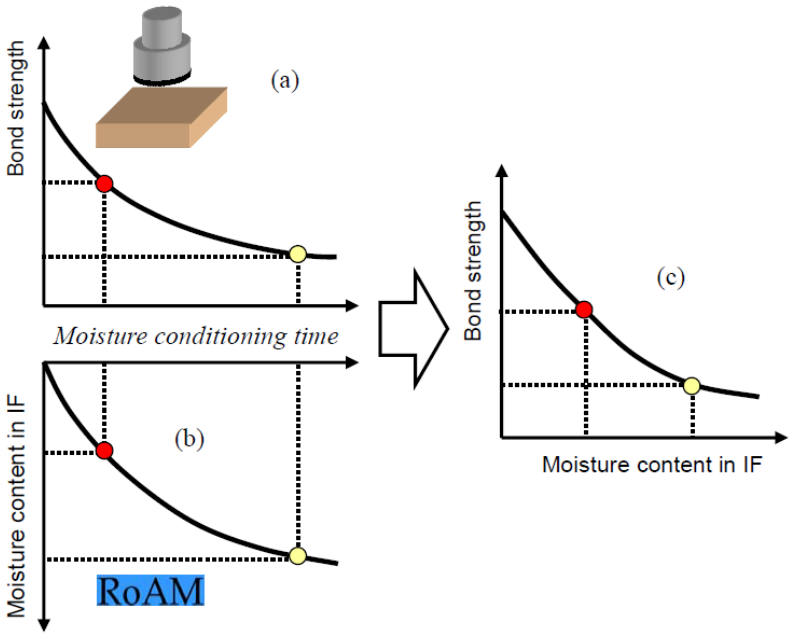

Figure 2-9 Methodology overview: (a) Experimental results (b) RoAM simulations (c) Bond strength as a function of moisture content

After analysing 9 specimens, she confirmed that moisture at the interface reduces bitumen-aggregate bond strength and the relationship (see Figure 2.10) between bitumen-aggregate bond strength and moisture content was determined as:

$$S_{if} = e^{(0.3-3.76\sqrt{\theta})} \qquad \text{Equation 2-1}$$

where S_{if} is the bitumen-aggregate bond strength; θ is the moisture content.

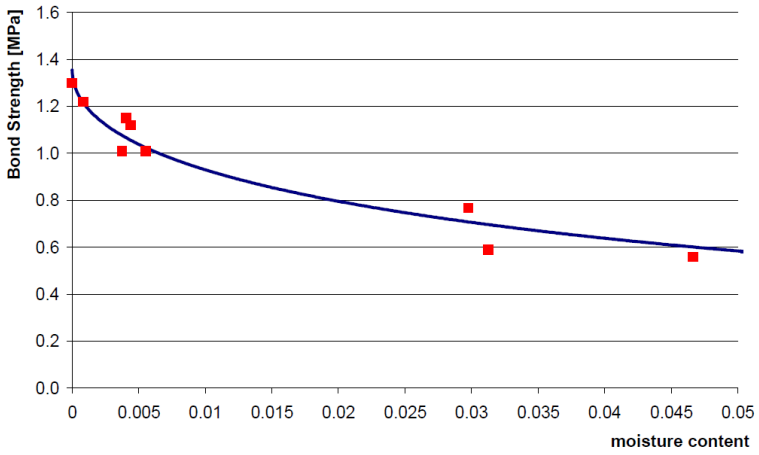

Figure 2-10 Relationship between interface strength and moisture content (Kringos, 2007)

2.3.3 Pore water pressure in the asphalt

As is known, asphalt pavement material is heterogeneous and it consists of aggregates, air voids, and bitumen binder. Therefore, the internal structure as well as the strength of asphalt pavement can be influenced by aggregate gradation and shape, degree of compaction and bitumen binder. Monismith (1992) has proved that the internal structure plays an important role in the resistance of asphalt concrete pavements to major pavement distress types including rutting, fatigue cracking, thermal cracking, and low temperature cracking. This is because moisture diffuses through the solid asphalt skeleton or flows through its interconnected cracks and voids under traffic load. These combined actions induce extra stress due to the pore water pressure.

Wang (2016) used a piezoresistive pressure transducer to measure the pore water pressure at the interface of the upper layer and mid-surface layer in a saturated asphalt pavement in the field. He tested the pore

water pressure under four different vehicle velocities (20km/h, 40km/h, 60km/h and 80km/h) and found that the pore pressure shows periodic damping and normally has two to three prominent cycles. The maximum pore pressure increased as the vehicle velocity increased, with a power law dependence. The maximum positive pressure value was much higher than the negative pressure value.

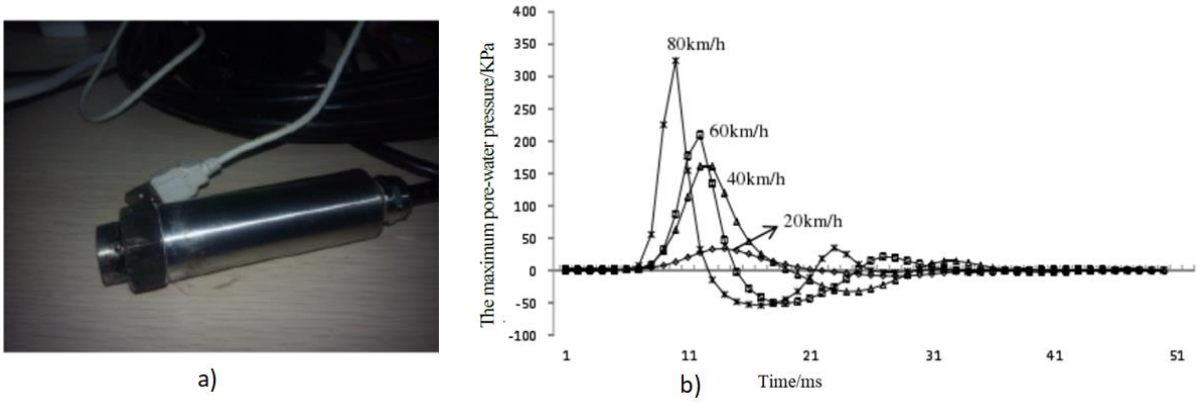

Figure 2-11. a) The piezoresistive pressure transducer used in the test; b) the pore water pressure under different vehicle velocities (Wang, 2016)

Cui et al. (2008) used the finite element tool ANSYS to predict the behavior of a multi-layered saturated asphalt pavement in response to moisture-loading coupled action. They applied a sinusoidal load to simulate the driving load, the maximum circular uniformly distributed vertical stress was is $P_{max} = 0.7MPa$ and the vehicle velocity was 90km/h. They found that in the surface structure of a saturated asphalt pavement, the change of pore-water pressure is large and the change trend is a sinusoid, the positive and negative change of pore-water pressure causing

pavement reciprocal scour and extrusion and making asphalt mixture bonding strength susceptible to lose which may lead to pavement damage.

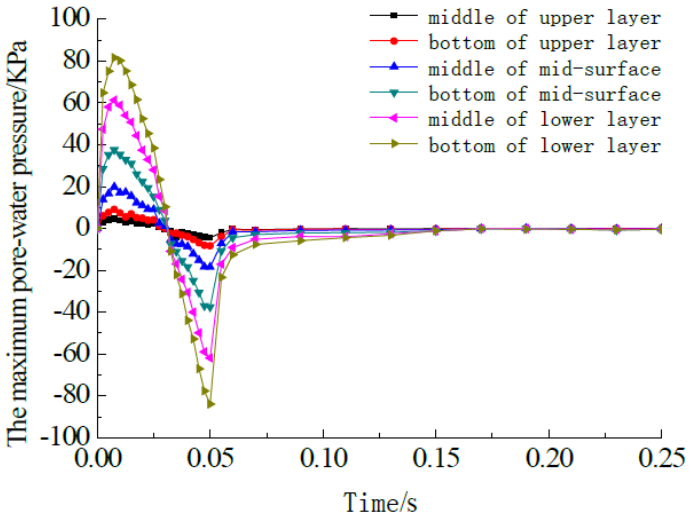

Figure 2-12. The history curves of the maximum pore-water pressure under traffic load (Cui et al., 2008)

Wei (2012) also confirmed a similar conclusion to that of Cui et al. (2008). He used the finite element tool ABAQUS to simulate 3 asphalt pavement specimens: SMA, AC1 and AC2. He applied the same sinusoidal load with a maximum circular uniformly distributed vertical pressure $P_{max} = 0.7MPa$, but the vehicle velocity was 100km/h.

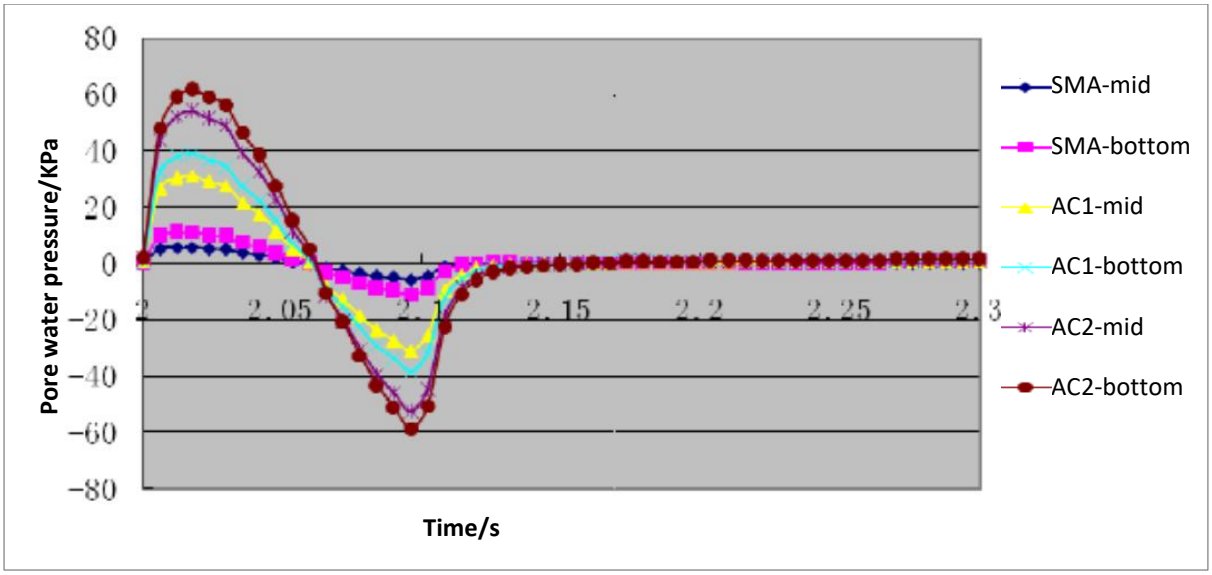

Figure 2-13. maximum pore water pressure for different asphalts (Wei, 2012)

2.4 De-bonding between layers

Since an asphalt pavement structure consists of several layers in order to withstand traffic and environmental loading, it is very important to ensure that those layers are fully bonded and work together as a composite. A thin film of bituminous bond coat (tack coat) at the interfaces is therefore produced to achieve this condition (Muslich, 2010).

Under this situation, the overall strength and stiffness of a pavement depending not only on the strength and stiffness of each individual layer but also on the bond between them. At locations where poor interface bonding or de-bonding occurs, the pavement deterioration would be accelerated even if the stiffness of the foundation and the individual layers are still reasonably good. An assumption that adjacent pavement layers are fully bonded condition together and no displacement is developed between them is often used when designing and evaluating

pavements. However this fully bonded condition is not always achieved in reality. (Muslich, 2010, Collop et al., 2009; Ascher & Wellner, 2007)

Hakim (2002) reported that bond failure may occur at the interface between the surfacing and the binder course where the horizontal forces as a result of turning, braking, ascending, descending, accelerating and decelerating are very high. Overlaid roads and some locations on airport runways and/or taxiways, where they are subjected to high-speed braking and turning, are more likely to cause this kind of bond failure, shown in Figure 2.14 (Shaat, 1992, Hachiya and Sato, 1997). There are three main forms of deterioration associated with poor bond conditions: slippage cracking, horizontal deformation and blistering on the surfacing layer (Muslich, 2010).

Figure 2-14 Premature slippage failure on an overlay project in Nevada, USA (Charmot et al., 2005)

Raab and Partl (2004) noticed that bond problems can also occur between deeper layers such as at the interface between bases and/or between base and bituminous or cementious sub-base (Figure 2.15).

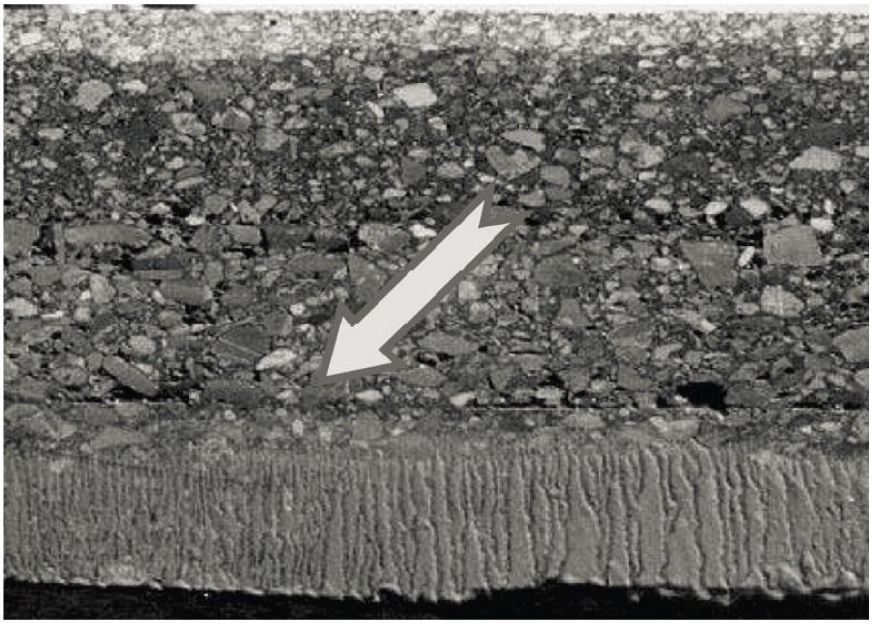

Figure 2-15 Bond failure between base and sub-base in a slab taken from a newly built Swiss Motorway (Raab and Partl, 2004)

Bond failure at the interface between surface and binder courses combined with vertical cracks can produce a pothole (Biczysko et al., 2010). An example is presented in Figure 2.16. Therefore improving the bond conditions is an effective way to prevent pothole formation.

Figure 2-16 Shallow potholes caused by de-bonding (Muench et al., 2008)

2.4.1 Separation modes

Muslich (2010) categorised bond failures into three separation modes: shear mode (A), tensile mode (B) and mixed shear-tensile mode (C) illustrated in Figure 2.17.

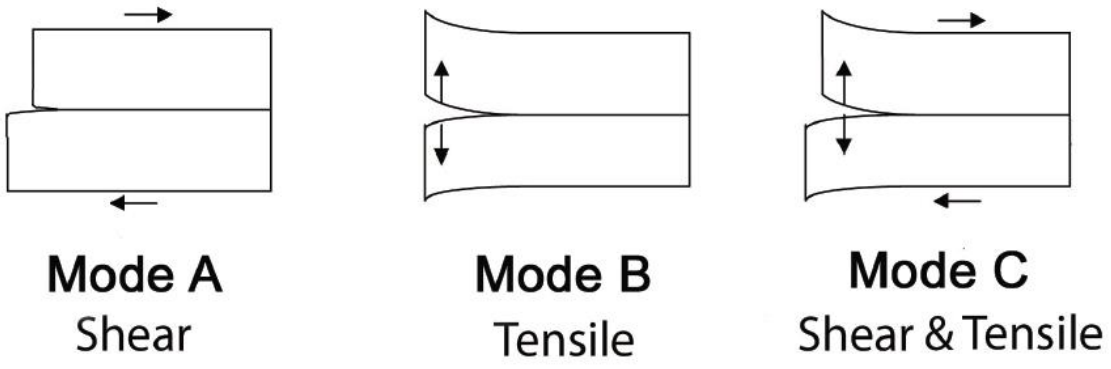

Figure 2-17 Bond failure separation modes (Muslich, 2010)

Shear separation mode is the most common type in the field as a result of induced shear stresses at the interface caused by traffic and/or temperature. Tensile separation mode is generated by vertical tensile

stress due to suction (Figure 2.18a) by the tyre and may also occur as a result of blistering.

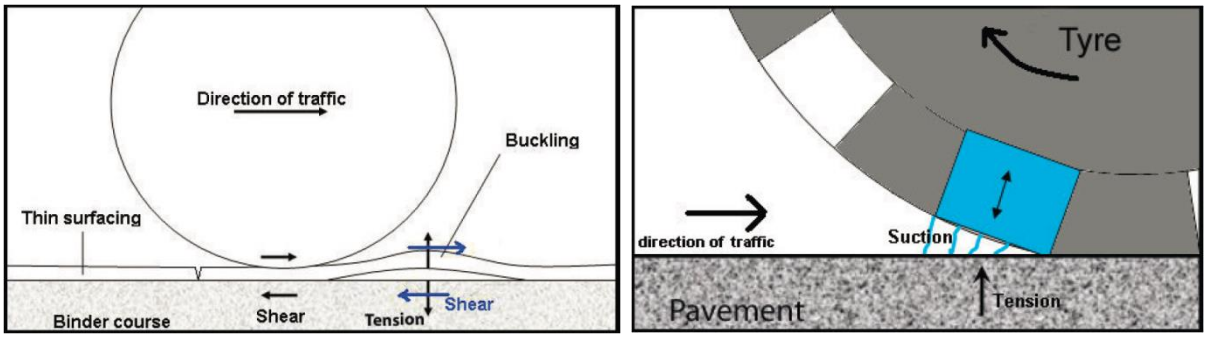

(a) (b)

Figure 2-18 (a) Shear-tensile separation associated with buckling (Raab & Partl, 2004); (b) Tyre suction phenomenon (Bernhard et al., 2005)

The mixed shear-tensile mode was not found in the literature review and hence it is reasonable to assume that this phenomenon would be rarely found in a real pavement structure. That is because the formation of mixed shear-tensile separation requires really critical conditions (combination of excessive horizontal loading, poor horizontal load transfer, surfacing layer buckling and still existing interface tensile adhesion) (Muslich, 2010).

2.4.2 Moisture effect on de-bonding

When talking about moisture effect on the bond strength between different asphalt layers, Raab et al. (2012) stated that moisture can lead to a reduction of the mean maximum shear force of up to 30% for long term water storage or combined pressure and short term water storage at 40 °C tested with the Layer-Parallel Direct Shear (LPDS) shear device. There are two mechanisms for moisture damage to the bond strength

between layers: (a) loss in strength and durability of materials due to the presence of water in the pores of the asphalt concrete (b) loss of mechanical behaviour of the bond between layers (Chabot et al., 2016). Chabot et al. (2016) used a four-point bending (4PB) test to evaluate the effect of water on the interface behaviour of bond between layers. They concluded that the presence of water will lead to debonding in a 4PB test from the observation of debonding failure mode for three specimens tested in water, shown in Figure 2.19.

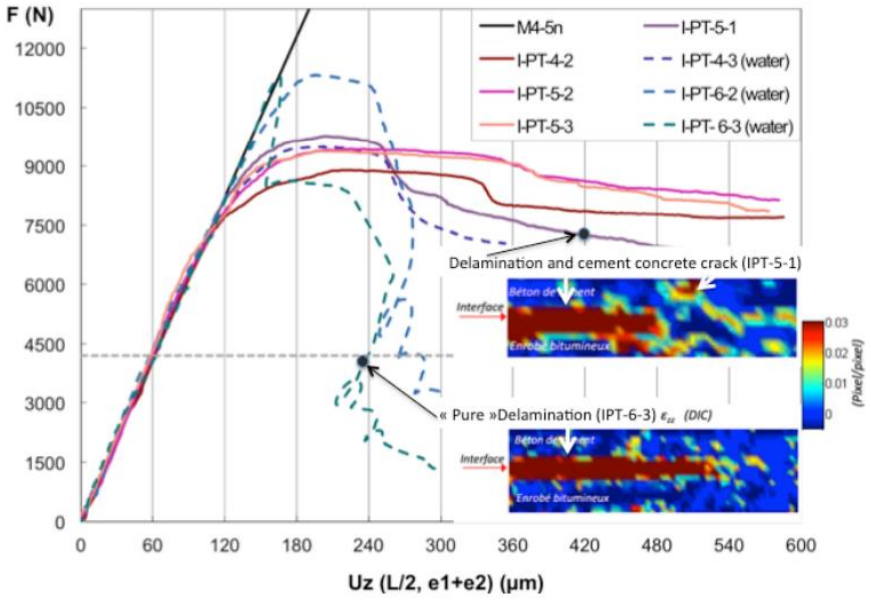

Figure 2-19 Curves of force (F)-displacement (Uz) results of cement concrete/bituminous specimens tested in air and in water with the 4PB test (0.7mm/mn, T=20°C) (Chabot et al., 2016)

2.5 Fatigue characteristics

It has been generally accepted that fatigue is a process of cumulative damage and one of the major causes of cracking in asphalt pavements. It consists of two main phases, crack initiation and crack propagation, and is

caused by tensile strains generated in the pavement not only by traffic loading but also by temperature variations and construction practices (Read, 1996; Rodrigues, 1999).

2.5.1 Fatigue characteristics

The fatigue characteristics of an asphalt mixture can be expressed as a relationship between the initial stress or strain and the number of load repetitions to failure. The majority of the fatigue prediction models have been developed based on laboratory fatigue tests and then calibrated by adding calibration factors (or transfer functions) to match the observed field fatigue performance (Yu et al. 2012). Many researchers have suggested different equations from different fatigue modes and these relationships are not usually derived from a theoretical analysis of pavement mechanics (Hamed, 2010).

The two typically used equations, shown as follows, are formulated as the result of fatigue tests depending on the mode of loading (Shen and Carpenter, 2007):

$$N_f = A\left(\frac{1}{\varepsilon}\right)^b \quad \text{in controlled-stain mode} \qquad \text{Equation 2-2}$$

$$N_f = C\left(\frac{1}{\sigma}\right)^d \quad \text{in controlled-stress mode} \qquad \text{Equation 2-3}$$

Where N_f is the number of load application to failure; ε, σ are the tensile strain or stress repeatedly applied; A, b, C, d are material coefficients, derived by fitting the data from laboratory testing.

Researchers tend to use the controlled strain mode as the results tend to be more independent of temperature for the controlled strain mode than the controlled stress mode. Also it is easier plotting and comparing the results of the same material for different temperatures when using the controlled strain mode.

Miner (1945) made a hypothesis of damage which can be used to account for strain variations. The hypothesis is represented as a relative damage factor where the crack will occur when the sum of the damage factors equals one. Miner's linear law of cumulative damage in conventional asphalt pavement design is given as follows (Miner, 1945):

$$D = \sum_i^T \frac{n_i}{N_i} = 1 \qquad \text{Equation 2-4}$$

where D is the damage; T is the number of periods; n_i is the number of load applications during a period i; N_i is the ultimate number of load applications the pavement could carry.

Bonnaure was the one of the first researchers to believe that fatigue strength can be affected by mixture characteristics. He developed his research by statistical analysis of data from several research institutions. He used the following equations to predict fatigue life, respectively for controlled strain and controlled stress conditions (Bonnaure et al., 1980):

$$\varepsilon = \left[\left(4.102 \times PI\right) - \left(0.205 \times \mathrm{PI} \times \mathrm{V_b}\right) + \left(1.094 \times \mathrm{V_b}\right) - 2.707\right] \times S_{mix}{}^{-0.36} \times N^{-0.2} \qquad \text{Equation 2-5}$$

$$\varepsilon = \left[\left(0.3 \times PI\right) - \left(0.015 \times \mathrm{PI} \times \mathrm{V_b}\right) + 0.08 \times V_b - 0.198\right] \times S_{mix}{}^{-0.28} \times N^{-0.2} \qquad \text{Equation 2-6}$$

where PI is the penetration index of bitumen; V_b is the volume of binder; N is the number of load cycles; $S_{\min}$ is the stiffness of the mixture.

Pell suggested the following observed relationship between the number of load applications to crack appearance in the pavement (N_f) and the tensile strain at the bottom of the asphalt concrete layer (ε_t):

$$N_f = K_1\left(\frac{1}{\varepsilon_t}\right)^{K_2} \qquad \text{Equation 2-7}$$

where K_1 and K_2 are the intercept and the slope respectively, determined by linear regression (Pell, 1967 and 1987).

More recently many researchers have found that the stiffer mixtures generally have shorter fatigue life in controlled strain laboratory tests; thus, they have introduced the stiffness modulus into the fatigue relation to absorb temperature and loading time effects (Monismith et al., 1985):

$$N_f = K_1\left(\frac{1}{\varepsilon_t}\right)^{K_2} \cdot \left(\frac{1}{\mathrm{E0}}\right)^{K_3} \qquad \text{Equation 2-8}$$

where: N_f = number of cycles to failure, ε_t = tensile strain at the bottom of the asphalt layer, E_0 = initial asphalt mix stiffness, and K_1 , K_2 and K_3 are regression constants obtained from laboratory testing.

Finn et al. (1977) determined the values of K_1 , K_2 , and K_3 for their laboratory fatigue prediction model based on stress-controlled four-point bending fatigue test data. The values of K_1 , K_2 , and K_3 were 0.00432, 3.291 and 0.854, respectively. Then in 2005 El-Basyouny and Witczack used long term pavement performance (LTPP) data to recalibrate equation 2.8 and developed the new bottom-up fatigue cracking model for the American Mechanistic-Empirical Pavement Design Guide (M-E PDG)

under the National Cooperative Highway Research Program (NCHRP) 1-37A (El-Basyouny et al., 2005). A sigmoid function considering failure criteria as 50% cracking of the total lane area was used to account for the effect of asphalt layer thickness to fatigue life. The final fatigue cracking model is shown below:

$$N_f = 0.00432 \times K \times C \left(\frac{1}{\varepsilon_t}\right)^{3.9492} \cdot \left(\frac{1}{E}\right)^{1.281} \quad \text{Equation 2-9}$$

$$K = \frac{1}{0.000398 + \frac{0.003602}{1 + e^{(11.02 - 3.49 h_{ac})}}} \quad \text{Equation 2-10}$$

$$C = 10^M \quad \text{Equation 2-11}$$

$$M = 4.84\left(\frac{v_{be}}{v_{be} + v_a} - 0.69\right) \quad \text{Equation 2-12}$$

Where h_{ac} is the thickness of LMA layer(inch), v_{be} is the effective binder content (%) and v_a is the air void (%).

2.5.2 Factors affecting fatigue in asphalt mixtures

Various factors can affect the fatigue behaviour of asphalt mixtures. Generally speaking, the method of specimen manufacture (compaction) and material characteristics can affect the fatigue behaviour. However these two factors can be controlled in theory. Traffic loading and environmental variables (temperature, ageing, healing, etc.) can also have a significant effect on fatigue behaviour.

2.5.3 Fatigue related damage

In general, there are four common pavement fatigue cracking types: alligator cracking, block cracking, longitudinal cracking and transverse cracking (shown in Figure 2.20) (Rababaah et al.). Figure 2.21 shows a pothole surrounded by alligator cracking which indicate that severe alligator cracking can lead to pothole.

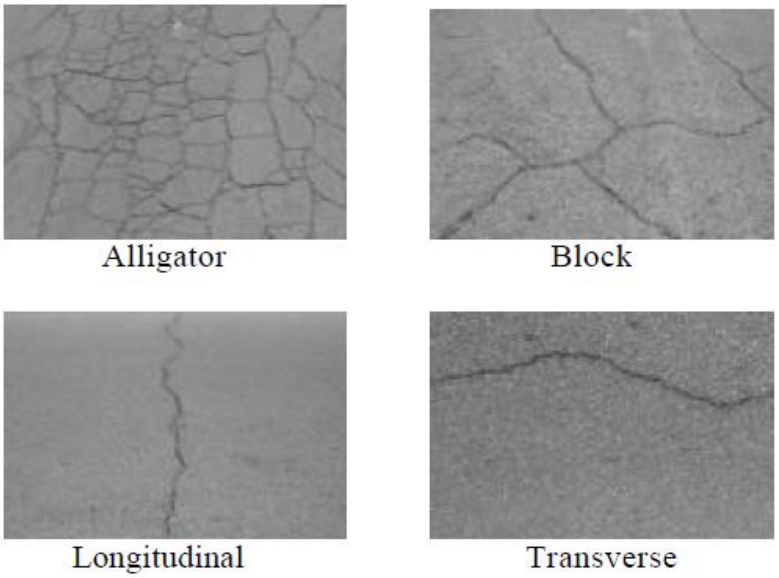

Figure 2-20 Types of Pavement Cracks (Rababaah et al., 2005)

Figure 2-21 Pothole Surrounded by Alligator Cracking (FHWA, 2009)

The formation of a crack is a result of two forms of cracking in an asphalt layers: top-down cracking and bottom-up cracking. Top-down cracks (TDC) are longitudinal and/or transverse cracks that initiate at the pavement surface and propagate downward and outward (Gilbert Y. Baladi et al., 2003). Svasdisant et al. (2002) stated that top-down cracking is caused by high tensile stresses due to traffic loading, temperature gradients, binder ageing and construction quality (materials, compaction and paving) (Svasdisant et al.,2002).

2.6 Summary

Asphalt mixtures are widely used as construction materials in road pavements. During their service lives, asphalt pavements will deteriorate with the passage of time under traffic load and environmental effects.

Hence it is important to understand the factors that leading to pavement distress. This literature review has given a comprehensive introduction to the two main causes of damage. Moisture damage is considered as one of the most important causes of pavement distress. As stated in section 2.2, the presence of water can result in adhesive failure at the bitumen-aggregate interface and/or cohesion failure within the bitumen film. This will accelerate the deterioration of an asphalt pavement together with other factors such as ageing of the binder, traffic loading and environmental effects. Compared to cohesion, adhesion between bitumen and aggregate surface plays a more important role in moisture damage. With the presence of water, the bond strength will deteriorate over the moisture conditioning time. This is similar to the moisture effect on debonding between asphalt layers. Fatigue is also a major cause of asphalt pavement deterioration. It usually results in cracking in the pavement. Different predictions of fatigue life were also reviewed together with the factors that affect fatigue in asphalt mixtures. Despite the many laboratory experimental tests on moisture and fatigue damage to asphalt mixtures, there is a lack of an analytical model that is capable of predicting the stated damage while utilising simple calculations. Inspired by the research studies reviewed in this chapter, this thesis is focused on development of a simplified analytical approach to estimation of damage due to moisture and fatigue. It should be mentioned that the model built in this research is based on a number of simplifying assumptions, which need specially designed laboratory experiments or numerical simulations

to validate and calibrate. These experiments are not within the scope of this research but will need to be tested in future studies.

Chapter 3. Site Monitoring

Although pavements may be well designed with the purpose of providing the most economical combination of pavement layers, different forms of pavement distress such as fatigue cracking, ravelling and potholes still occur over time. They are always considered to be the result of a combination of traffic and the environment. The aim of the site monitoring described here was to observe pavement distress initiation and development in real pavements to obtain a better understanding of the factors that influence pavement distress.

3.1 Introduction

As stated above the two main factors that cause pavement distress are trafficking and water on the surface. In order to determine the influence of trafficking, the selected monitoring sites were under different kinds of traffic flow and traffic load. The terrains of the sites were also different. Some sections were flat and straight and the others sloping and winding. The weather conditions were also recorded in general forms. Data collection was by photography and sketching. However, the exact length, size and depth of the different regions of distress were not measured. A navigation application was used to locate the position for photography each time and then to sketch the road surface distress position and shape. The surveys were conducted in April 2012, August 2012, March 2013, July 2013, January 2014, August 2014, February 2015, and June

2015. However, due to the expansion of the Nottingham tram system in 2012, one of the sites (Nottingham University east entrance) was no longer available to monitor after that date. The sites inside the University Park are designated as low traffic flow (less than 10000 vehicles/day) and low traffic load (less than 5% truck/bus traffic). The sites outside the University Park are designated as heavy traffic flow (over 20000 vehicles/day)) and heavy traffic load (over 10% truck/bus traffic).

3.2 Results from the survey

A total four sites are presented in this chapter with the sketches and photos of pavement distress propagation. Two sites inside the University Park: University East Entrance and South Entrance, and two sites outside the University Park: Derby Road and Beeston Road.

3.2.1 University East Entrance

This site comprises 100m at the east entrance of Nottingham University which is a severe turning site. The annual average daily 2-way traffic flow for University east entrance was around 9000 (Department for Transport, 2016) and it is classified as a lightly loaded pavement. With a speed limit of 20 mph, vehicles have to brake when entering from Clifton Boulevard (at about 63449 annual average traffic flow) for which the speed limit is 40 mph. It became seriously damaged under these two situations (braking and turning). During winter, this site also deteriorated at a rapid

pace. It can be seen that a pothole shown in Figure 3.1a) appeared on this site during the winter and was soon repaired; then another pothole appeared and developed quickly. These two potholes seem to be the severe end result of alligator cracking. After repairing the potholes, surface break-up accelerated the development of a new pothole. It was an excellent site for monitoring, but became unavailable now due to tram work.

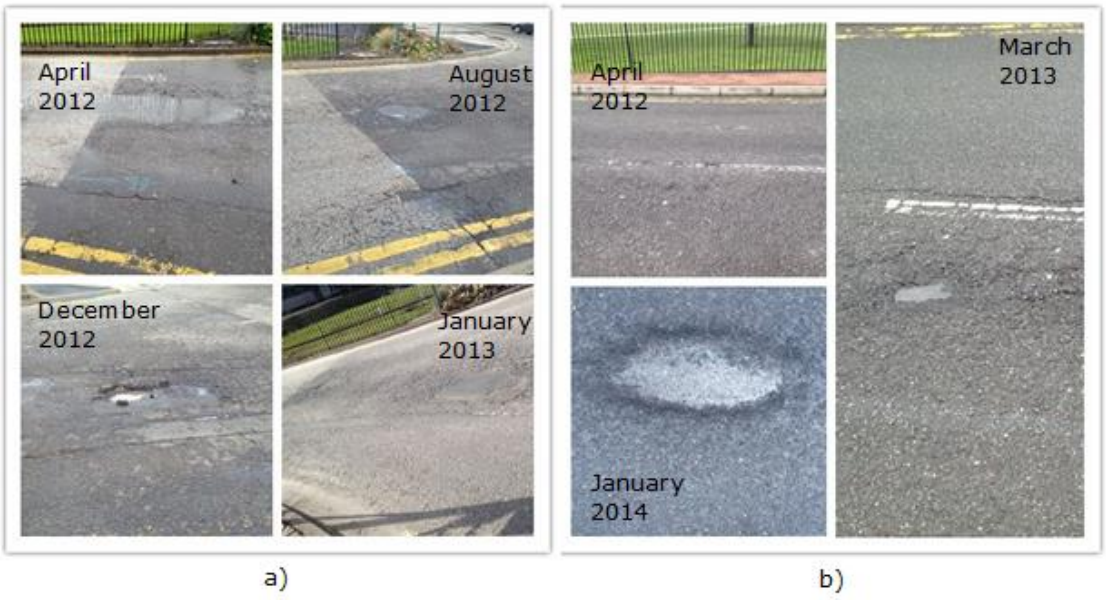

Figure 3-1 a) Photos taken at University East Entrance b) photos taken at University South Entrance

3.2.2 University South Entrance

The annual average daily traffic flow for the University south entrance was 7000 (Department for Transport, 2016) and it is therefore a lightly loaded pavement. This site was a ravelled pavement. Ravelling is more obvious in the four areas shown on the sketch. On the first site visit in April 2012, a few small potholes already existed together with occasional transverse cracking, longitudinal cracking and alligator cracking. Pothole 1 shown in Figure 3.1b) and 3.2 developed very quickly in size and depth. At first it was caused by ravelling, but later on surface break-up was the main

problem. On the second visit, two new potholes 2, 3 had appeared. Pothole 2 was near the edge of the road and it became bigger and deeper by the third visit. Pothole 3 was between two longitudinal cracks. However it had been repaired before the third visit. All the remaining areas of distress also deteriorated slightly between surveys.

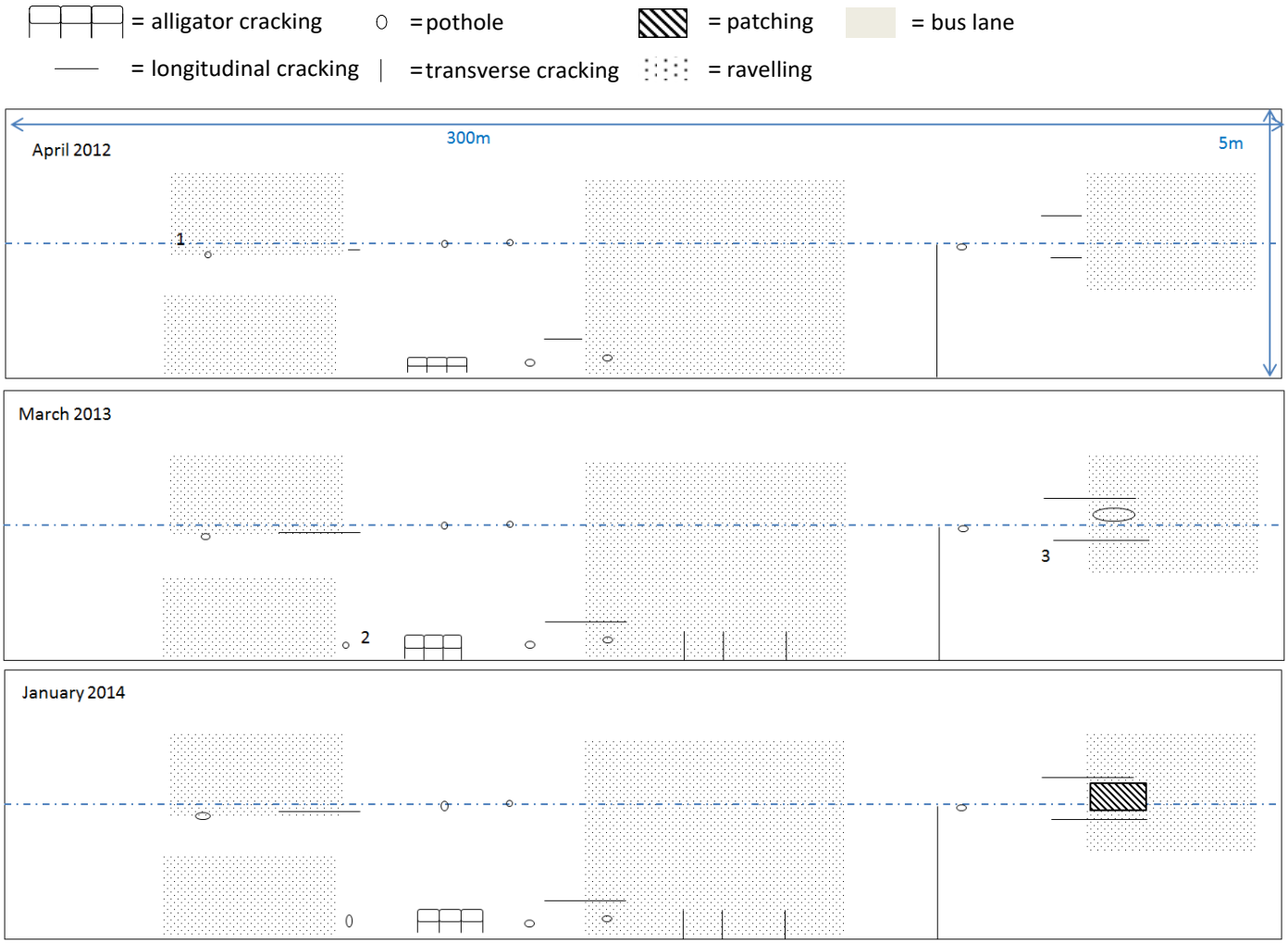

Figure 3-2 Diagrams showing the pavement deterioration over the time on University South Entrance

3.2.3 Derby Road

The annual average daily traffic flow for Derby road is around 21000 (Department for Transport, 2016) and it is therefore designated as a heavily loaded pavement. The pavement surface was in fair condition with several low severity areas of cracking and few medium severity cracks along the edge. At the end of survey area, the pavement

showed a ravelled surface with some medium severity cracking. At point 1 in Figure 3.3 and 3.4, longitudinal cracking had first occurred in 2008. It deteriorated slowly into high severity alligator cracking by 2012. A small pothole started to form in 2013. As soon as the pothole formed, it developed quickly in size and depth and some further small potholes appeared near it. After the local authority repaired these potholes, some additional cracking formed around the pothole. Other areas of distress also deteriorated slightly during the survey period. The photos for point 1 at different date are shown in Figure 3.4.

Figure 3-3 Photos at Derby road, photos in July 2008, June 2011 and September 2014 are taken from google map

Figure 3-4 Diagrams showing the pavement deterioration over the time on Derby Road

3.2.4 Beeston Road

The annual average daily traffic flow for Beeston road is about 30000 (Department for Transport, 2016) which makes it another heavily loaded pavement. The overall pavement surface was in good condition with only a few low severity cracks and some alligator cracking along the edge. The alligator cracking deteriorated more obviously than the others. This may have been caused by poor drainage as well as traffic loading. The water tended to remain along the cracked area due to the sinking surface. At the same time, the heavy traffic flow provided frequently traffic loading even frequently overloading sometimes. During the three visits, the alligator cracking deteriorated from medium severity to high severity alligator cracking. Other edge cracks all deteriorated slowly through the survey period. The sketches indicate the pavement deterioration are shown in Figure 3.5.

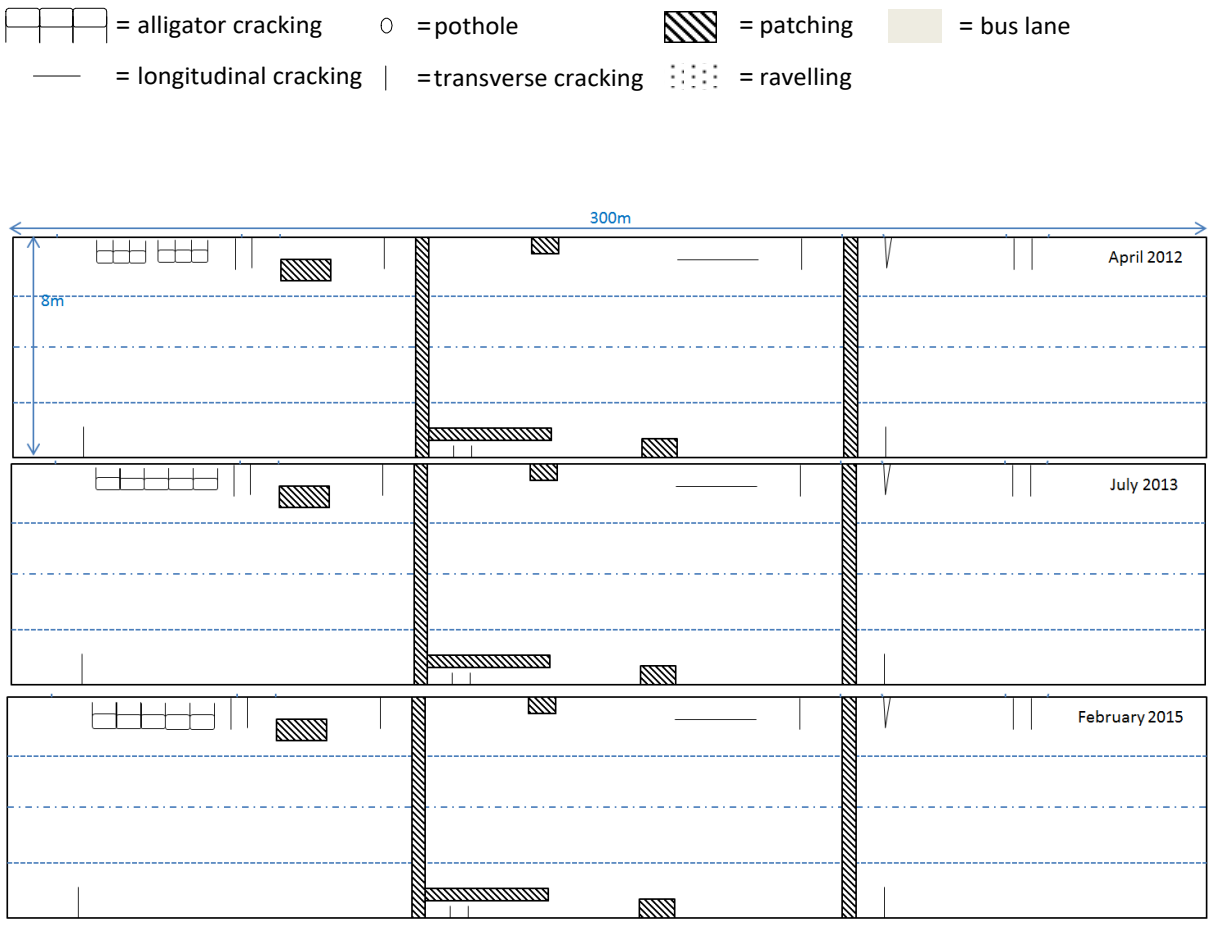

Figure 3-5 Diagrams showing the pavement deterioration over the time on Beeston Road

3.3 Summary

This chapter has presented observations from four different sites. The most common pavement distress types found at these sites were potholes, alligator cracks and ravelling. They all deteriorated under traffic flow. A summary table (Table 3.1) is shown below. It is noted that the surface types for University south entrance, Derby road and Beeston road are all SMA, but their performances are quite different. This may because the SMA used in UK varies in its constituent. Moreover, the binder content may be not the same. The surface type for University east entrance is

DBM. Although the condition of this site was the worst, it did not mean that DBM was worse than SMA. The site itself was a special case with both turning and braking traffic conditions. Turning and braking can accelerate pavement distress deterioration for any surface type. Thus no specific conclusions for different types of asphalt can be obtained due to lack of information.

Table 3-1. Summary table for the site monitoring

Site	Surface type	Traffic	Condition	Maintenance
University east entrance	DBM	9000	poor, potholes	minor patching
University south entrance	SMA	7000	fare, ravelling and few potholes	resufacing, minor patching
Derby road	SMA	21000	fare, longitudinal cracking	major patching
Beeston road	SMA	30000	fare, edge alligator cracking	minor patching

After analysis of the observations the following conclusions can be drawn:

- From the observations at University East Entrance, the conclusion that turning and braking can accelerate pavement distress deterioration can be drawn. This may be because turning and braking can cause the corrugation or shoving of the pavement surface and this leads to an uneven surface which means water will be trapped. Thus the water can penetrate into the surface course and even base course more easily compared to a normal pavement. With the help of frequent traffic loads, pavement distress will occur and deteriorate quickly.

- Ravelling was found to be the main distress type at University South Entrance together with a few resulting potholes. These deteriorated slightly quicker during a heavy rainfall period even under the light traffic load. This may due to insufficient bitumen content in the asphalt and the loss of bitumen binder to aggregate particle adhesion with the presence of water.

- Longitudinal cracking was observed in the wheel paths at Derby Road. In one key location, this had deteriorated into multiple cracking failure by resulting in pothole which is agree with the fact that several fatigue cracking can lead to the formation of pothole.

- Beeston road is in a good service condition overall. The most significant distress was alligator cracking at the edge. This may cause by the uneven pavement surface and an inadequate edge support. Alligator cracking is also the sign of fatigue indicating the failure of the structure. If left untreated, the alligator cracking will allow infiltration of water and worsen the pavement surface which may result in potholes.

Evidence from the site observations and literature indicates a strong link between ravelling and other forms of surface break-up and both traffic and water effects. This is not modelled or predicted in any existing design method. Therefore this thesis will tackle it by analytical modelling of the water pressure on the pavement surface and within the pavement

structure and then combined with the laboratory tests results to predict surface deterioration such as ravelling.

Chapter 4. Analytical Modelling of Water Pressure on the Pavement Surface

From the literature review it is clear that moisture is the main cause of pavement surface deteriorations (i.e. ravelling and potholes). The first step towards understanding the mechanism behind this issue is to understand what happens on the pavement surface. In this chapter, a simplified analytical model is developed to simulate the tyre movement with the presence of surface water and to calculate the resulting water pressure.

The loss of surface chippings or aggregates from the surface of a pavement is a major problem for most road pavements. This loss of surface material can occur at any time and if it is left untreated, this can completely destroy the wearing course of a pavement, then leading to potholes. Therefore it is necessary to understand surface material loss. Factors such as ageing, trafficking and moisture damage cause the binder to harden, and loss of adhesion and cohesion allow the aggregate to be removed. As a first attempt, only two main factors are taken into account in this research. Based on the literature review, traffic loading and moisture damage are chosen.

Rainfall onto the pavement leads to a water film on the pavement surface. With the passage of vehicles, the trapped water between the pavement and the tyre is expelled through the channels provided by the pavement

macro-texture and by the tyre tread. This will logically result in a water pressure pulse on the pavement surface, potentially forcing the water into the pavement layers through cracks, micro-cracks and joints. This in the end could destroy the bond between bitumen and aggregates leading to more serious damage to the pavement.

4.1 Smooth Pavement Surface

The first step is to calculate the water pressure at the pavement surface due to moving wheels on a smooth surface. In reality, the surface water under the tyre can be expelled in different directions, illustrated in Figure 4.1. No matter what directions the water travelled, it in the end will be at the both sides of tyre which means the transvers component of water velocity is the one that mattered.

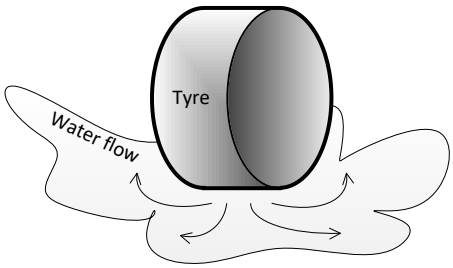

Figure 4-1 Water flow under tyre in reality

Therefore the really 3D water movement can be transferred to a 2D simulation as shown in Figure 4.2. The water is assumed incompressible to facilitate calculations. The assumption is that the water pressure is caused by the vertical motion of the face of the moving tyre, squeezing water to both sides. The water pressure distribution can be calculated

through dynamic equilibrium by assuming volume and mass conservation of the water for known vertical tyre velocity. This is due to a combination of acceleration/deceleration of water mass and viscosity effects. This smooth pavement surface model serves as a basis for more complicated models (textured surface and permeable surface) which will be introduced in later sections.

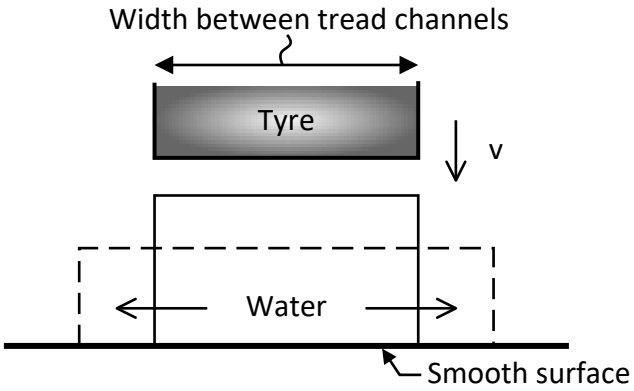

Figure 4-2 Simplified smooth pavement surface

4.1.1 Tyre Vertical Velocity

The most important and fundamental parameter is the tyre vertical velocity. Mansura et al. (2015) investigating indentation of surface aggregate into tyre rubber developed a relationship between indentation rate and time based on a 3D finite element whole tyre model, as shown in Figure 4.3 for the case of a car moving at 100 km/hour. From this figure the relationship between indentation rate (i.e. tyre vertical velocity) and time can be simplified and described as a linear function:

$$V_{indentation} = 42.857 \times t_{indentation} \quad \text{at 100 km/hour vehicle velocity} \quad \text{Equation 4-1}$$

Where $V_{indentation}$ is the indentation rate (m/s)

$t_{indentation}$ is the indentation time (s)

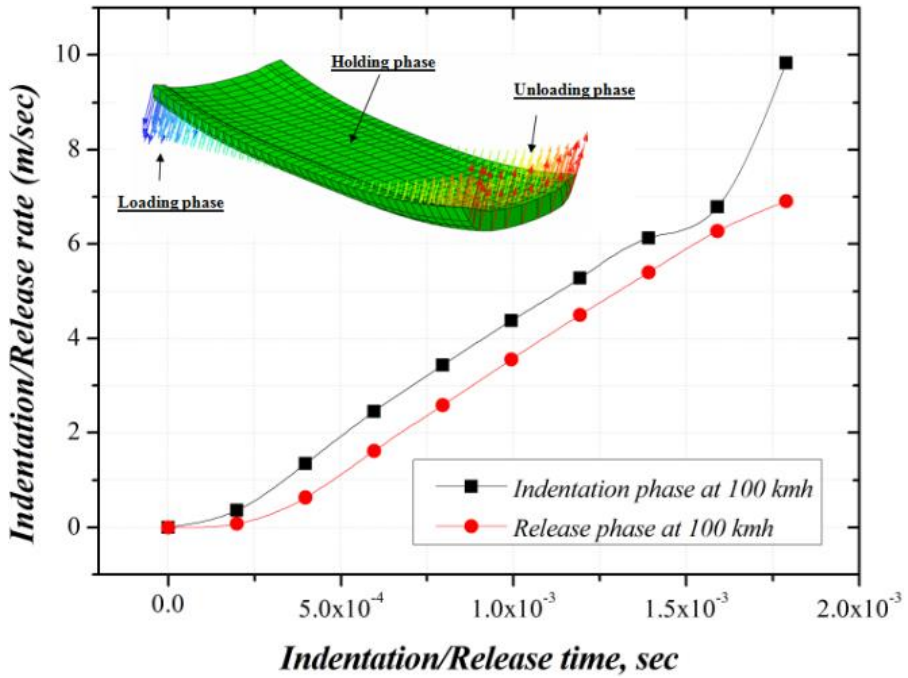

Figure 4-3 Vertical tyre velocity before and after contact adopted from Mansura (2015)

Based on the equation above a linear relationship between vertical velocity and time for different vehicle speeds is formulated as follows:

$$V_v = k \times (t_0 - t) \qquad \text{Equation 4-2}$$

$$t_0 = \sqrt{\frac{2H}{k}} \qquad \text{Equation 4-3}$$

Substituting t_0 into equation 4.1:

$$V_v = -kt + \sqrt{2Hk} \qquad \text{Equation 4-4}$$

where V_v is the tyre vertical velocity (m/s);

t is the elapsed time (s);

t_0 is the total time needed for the tyre to reach the pavement surface;

k is a coefficient $= 42.857 \times V$ with V being the vehicle velocity (km/h)

H is the water depth on the surface (m);

Typical value for tread width of 20mm is chosen while water depth and vehicle speed vary.

4.1.2 Calculations

The basic assumption in this calculation is that the total water volume per unit length expelled by the tyre tread is equal to the water volume per unit length that goes to both sides of the tyre tread i.e. movement is purely transverse. The shaded area 1 which is shown in Figure 4.4 represents the water expelled by the tyre tread, and this is equal to shaded area 2, which represents the water that goes to both sides of the tyre tread.

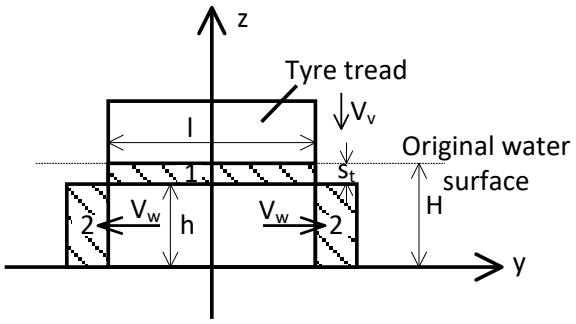

Figure 4-4 Schematic showing equal water volume rule

Vertical distance 's_t' (Figure 4.4) is calculated by integrating velocity from Equation 4.4:

$$s_t = \frac{1}{2}(-k)t^2 + \sqrt{2Hk} \cdot t \qquad \text{Equation 4-5}$$

so that the remaining distance from the tyre tread to the asphalt surface 'h' is given by:

$$h = H - s_t$$ Equation 4-6

The average velocity 'V_w' of the water expelled to one side is then calculated by balancing these two areas:

$$V_w = \frac{l \times V_v}{2 \times h}$$ Equation 4-7

where l is the width of the tread.

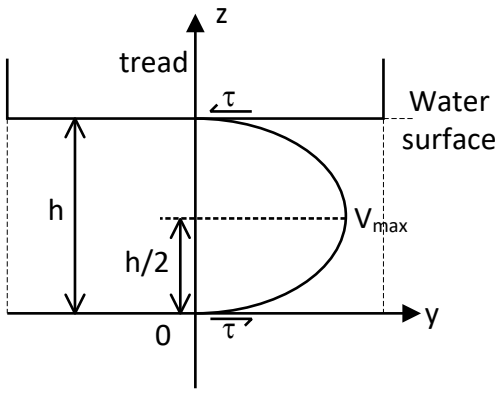

Figure 4-5 Water velocity distribution under tread

It is assumed that the water flow under the tread is laminar. From the experience of water velocity distribution in pipe flow (White, 1999), the water flow velocity distribution is in the form of a paraboloid which can be described using the following equation:

$$v = Az^2 + Bz + C$$ Equation 4-8

where A, B and C are constants and can be calculated from the boundary conditions.

With viscous flow there can be no slip at the boundary so that $v = 0$ when $z = 0$ and $z = h$. The maximum water velocity occurs at the centre line so that $v = v_{\max}$ when $z = h/2$. With a knowledge of the geometry of a paraboloid, the average water velocity is two-thirds of the maximum

velocity. Using these relationships to evaluate the constants in the above equation therefore

$$C = 0, A = -\frac{B}{h}, B = \frac{6V_w}{h}$$

Hence

$$v = -\frac{6}{h^2}V_w z^2 + \frac{6V_w}{h} z \qquad \text{Equation 4-9}$$

From Newton's equation of viscosity, the shear stress is related to the velocity by the equation $\tau = -\mu(dv/dz)$. Substituting the differential of the above equation:

$$\tau = -\mu(-\frac{12}{h^2}V_w z + \frac{6V_w}{h}) \qquad \text{Equation 4-10}$$

Thus the shear stress at $z = 0$ and $z = h$ is given by:

$$\tau_{(z=0)} = -\mu\frac{6V_w}{h}$$
$$\tau_{(z=h)} = \mu\frac{6V_w}{h}$$

Looking at a water element under the tread (Figure 4.6), it is accelerated under the different forces. The average water acceleration a_w is calculated from the average water velocity:

$$a_w = \frac{dV_w}{dt} = \frac{l}{2}\frac{(-kt + \sqrt{2Hk})^2 - kh}{h^2} \qquad \text{Equation 4-11}$$

Now according to Newton's Second Law, i.e. force equilibrium, applied to a water element under the tread:

$$\Delta Ph = ma_w + (\tau_{(z=h)} - \tau_{(z=0)})dy \qquad \text{Equation 4-12}$$

where m is the mass of the water element and is equal to ρhdy.

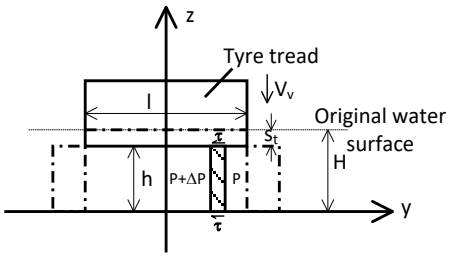

Figure 4-6 Diagrams showing the forces acting on a water element

Hence the water pressure difference ΔP is:

$$\Delta P = \frac{\rho h a_w dy + (\tau_{(z=h)} - \tau_{(z=0)})dy}{h} \qquad \text{Equation 4-13}$$

Integrating Equation 4.13 gives:

$$P = \frac{\rho h a_w (\frac{l}{2} - y) + (\tau_{(z=h)} - \tau_{(z=0)})(\frac{l}{2} - y)}{h} \qquad \text{Equation 4-14}$$

Substituting a_w and τ into equation 4.14:

$$P(y) = \frac{(\frac{l}{2} - y)l}{2h^2} \left\{ \rho \left[(-kt + \sqrt{2Hk})^2 - kh \right] + 12\mu(-kt + \sqrt{2Hk}) \right\} \qquad \text{Equation 4-15}$$

4.1.3 Results and discussion

Figure 4.7 shows the variation of water pressure with time for five different vehicle velocities where the same water height of 2mm was assumed above the surface. The tyre tread width is assumed to be 20mm. Due to the "perfectly smooth surface" assumption, there is an impact pressure of infinite at the last zero second which is not able to predict in this analytical calculations. Moreover the water depth is irrelevant in this calculation. This is because the tyre tread vertical

velocity is only dependent on the distance from the pavement surface and the vehicle velocity based on Equation 4.4. Therefore the vertical velocity is the same at the same depth which means the same average water velocity and the same average water acceleration at the same depth results in the same water pressure.

Despite the unrealistically high peak pressure values, the trend of the pressure time-histories with varying vehicle velocities is very clear. It is observed from this figure that higher vehicle velocity results in a higher peak water pressure that corresponds to a shorter rise time.

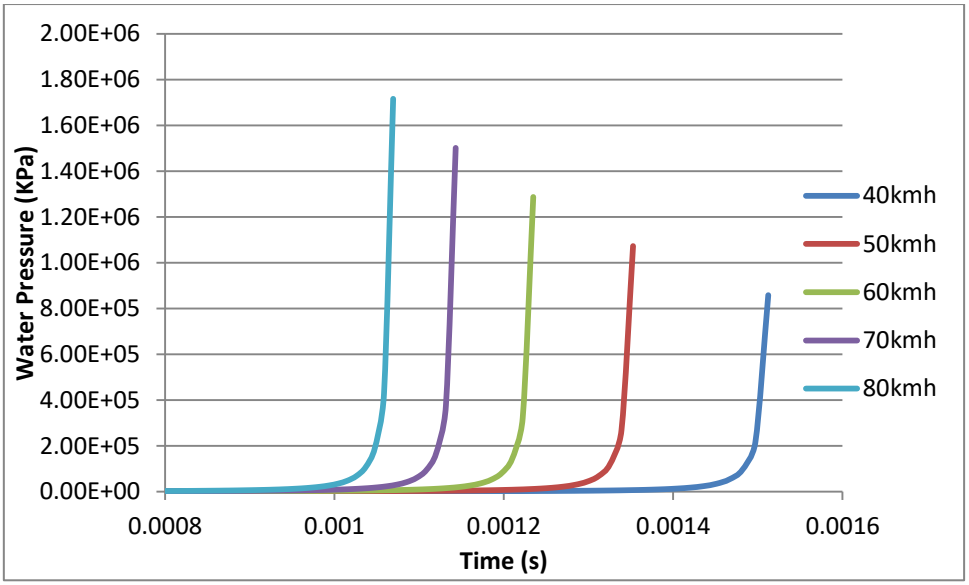

Figure 4-7 Centre point water pressure at different vehicle velocities for smooth surface

4.2 Textured pavement surface

In reality, the pavement surface is never perfectly smooth and flat. So an idealised textured pavement surface is introduced here. Figure 4.8 illustrates the structure of the textured surface, which, compared to the smooth surface, has regular protrusions. The protrusions are assumed to

be cylindrical. In order to calculate the water pressure at ground level in this case, an equivalent smooth surface with an additional depth of h_e can be used. This is done by equating the volume of the remaining region within the texture to that of an equivalent cuboid.

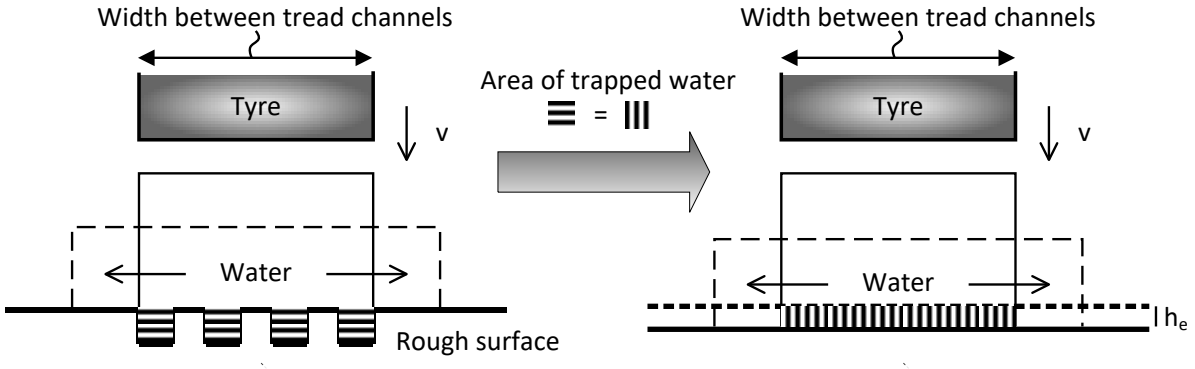

Figure 4-8 Simplified textured pavement surface

4.2.1 Calculations

Because it is assumed that there are protrusions on the textured pavement surface, the tyre is not able to be in full contact with the surface. There will be some regions that are still fully filled with water and from which the water will never be expelled.

Figure 4.9 indicates how the tyre rubber is assumed to deform around the protrusions.

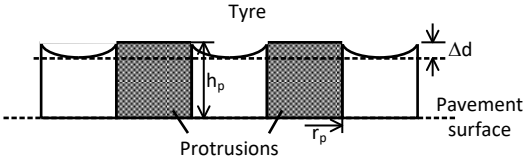

Figure 4-9 Deformation of Tyre Tread in Contact with Surface Protrusions

First of all, the effective tyre rubber pressure P_{Re} acting on the protrusions needs to be determined using the following pressure definitions:

$$l = \frac{F}{P_T w} \qquad \text{Equation 4-16}$$

$$P_R = \frac{P_T}{n_1} \qquad \text{Equation 4-17}$$

$$P_{\mathrm{Re}} = \frac{P_R}{n_2} \qquad \text{Equation 4-18}$$

where F is wheel load,

l is length of the wheel contact area,

w is width of the wheel contact area,

P_T is tyre pressure,

P_R is rubber pressure,

n_1 is contact percentage of tyre,

n_2 is ratio of contact protrusion to tread.

Then the load on protrusions F_p is calculated as:

$$F_P = P_{\mathrm{Re}} r_p^2 \pi \qquad \text{Equation 4-19}$$

where r_p is the radius of the protrusions;

Indentation Δd determined by the Boussinesqis's solution is given by:

$$\Delta d = \frac{F_P(1-\nu^2)}{2 r_p E_r} \qquad \text{Equation 4-20}$$

where E_r and ν are the elastic modulus and Poisson's ratio of rubber;

Therefore the equivalent height h_e is equal to

$$h_e = n_2(h_p - \Delta d)$$ Equation 4-21

The next step is to add the calculated equivalent height h_e to equation 4.6, and the new effective remaining distance from the tyre tread to the asphalt surface 'h' is:

$$h = H - s_t + h_e$$ Equation 4-22

This new effective remaining distance h is used in Equations 4.7 to 4.15 to calculate the water pressure with a textured pavement surface.

4.2.2 Results and discussions

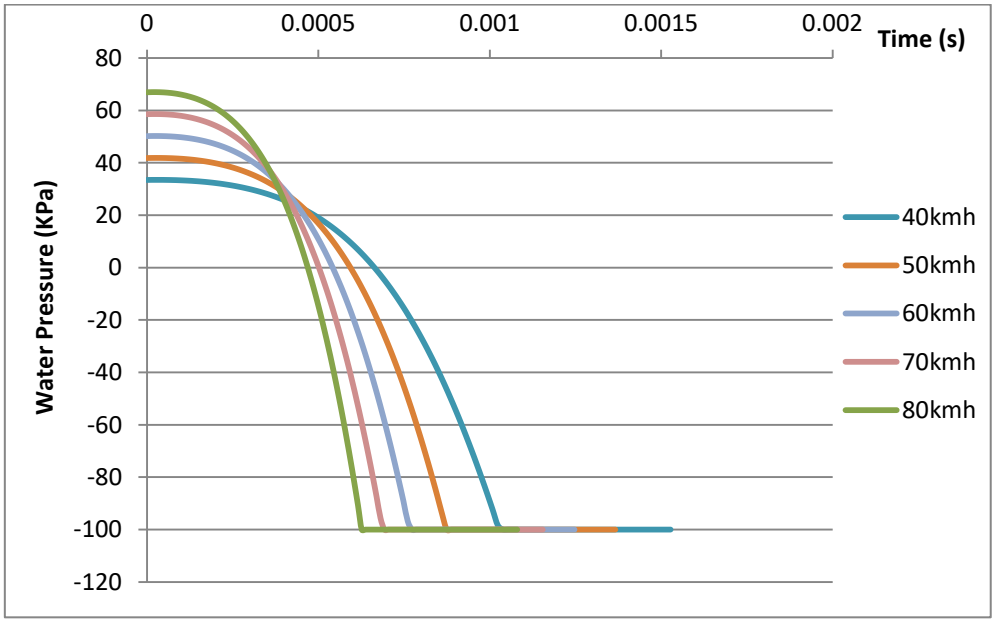

Figure 4-10 Centre point water pressure at different vehicle velocities for textured surface

Figure 4.10 shows the variation of water pressure midway between tread channels with time for five different vehicle velocities and a protrusion height of 1.5mm radius of 1mm. Compared to the perfectly smooth surface, this textured pavement surface assumption gives a more realistic result. Apart from that, the figure shows that high vehicle velocity results

in high peak water pressure. Interestingly, the water pressure in this figure, which is initially positive, reduces to zero and then becomes negative increasing with vehicle velocities. The positive peak pressure happens right after the tyre touches the water surface. However it can be seen that the water pressures reach negative values, theoretically beneath -100kPa, for all vehicle velocities after a certain time. This means that a vacuum will form in the space under the tyre tread since, in reality, the maximum negative water pressure cannot exceed 100kPa. The negative pressure occurred because of the inertia of the water. At first, the water is accelerated by the tyre until the water pressure reaches to its maximum value. At that time, the water is compressed and not equilibrium. It became decelerated due to the pressure difference and the inertia of water. This stage stops when the water pressure reaches to the negative maximum value.

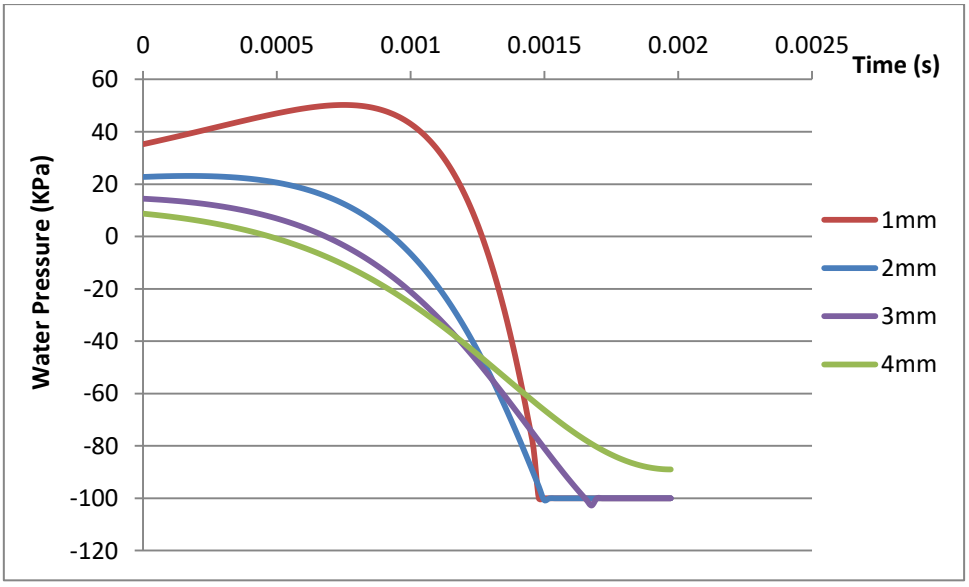

Figure 4-11 Centre point water pressure at different protrusion heights for textured surface

Figure 4.11 shows the water pressure changing with different protrusion heights with the same radius of 1mm under the same vehicle velocity of 60km/h. These results show a similar trend to those of Wei (2012), Cui et al. (2008) and Wang (2016). However they all analysed the whole process of vehicle approach and leaving. This calculation has only considered the stage of vehicle approach (particularly from the point where the tyre touches the water surface to where it contacts the pavement surface). Therefore this result only mirrors the first half of their (Wei, Cui et al. and Wang) results. It can be seen that a lower protrusion height will result in a higher peak water pressure. In all cases, the value of water pressure is positive at the beginning and becomes negative after a certain time. Vacuum (-100kPa pressure) happens in all cases apart from with a protrusion height of 4mm.

As illustrated in Figure 4.12, the textured pavement surface calculations are also applicable to a micro-scale to determine the water pressure on one single protrusion.

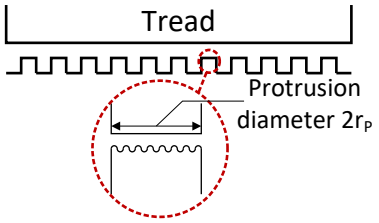

Figure 4-12 A micro-scale for rough pavement surface

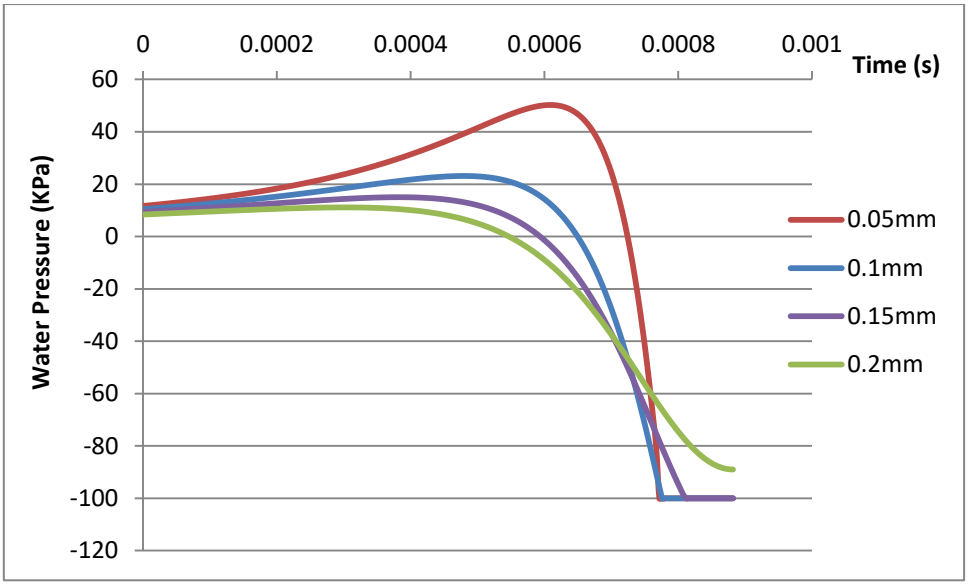

Figure 4-13 Centre point water pressure at different protursion heights for textured surface for a micro-scale

The tread width, protursion heights and radius used in the micro–scale are all scaled down by the same proportion. Similar conclusions can be drawn compared with the different protursion heights. Compared with the two scales, it can be seen from Figure 4.13 that the pressure differences between different portursion heights occurred right after contact at the full-scale, whereas the water pressure is very closed to each other at the micro-scale. However, the peak pressure for the same protursion heights to radius ratio is nearly the same.

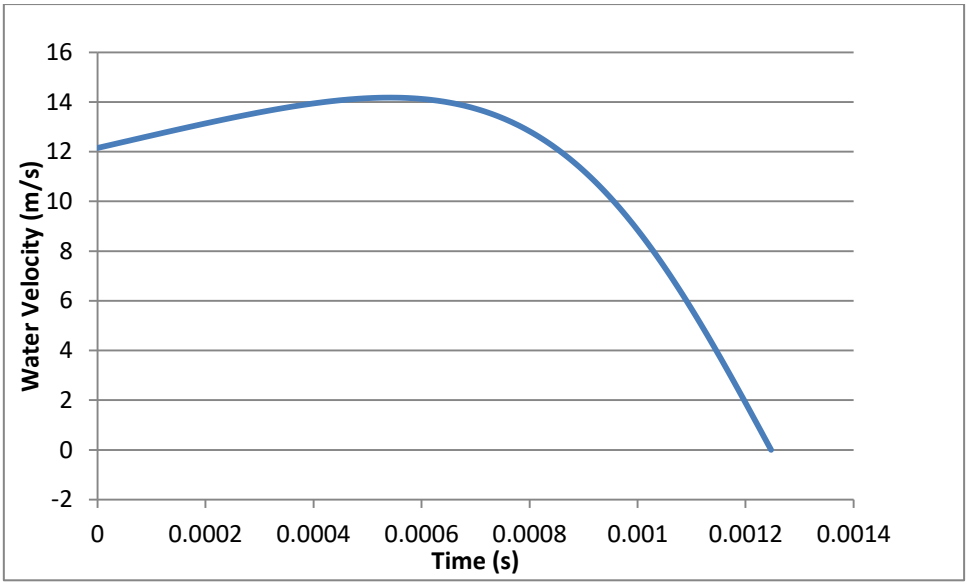

Figure 4-14 Average water velocity under tread

Figure 4.14 presents the average water velocity against time under a 60km/h vehicle velocity and 2mm water depth with a 1mm protrusion height. At the beginning, the water velocity increases with time, but after reaching its peak value, which is around 11 m/s in this case, it decreases and finally reduces to zero.

4.3 Permeable pavement surface

On both a smooth pavement surface and a textured pavement surface, all water is assumed to be expelled to the side of the tyre, whereas in reality some may penetrate into the pavement. Therefore a permeable pavement surface is introduced which is shown in Figure 4.15. It is assumed that part of the water enters the pavement structure through micro-cracks in the surface.

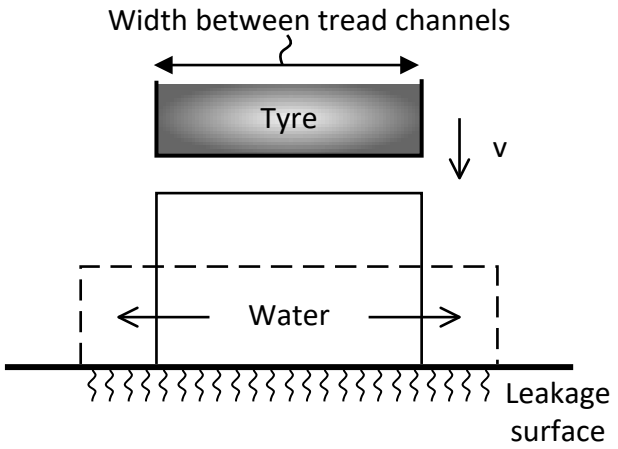

Figure 4-15 Simplified permeable pavement surface

4.3.1 Calculations

Since a 2D problem is considered in this study, a 3D flow problem with flow through tubes needs to be transformed into a 2D format. This can be done by considering an equivalent flow through a square of side S (with its flow represented by Q) shown in Figure 4.16.

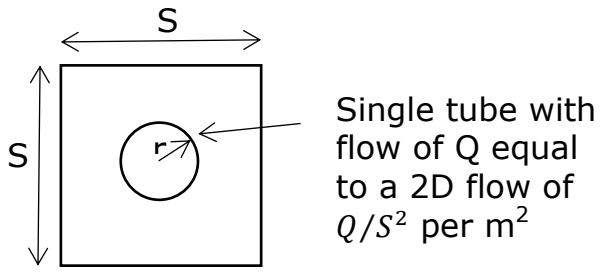

Figure 4-16 Equivalent flow through an area around a tube

According to pipe flow assumptions,

$$Q = K\frac{1}{4}\pi r^2 \frac{\Delta P}{\rho g l_{tube}} \qquad \text{Equation 4-23}$$

where l_{tube} is the length of the tube;

K is the permeability of asphalt for different air void content, using Equations 5.3-5.6 ;

Consider a length of l under the tread,

$$\sum Q_1 = \frac{K\frac{1}{4}\pi r^2 \frac{\sum P}{\rho g l_{tube}}}{S^2} l \times (t_i - t_{i-1}) \qquad \text{Equation 4-24}$$

It is noted that the surface water pressure is used which, however, is not known when calculating the flow into asphalt. Therefore there is no analytical solution for this situation. To solve this problem, the surface water pressure at time t_i is obtained from the pressure calculated at time t_{i-1}.

The total flow Q_{total} that is expelled by the tyre tread is given by:

$$Q_{total} = Vl \qquad \text{Equation 4-25}$$

Thus the water flow Q_2 going to both sides is calculated as:

$$\begin{aligned} Q_2 &= Q_{total} - \sum Q_1 \\ &= Vl - \frac{K\frac{1}{4}\pi r^2 \frac{\sum P}{\rho g l_{tube}}}{S^2} l \times (t_i - t_{i-1}) \end{aligned} \qquad \text{Equation 4-26}$$

Therefore the average water velocity is given by:

$$V_w = Q_2 / h = \frac{Vl}{h} - \frac{K\frac{1}{4}\pi r^2 \frac{\sum P}{\rho g l_{tube}}}{h \bullet S^2} l \times (t_i - t_{i-1}) \qquad \text{Equation 4-27}$$

The new average water velocity is used to calculate the average water acceleration. After that, the new average water acceleration is substituted into Equation 4.14 to calculate the water pressure at this time step.

4.3.2 Results and discussions

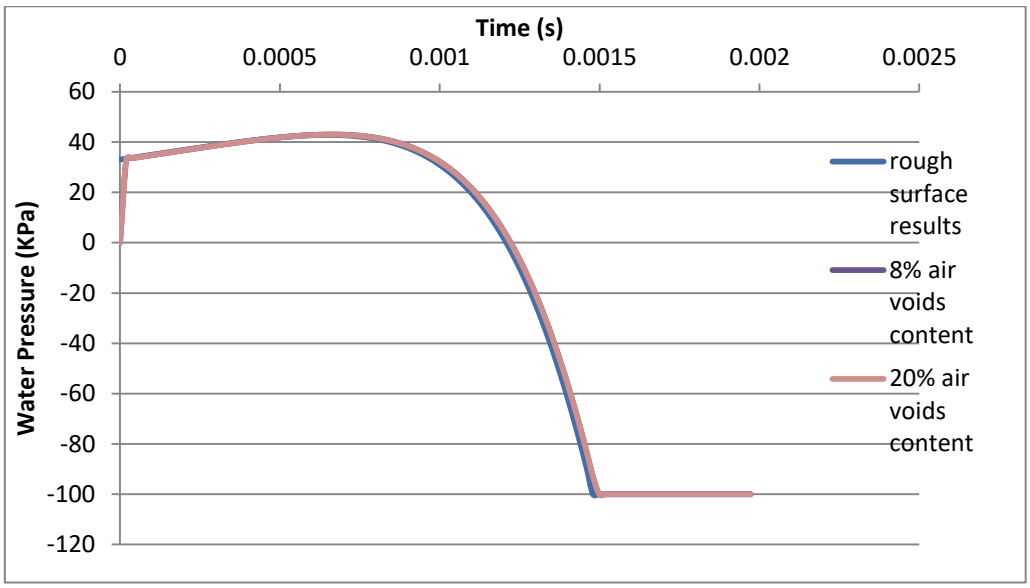

Figure 4-17 Centre point water pressure at different permeability for permeable surface

The results of water pressure at the centre of the tyre with and without consideration of micro-cracks through a rough surface are compared in Figure 4.17. Three values of micro-crack air void content of 0%, 8% and 20% were considered. The case of 0% air void content is used as a reference for the comparison. It can be seen that the permeability of asphalt surface has an insignificant effect on the surface water pressure since the curves in Figure 4.17 representing the three sets of results almost overlie each other. This is due to the relatively small water flow into the pavement which is negligible compared to total water flow.

4.4 Summary

This chapter has presented calculations of surface water pressure for three different types of pavement surface. The first is a smooth surface which does not exist in reality. The results give an idea of how the water

pressure changes with different vehicle velocities. The second type is a textured surface which is assumed to contain protrusions on the surface. Compared to the perfectly smooth surface, this textured pavement surface assumption results are more realistic. The results show that the peak water pressure increases with increasing vehicle velocity or reducing the height of protrusion. The third type is the permeable pavement surface. The results indicate that the permeability of asphalt surface is a secondary effect on the surface water pressure.

Chapter 5. Analytical Modelling of Asphalt Structure

Since the water pressure at the pavement surface can be calculated using the proposed methodology described in the previous chapter, the next step is to understand the water pressure within the asphalt pavement structure. Although an asphalt mixture is very complex, a simplified model will be developed to facilitate calculations.

5.1 Problem Definition

According to the ways that water enters and moves in a pavement, pavements can be classified into the following 6 types (Dawson, 2008):

- Impermeable throughout the construction
- Impermeable surface and structural layers
- Permeable surface over impermeable structural layers
- Permeable throughout with water storage capacity within the structure
- Permeable throughout without water storage capacity
- Cracked or jointed surface layers over permeable lower layers

The second and third types are the most common. While an impermeable surface, such as Portland cement concrete (PCC) surfacing, is designed to provide an impermeable covering to lower pavement layers, water can still penetrate into the pavement through cracks and joints. In fact water can penetrate into most pavement surfaces.

When dealing with moisture damage in pavements, it is very important to understand the internal structure which includes analysing the air voids size and distribution in the pavement. Chen et al. (2004) classified air voids in asphalt mixtures into three categories: effective, semi-effective and impermeable (Figure 5.1).

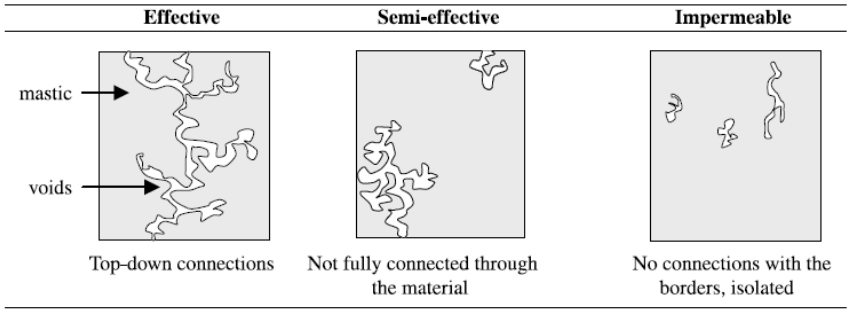

Figure 5-1 Classification of voids in asphalt mixtures (adapted from Chen et al. 2004).

Nowadays air void size and distribution can be analysed using a probabilistic approach with the assistance of X-ray computed tomography and image analysis techniques. Many researchers have found that the air void sizes and the air void content percentages vary with depth. It is found that a higher percentage of air voids is usually concentrated at the top and bottom parts of a layer and the percentage of air voids in the middle region is smaller and relatively more uniformly distributed (Masad et. al., 2002), some examples of which are shown in Figure 5.2 and Figure 5.3.

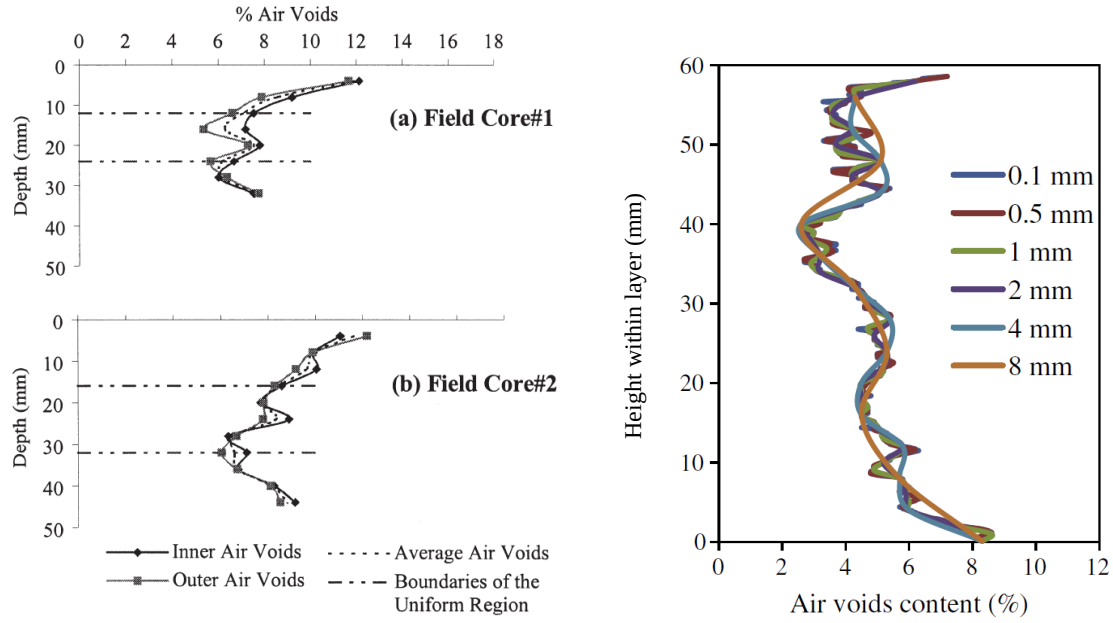

(a) (b)

Figure 5-2 Vertical and horizontal air void distribution in field cores from the top lift of a pavement layer (Tashman, 2002) (b) Analysis of air voids distribution (Hassan，2014)

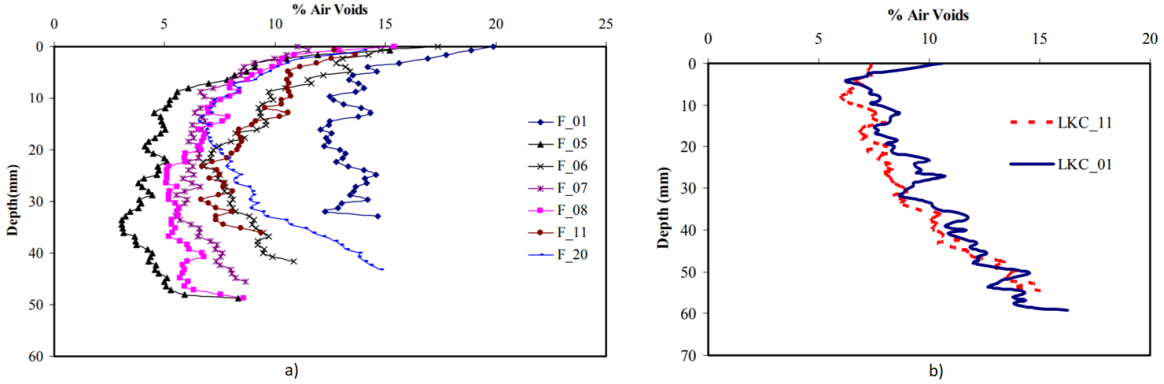

Figure 5-3. a) Air void distribution in field specimens; b) Air void distribution in Linear Kneading Compactor (LKC) specimens (Al Omari, 2005)

In this chapter, which aims to develop analytical models for simulating flowing water through voids and connecting passages, a simplified pavement structure is proposed. This simplified structure is illustrated in Figure 5.4. Although from the above discussions air void size and air void content percentages vary with depth, this simplified internal structure

assumes that the size of all air voids is the same, while some of these air voids are connected by tubes which are uniformly distributed.

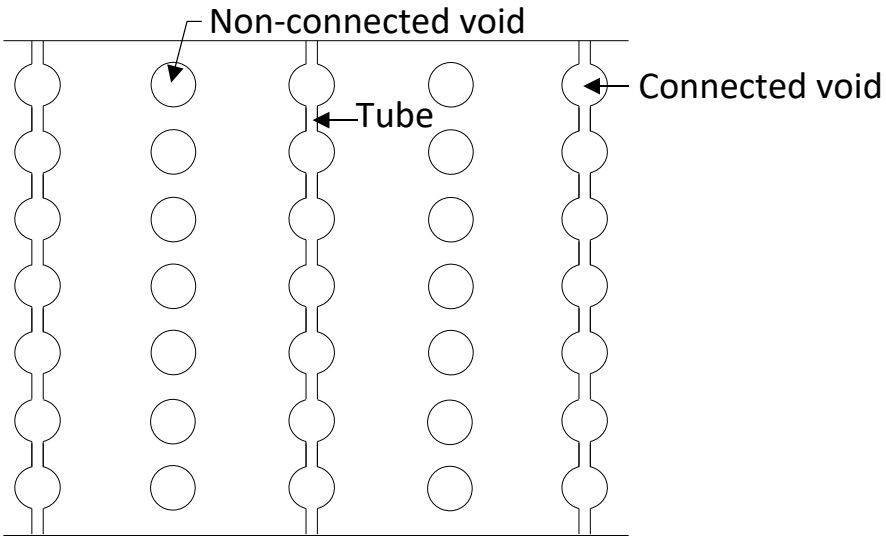

Figure 5-4 Cross-section showing the proposed simplified voids configuration

5.2 Selected Model Parameters

In order to define the simplified structure, the air voids size, connected air voids content and permeability of the asphalt mixture are required.

5.2.1 Air voids size

While it is acknowledged that air voids size, in reality, varies within the asphalt mixture, it is necessary to choose a representative size that can be used in the simplified structure. Based on Masad's (2002) research, a range of air void sizes for a series of asphalt concrete mixtures is shown in Figure 5.5.

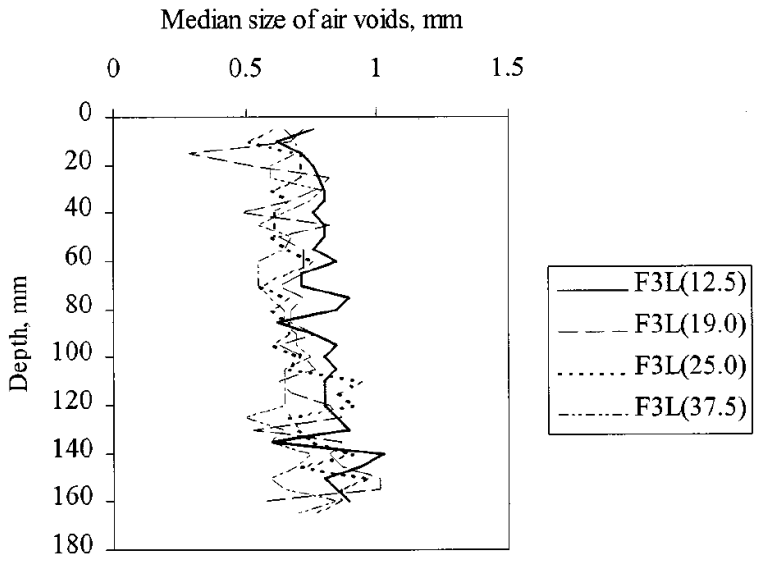

Figure 5-5 Median distribution of air void size with depth in Superpave gyratory compactor compacted specimens with different nominal maximum aggregate size (12.5mm, 19.0mm, 25.0mm, 37.5mm) (Masad, 2002)

However the range of median size is quite tight and a wider range of size will be evaluated in this chapter.

5.2.2 Connected air voids content

Alvarez et al. (2012) have found that the connected air voids (CAV) content, which corresponds to the fraction of air voids (AV) forming connected paths in an asphalt, is better related to the asphalt mixture response (i.e., permeability) than the total AV content.

Table 5.1 below shows their relationship between the total air voids (TAV) content and CAV content for hot and warm mix asphalt mixtures obtained through image analysis (Alvarez et al., 2012).

table 5-1 Compaction temperature and air voids (AV) content of scanned specimens (Alvarez et al., 2012)

Specimen	CT	TAV	CAV	RAT
Road core Hot mix asphalt	NA	7.8	4.3	55.1
Road core Asphamin®	NA	10.3	6.2	60.2
Road core Sasobit®	NA	13.7	11.2	81.7
Road core Evotherm®	NA	10.0	5.3	53
SGC Hot mix asphalt-115mm	121	2.9	1.3	44.8
SGC Asphamin®, 115mm	104	2.9	1.0	34.5
SGC Sasobit®, 115mm	104	2.8	0	0
SGC Evotherm®, 115mm	104	3.2	0	0
SGC Evotherm®, 62mm	80	5.1	0.6	11.7
SGC Evotherm®, 62mm	93	5.2	1.6	30.7
SGC Evotherm®, 62mm	104	5.2	1.3	25
SGC Evotherm®, 62mm	121	5.2	2.6	51

Note: SGC = Superpave Gyratory Compactor; Asphamin®, Sasobit®, Evotherm® = warm mix additives; CT = compaction temperature (℃); TAV = total air voids content (%); CAV = connected air voids content (%); RAT = ratio of CAV to TAV values; NA = not available

From this table the relationship of CAV and TAV shown in Figure 5.6 for road cored specimens can be assumed as following:

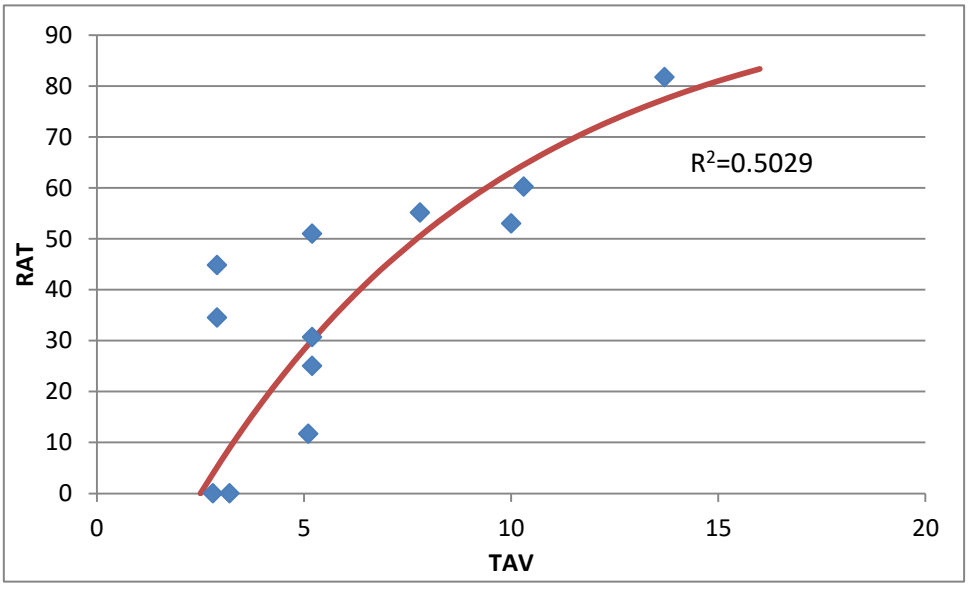

Figure 5-6 Relationship between TAV and RAT (data from Alvarez et al., 2012)

$$RAT = 100 \times (1 - 1.142^{-(TAV-2.5)}) \qquad \text{Equation 5-1}$$

Hence the CAV is given as:

$$CAV = \frac{RAT \times TAV}{100} \qquad \text{Equation 5-2}$$

5.2.3 Permeability of the asphalt mixture

The relationship between field permeability and air voids developed by Cooley et al. (2002) was used in this study. They developed relationships for different nominal maximum aggregate size (NMAS). An example is shown in Figure 5.7 for 12.5 mm NMAS mixes. A total of eight HMA mixes were tested and a fairly high R^2 value found (0.64). The "best-fit" equation used to describe asphalt permeability at different air voids contents is given by.

$$y = 0.0047x^{4.8672} \qquad \text{Equation 5-3}$$

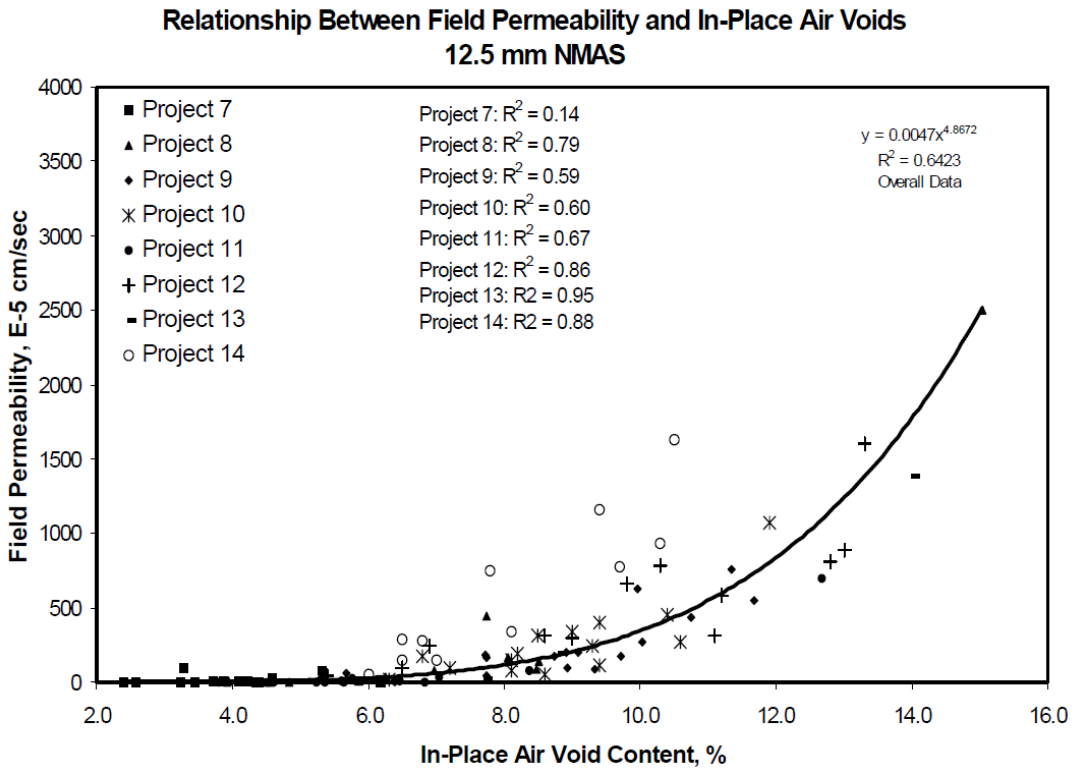

Figure 5-7 Relationship between permeability and density ~ 12.5 mm NMAS mixes (Cooley et al., 2002)

As well as the 12.5mm NMAS, they also tested other sizes, namely 9.5mm, 19.0mm and 25.0mm, the best fit lines for which are shown in Figure 5.8 below. The resulting equations are as follows.

For 9.5mm NMAS:

$$y = 0.0054x^{4.9098} \qquad \text{Equation 5-4}$$

For 19.0mm NMAS:

$$y = 0.0936x^{4.2145} \qquad \text{Equation 5-5}$$

For 25.0mm NMAS:

$$y = 0.6739x^{3.7721} \qquad \text{Equation 5-6}$$

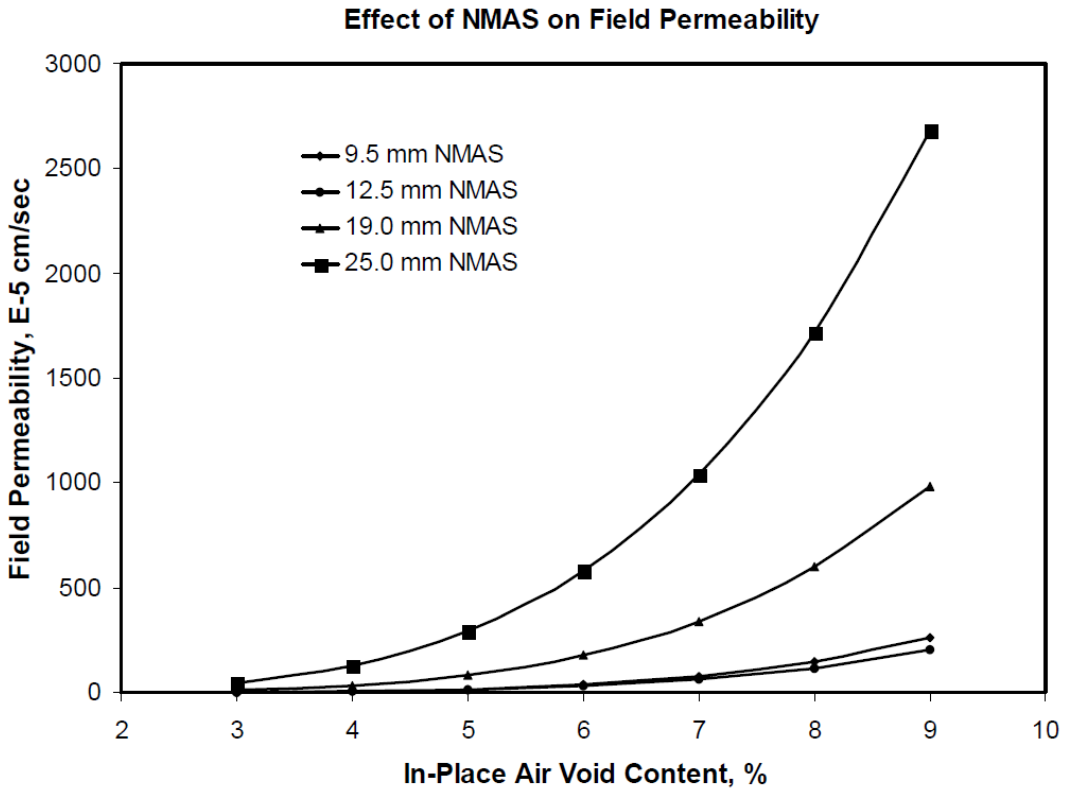

Figure 5-8 Relationship between Permeability and Density for different NMAS Mixes (Cooley, 2002)

5.3 Selection of Voids Geometry

Only the connected air voids content percentage was used to determine the appropriate geometry. Because it is assumed that the connected tube diameter is relatively smaller than the void diameter (see Figure 5.2), when calculating the total air voids content, the tube area was ignored. The variable 'D' is used to denote the diameter of the voids and 'd' for the tubes.

The distance between CAV voids horizontally is termed 's' in the calculation. Figure 5.9 gives examples of asphalt CT images. From these images it can be seen that the distance between two voids is closely related to the aggregate size. Taking some of the asphalt CT images as

examples, the average spacing of the voids is generally calculated from the ratio of void numbers and overall area. The results are scattered and distribute around half of the NMAS. Therefore in this study, the average distance from the edge of two voids is assumed to be half of the NMAS.

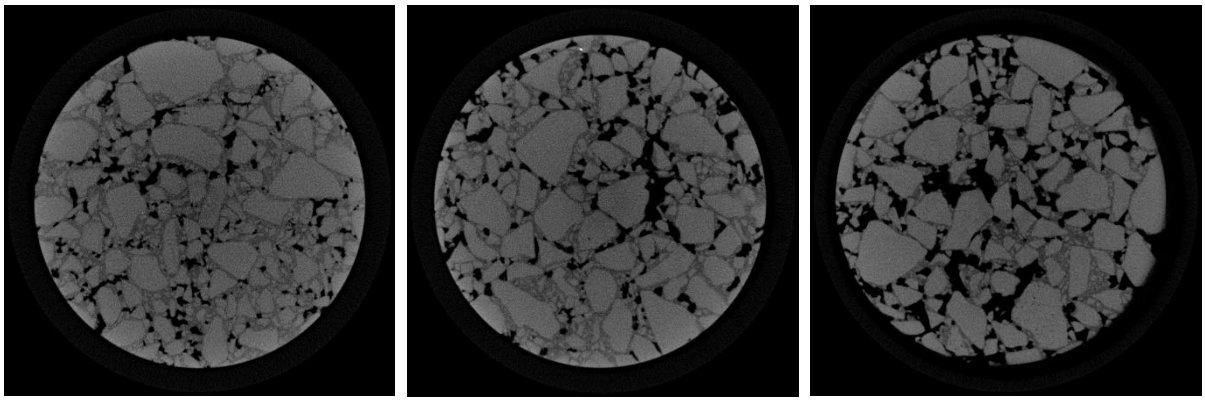

Figure 5-9 Asphalt CT images air voids content 5%, 10% and 17% respectively (Aboufoul, 2015)

The vertical spacing between two CAV voids is 'z'. Assuming that there are a total of 'a' voids along a length 'L', 'b' along a width 'W' and 'c' along a depth of 'Z', Figure 5.10 shows a schematic diagram of the structure.

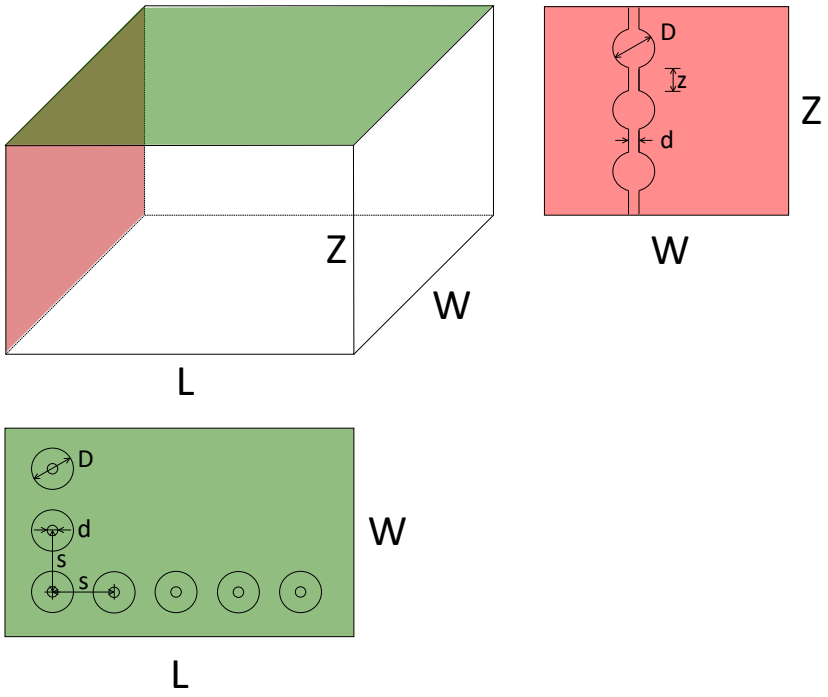

Figure 5-10 Schematic diagram of simplified pavement structure

For a given material, it is assumed that the NMAS and the TAV content are known. Therefore based on the information from the previous section, the connected air voids content 'n', permeability 'K', void diameter 'D' and the distance between two voids 's' values were used as input parameters.

Hence:

$$c = \frac{Z}{z + D} \qquad \text{Equation 5-7}$$

$$a = \frac{L}{s} \qquad \text{Equation 5-8}$$

$$b = \frac{W}{s} \qquad \text{Equation 5-9}$$

Balancing the total voids volume with the CAV content, the CAV content n can be calculated as:

$$n = \frac{\frac{4}{3}\pi(\frac{D}{2})^3 \cdot c \cdot a \cdot b}{W \cdot L \cdot Z} \qquad \text{Equation 5-10}$$

Substituting a, b and c:

$$n = \frac{\frac{4}{3}\pi(\frac{D}{2})^3 \cdot \frac{Z}{z+d} \cdot \frac{L}{s} \cdot \frac{W}{s}}{W \cdot L \cdot Z}$$

$$n = \frac{\pi D^3}{6(z+D)s^2} \qquad \text{Equation 5-11}$$

Therefore the vertical spacing between two CAV voids z can be given as:

$$z = \frac{\pi D^3}{6ns^2} - D \qquad \text{Equation 5-12}$$

Then from Newton's equation of viscosity, the mean water velocity $\overline{V}$ in the tube is:

$$\overline{V} = \frac{\Delta P}{c \cdot z}\frac{d^2}{32\mu} \qquad \text{Equation 5-13}$$

where ΔP is the pressure difference from asphalt surface to bottom; μ is the dynamic viscosity of water (White, 1999).

And based on Darcy's law, the total flow through the tube Q_{tube} is:

$$Q_{tube} = \overline{V} \cdot A_{tube} = \frac{\Delta P}{c \cdot z}\frac{d^2}{32\mu}\frac{1}{4}\pi d^2 = \frac{\Delta P \pi d^4}{128\mu \cdot c \cdot z} \qquad \text{Equation 5-14}$$

where A_{tube} is the area of the cross section of the tube;

The permeability K is then calculated below:

$$K = \frac{Q_{tube} a \cdot b \cdot Z}{\Delta H A_{total}} = \frac{\frac{\rho g \Delta H \pi d^4}{128\mu \cdot \frac{Z}{z+D} \cdot z} \cdot \frac{L}{s} \cdot \frac{W}{s} \cdot Z}{\Delta H \cdot L \cdot W} = \frac{\rho g \pi d^4 (z+D)}{128\mu \cdot s^2 \cdot z} \qquad \text{Equation 5-15}$$

where ΔH is the total length of tube; A_{total} is the total area of the cross section of the asphalt element;

Therefore the diameter of tube d is given by:

$$d^4 = \frac{128K\mu \cdot s^2 \cdot z}{\rho g \pi (z + D)} \qquad \text{Equation 5-16}$$

The diameter of tube 'd' and the spacing between two voids 'z' can be calculated based on Equations 5.12 and 5.16. An example of the calculation based on Equations 5.7 to 5.16 is shown in Table 5.2 below, relating to a 12.5mm asphalt concrete with 8% total air voids.

Table 5-2 Example calculation

Input	Value	Description	Output	Value	Description
$D(mm)$	1.5	Diameter of Voids	$z(mm)$	0.267146	Spacing between Voids
$s(mm)$	5	Distance between Voids	$d(mm)$	0.116404	Diameter of Tubes
n	0.04	Connected Air Voids Content			
$k(m/s)$	1.16847E-05	Permeability			
$\mu(Ns/m^2)$	0.001	Dynamic Viscosity			
$g(N/kg)$	9.8	Gravitational Acceleration			
$\rho(kg/m^3)$	1000	Density of water			

5.4 Fully and Partially Saturated Voids

To begin with, all the voids and tubes are assumed fully saturated with water. The water flow is assumed to be laminar. It is known that Reynolds number distinguishes laminar and turbulent flow.

$$\mathrm{Re} = \frac{\rho u L}{\mu} \qquad \text{Equation 5-17}$$

where: ρ is the density of the fluid (kg/m^3), u is the velocity of the fluid with respect to the object (m/s), L is a characteristic linear dimension (m), μ is the dynamic viscosity of the fluid (Pa·s or N·s/m^2 or kg/m·s)

Water flow with a Reynolds number less than 2000 is laminar and over 4000 is turbulent. The Reynolds number of these simplified asphalt structures has been checked and found to be typically in the range 1200 to 2500. Although some of the flow is transitional, the equations for laminar flow are still approximately applicable.

Table 5-3. Typical Reynolds number value under different water velocity

u	12	13	14	16	18	20	22	24
Re	1221.053	1322.807	1424.561	1628.07	1831.579	2035.088	2238.596	2442.105

The water pressure calculated in chapter 4 is used here as the surface water pressure. In the saturated case, the distribution of pressure drop along the tubes is linear and it is assumed that there is no pressure loss in the voids. Also a "zero-pressure" assumption was made at the bottom of the asphalt layer.

Hence, for saturated conditions:

$$P_1 = \frac{P}{l_{tube}} \frac{d^2}{32\mu} z_1 \qquad \text{Equation 5-18}$$

Where P_1 is the pressure at the first void

P_1 is the pressure at the surface

l_{tube} is the total tube length

d is the diameter of tube

z_1 is the depth of the first void

The next step is to calculate under partially saturated conditions. The air inside the partially saturated voids is compressed by the pressure. Based on the Boyle–Mariotte law, the air in the voids is assumed an ideal gas and the temperature remains the same. It is assumed that the original air

volume 'V_0' in each void is the same and can be calculated by the saturation percentage. Figure 5.11 shows a schematic diagram of the structure.

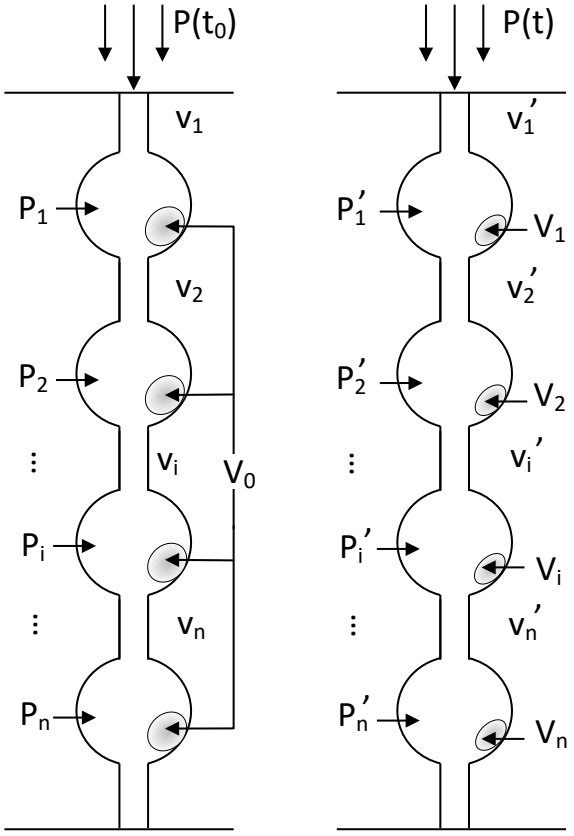

Figure 5-11 Structure schematic diagram of water flow

Then

$$(P_1 + P_{atm})V_0 = (P_1^{'} + P_{atm})V_1 \qquad \text{Equation 5-19}$$

where P_1 is the pressure at the first void

P_{atm} is the atmospheric pressure

V_0 is the original air volume in the void

$P_1^{'}$ is the new pressure after compression at the first void

V_1 is the new air volume after compression in the void

The volume change is based on the flow change

$$V_0 - V_1 = (v_1 - v_2)\pi \frac{d^2}{4}(t_1 - t_0) \qquad \text{Equation 5-20}$$

where V_0 is the original air volume in the void

V_1 is the new air volume after compression in the void

v_1 is the water velocity before the first void

v_2 is the water velocity after the first void

d is the diameter of tube

t is the time

According to these equations the different water pressures in different voids can then be calculated. The following results show an example for a 0.015m thickness asphalt and ten voids through the depth. Although this thickness is a bit less for a real pavement surface, the results show a similar trend with different asphalt thickness.

5.5 Results and Discussions

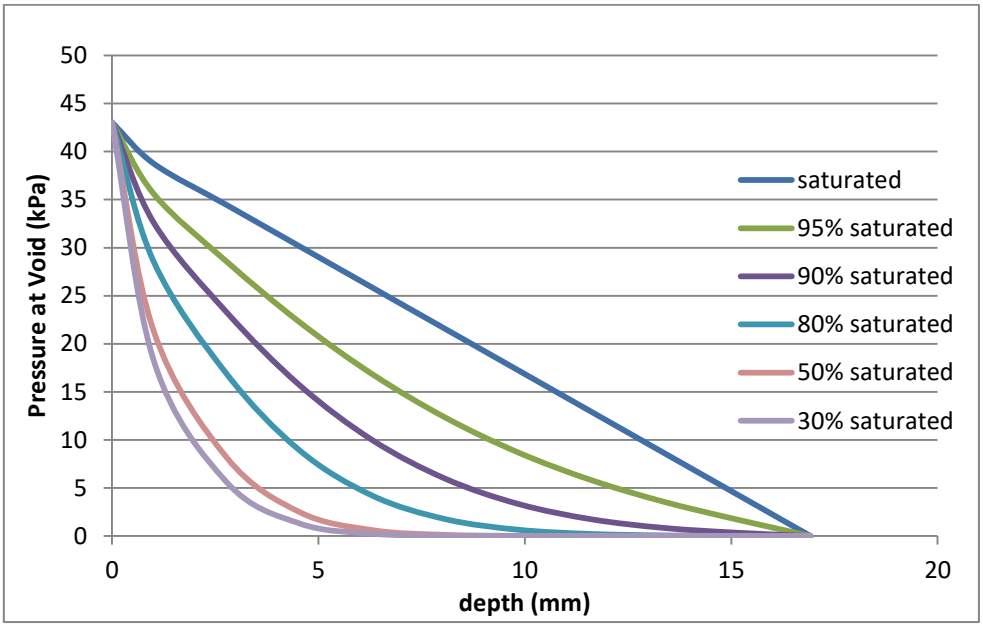

Figure 5-12 Peak water pressure distribution in asphalt pavement

It can be seen from Figure 5.12 that the water pressure experiences a significant decrease when the voids are not fully saturated. The rate at which the water pressure drops with depth becomes lower with decreasing saturation percentage. There exists a threshold depth at which the gradient of drop of water pressure experiences a sharp change. The threshold point is much closer to the surface if it is less saturated. The threshold point is close to the 8mm (fifth void counting downward from the surface) for 95% saturation whereas it is at about the 6mm (fourth void) for 93% saturation. Moreover for all partially saturated voids, the water pressure dropped quicker near to the surface than at depth.

5.6 Summary

This chapter has shown a step-by-step calculation of the water pressure in the voids within an asphalt structure. In order to calculate the pressure, a simplified voids structure has been proposed. After estimating the voids diameter 'D', connected air voids content 'n', permeability 'K' and the distance between two void centres 's', the remaining geometry of the structure can be determined. Once the structure is defined, the water pressure for the fully saturated voids is then calculated using Darcy's law. For partially saturated voids, the water pressure inside the voids can also be calculated. These water pressures inside the voids are used in the next chapter to evaluate crack initiation and propagation within the asphalt structure using cavity expansion theory.

Chapter 6. Crack Initiation and Propagation within the Asphalt Structure

The previous two chapters have addresses the issues of the surface water pressure and a simplified asphalt internal structure. The subject of how to use these parameters to predict asphalt damage, such as crack initiation and propagation, is introduced in this chapter. Loss of bitumen-aggregate adhesion is also one of the main mechanisms of crack initiation and it will be covered briefly here. However the main methodology that has been chosen to calculate the stress and strain from a given internal pressure is cavity expansion. An asphalt cracking law will then be used to estimate crack propagation rate.

6.1 Loss of bitumen-aggregate adhesion

It is found in the literature that high tensile localized stresses near the edges of compressed air voids can lead to the growth of cracks (Zhang et al. 2014). With the presence of water, this process will be accelerated. And the mechanics of the bonding at the aggregate-binder interface, which is highly affected by moisture conditions, influences the response of the asphalt mixture to different distress types. In this section, the mechanism for loss of adhesion between the aggregate and bitumen film is addressed using a simplified calculation.

Looking at a single aggregate particle, it is coated with a thin bitumen film which is typically about 15-25 micrometres thick (Read et al., 2003). If a micro-crack or any localised damage occurs in the bitumen film, it allows water to get into the area between the bitumen film and the aggregate. An infinitesimal element (see Figure 6.1) of the bitumen film was used to calculate the localized stresses. The assumed simplified structure and the stresses acting on it are shown in Figure 6.1. The following is a simplified analysis of those stresses.

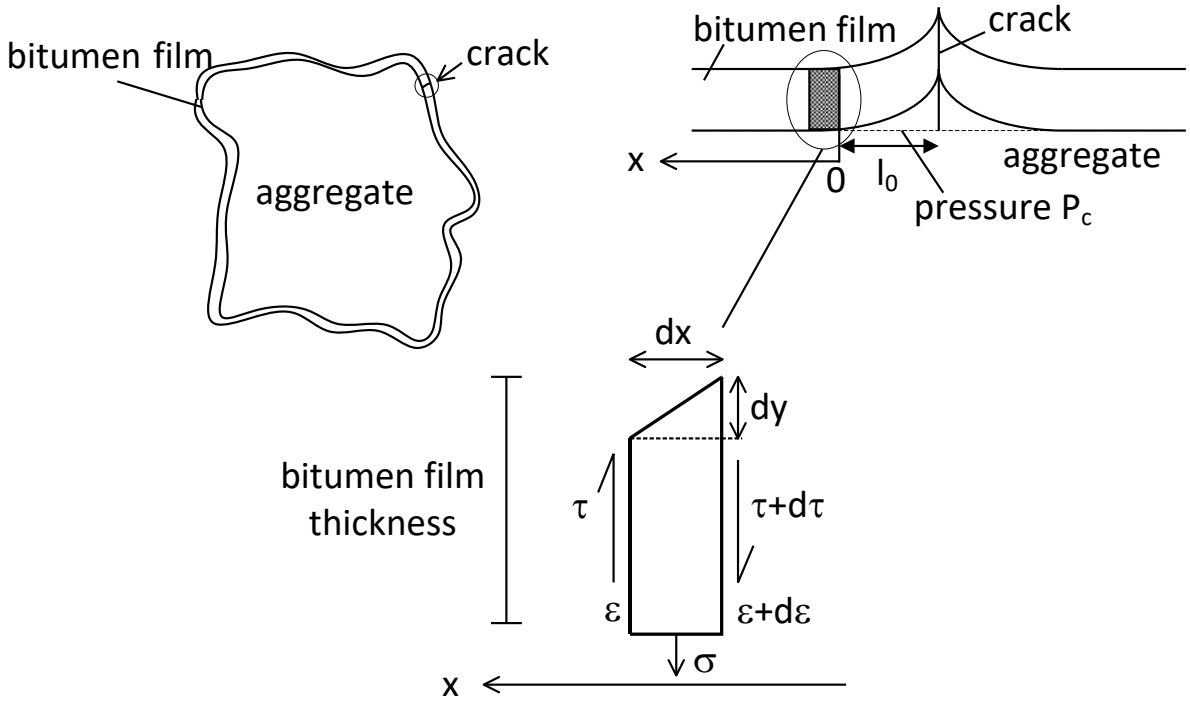

Figure 6-1 Schematic showing the simplified model for simulating de-bonding of aggregate and bitumen film

Based on Hooke's Law, the average strain in the bitumen element shown is given by:

$$\varepsilon(x) = \frac{\sigma(x)}{2E}$$

Equation 6-1

where E is the Young's modulus of bitumen. Equilibrium then gives:

$$\sigma(x)dx = d\tau(x)h_b \qquad \text{Equation 6-2}$$

where h_b is the thickness of the bitumen film.

Substituting Equation 6.1 into 6.2 we obtain:

$$2E\varepsilon(x) = \frac{d\tau(x)}{dx}h_b \qquad \text{Equation 6-3}$$

Differentiating both sides of Equation 6.3 with respect to x

$$2E\frac{d\varepsilon(x)}{dx} = h_b\frac{d^2\tau(x)}{dx^2} \qquad \text{Equation 6-4}$$

By definition the average shear strain is given by:

$$\frac{1}{2}\frac{dy}{dx} = \frac{\tau(x)}{G} \qquad \text{Equation 6-5}$$

where G is the shear modulus;

Also by definition:

$$\frac{dy}{dx} = \frac{d\varepsilon(x)h_b}{dx} \qquad \text{Equation 6-6}$$

Combining Equation 6.5 and 6.6 then substituting into Equation 6.4:

$$2E\frac{2}{Gh_b}\tau(x) = h_b\frac{d^2\tau(x)}{dx^2} \qquad \text{Equation 6-7}$$

Solving the above equation gives:

$$\tau(x) = C_1 e^{x\sqrt{\frac{8(1+\upsilon)}{h_b^2}}} + C_2 e^{-x\sqrt{\frac{8(1+\upsilon)}{h_b^2}}} \qquad \text{Equation 6-8}$$

where υ is the Poisson's ratio; C_1 and C_2 are constants and can be calculated using the boundary conditions.

Based on the assumption $\tau(0) = P_c l_0 / h_b$ when $x = 0$ and $\tau'(\infty) = 0$ when $x = \infty$, where P_c is the pressure in the crack and l_0 is the distance from crack to the connected point, then from Equation 6.2:

$$\begin{aligned}\sigma(x) &= \frac{d_{\tau(x)}}{d_x} \cdot h_b \\ &= h_b \sqrt{\frac{8(1+\upsilon)}{h_b^2}} C_1 e^{x\sqrt{\frac{8(1+\upsilon)}{h_b^2}}} - h_b \sqrt{\frac{8(1+\upsilon)}{h_b^2}} C_2 e^{-x\sqrt{\frac{8(1+\upsilon)}{h_b^2}}} \\ &= \sqrt{8(1+\upsilon)} C_1 e^{x\sqrt{\frac{8(1+\upsilon)}{h_b^2}}} - \sqrt{8(1+\upsilon)} C_2 e^{-x\sqrt{\frac{8(1+\upsilon)}{h_b^2}}}\end{aligned} \qquad \text{Equation 6-9}$$

According to the above equations the stress distribution in the bitumen film can be calculated. An example calculation is shown in the Table 6.1 below.

Table 6-1 Example calculation of loss of bitumen-aggregate adhesion

Input	Value	Description	Output	Value	Description
$P_c(kPa)$	42.5	Pressure in the Crack	$\sigma(kPa)$	515.4	Stress at Connected Point
$l_0(mm)$	0.07	Distance from Crack to Connected Point			
$h_b(mm)$	0.02	Bitumen Film Thickness			
υ	0.5	Poisson's Ratio			

The pressure in the crack used here is based on the peak water pressure under 60km/hour vehicle velocity and 1mm protrusion height. The Poisson's ratio is chosen to be 0.5 for pure bitumen (Read et al., 2003). In this case, the stress at the connected point is calculated to be 515.4kPa with a 42.5kPa pressure in the crack. To put this in context, the bitumen and aggregate bond strength is typically around 1MPa; however it is highly dependent on the temperature and the loading rate (Zhang, 2015). Although in this example the pressure is not high enough to do any damage to the bond between the bitumen and aggregate, the stress is reasonably high compared to the input pressure value. But as Kringos (2007), predicted the bond strength is around 0.6MPa when moisture content reaches 5%. Therefore, the bond strength is low enough to damage the bond under certain moisture conditions. These calculations give a brief idea of what water pressure can potentially achieve at the connected point near the crack. Figure 6.2 below shows the relationship between connected stress and distance from crack to connected point under the same bitumen film thickness of 0.02mm.

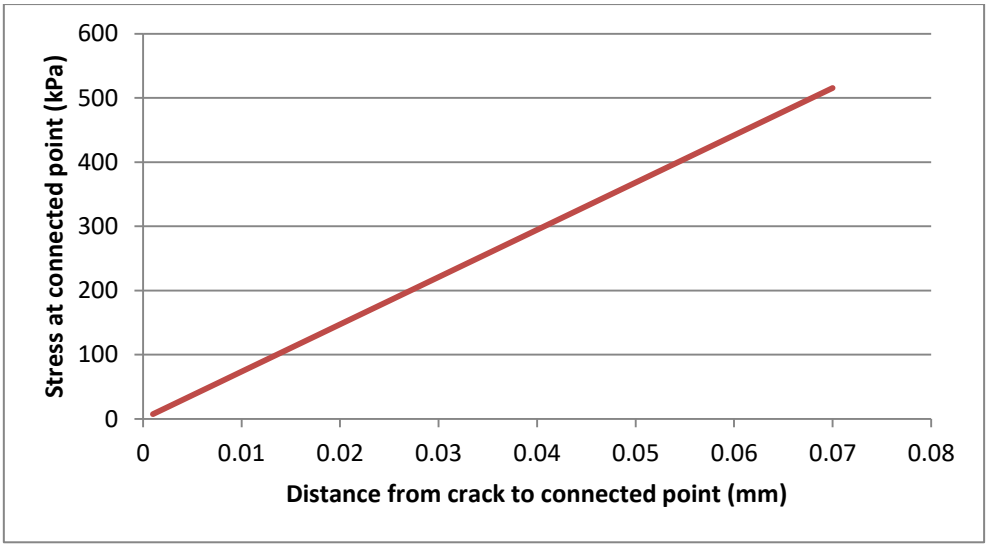

Figure 6-2 Relationship between connected stress and distance from crack to connected point

6.2 Debonding between asphalt layers

The same equations can also be applied to calculating the de-bonding stress between asphalt layers by changing the input parameters. In that case, the bitumen film and the aggregate in Figure 6.1 are replaced by two asphalt layers which are originally bonded to each other. An example calculation using Equation 6.9 is shown in Table 6.2 below.

Table 6-2 Example calculation of debonding of asphalt layers

Input	Value	Description	Output	Value	Description
$P_c(kPa)$	42.5	Pressure in the Crack	$\sigma(kPa)$	23.2	Stress at Connected Point
$l_0(mm)$	5	Distance from Crack to Connected Point			
$h_b(mm)$	30	Layer Thickness			
υ	0.35	Poisson's Ratio			

It can be seen that in this case the pressure at the connected point is 23.2kPa which is quite small compare to that in previous case (value of 515.4 kPa). This therefore indicates that debonding will only happen

under this mechanism with a very high water pressure (value near to the bond strength between layers). The relationship between connected stress and distance from crack to connected point under the same asphalt layer thickness of 30mm is presented in Figure 6.3 below. It should be noted that the debonding strength between asphalt layers is affected not only by the effective confining pressure but also by the moisture content and temperature. The pressure at connecting points is mainly affected by the pressure at the adjacent crack, the crack-to-connecting point distance, and the bitumen layer thickness. Given the uncertainties of these variables, it is difficult to come to a simple conclusion as to whether the pressure at a connecting point exceeds the stripping strength of the interface between bitumen layers or not. Specially designed scenarios and associated laborotory experiments and/or computer simulations should be developed in future studies to validate and calibrate the simple analytical model derived here in this chapter.

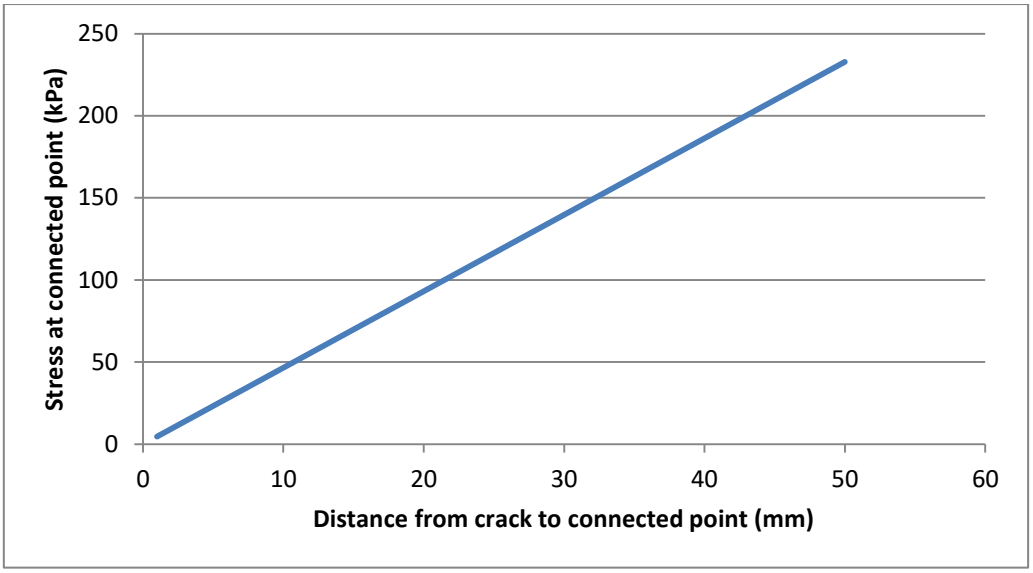

Figure 6-3 Relationship between connected stress and distance from crack to connected point for debonding

6.3 Asphalt crack propagation law

As cracking can occur in nearly every type of asphalt mixture, a number of studies have been made to obtain a better understanding of cracking mechanisms. In 1961, Paris et al. (1961) suggested to use the Irwin stress intensity factor (ΔK) to characterize the rate of crack advance per cycle da/dN, which is now known as Paris law (Equation 6.10). Since then, much work has been done to understand more about Paris law and its possible application to asphalt.

$$\frac{da}{dN} = C\Delta K^{m} \qquad \text{Equation 6-10}$$

Where: a is crack length;

N is number of loading applications;

ΔK is the range of stress intensity factor;

C , m are parameters that depend on material, stress ratio, temperature, etc.

However Paris law is most commonly used in predicting cracking in metals, and it matches well with experimental data. But asphalt is quite different from metals. Based on Pell and Cooper's (1975) findings and the findings of numerous subsequent researchers, the fatigue life of asphalt has a unique relationship with tensile strain (ε_t). Thom (2000) suggested an asphalt crack propagation law that relates the strain to the crack propagation rate rather than the overall fatigue life. This 'law' can be expressed as a simple equation:

$$\frac{dc}{dN} = A\varepsilon_t^n \qquad \text{Equation 6-11}$$

where c is crack length;

N is number of load applications;

ε_t is the tensile strain 'in the region of' the crack tip;

A and n are constants which can be calculated from the failure equation using data from the Indirect Tensile Fatigue Test (ITFT).

In order to calculate these two constants the following calculations are necessary.

First of all, based on Thom's (2008) calculations, the tensile strain 'in the region of' a crack (initially microcrack) tip is about 2.63 times the average strain in the ITFT, and the specimen fails rapidly once the crack length c reaches about 40 percentage of the specimen diameter. Integrating Equation 6.11:

$$\int_0^{40\%\Phi} dc = \int_0^N A(2.63\varepsilon_{av})^n dN \qquad \text{Equation 6-12}$$

where Φ is the diameter of ITFT sample.

And then the following equation can be obtained:

$$\varepsilon_{av} = \frac{1}{2.63}\left(\frac{40\%\Phi}{A}\right)^{\frac{1}{n}} N^{-\frac{1}{n}} \qquad \text{Equation 6-13}$$

A typical relationship found from the ITFT is given by:

$$\varepsilon_t = k_1 N^{k_2} \qquad \text{Equation 6-14}$$

where k_1, k_2 are mixture dependent constants.

Comparing Equation 6.13 and 6.14:

$$k_1 = \frac{1}{2.63}\left(\frac{40\%\Phi}{A}\right)^{\frac{1}{n}} \qquad \text{Equation 6-15}$$

$$k_2 = -\frac{1}{n} \qquad \text{Equation 6-16}$$

Therefore:

$$n = -\frac{1}{k_2} \qquad \text{Equation 6-17}$$

$$A = \frac{40\%\Phi}{(2.63k_1)^n} \qquad \text{Equation 6-18}$$

Constants A and n are then easily calculated with a known k_1 and k_2.

Many researchers have carried out ITFT tests with many different asphalt mixtures (Kennedy 1977, Cocurullo et al. 2008, Buttlar 1994); in this study, the data from Read (1996) has been used. Table 6.1 shows the test data from Read for different asphalt mixture types.

Table 6-3 ITFT test results from Read (1996)

MIXTURE TYPE	EQUATION FOR FAILURE CHARACTERISTIC
30/14 HRA	$\varepsilon = 4322N^{-0.264}$
10mm AC	$\varepsilon = 1362N^{-0.224}$
SMA	$\varepsilon = 2950N^{-0.298}$
20mm DBM	$\varepsilon = 1562N^{-0.246}$

Note: HRA = Hot Rolled Asphalt, AC = Asphalt Concrete, SMA = Stone Mastic Asphalt, DBM = Dense Bitumen Macadam.

So based on the equations in Table 6.3 the two constants A and n are calculated as shown in Table 6.4.

Table 6-4 Example values of A and n

MIXTURE TYPE	k1	k2	A	n
30/40 HRA	4322	-0.264	1.73694E-17	3.787879
French 0/10mm	1362	-0.224	5.43745E-18	4.464286
SMA	2950	-0.298	3.54091E-15	3.355705
20mm DBM	1562	-0.246	8.17485E-17	4.065041

Having determined the two parameters A and n, the asphalt crack propagation law can be used. The next step is to calculate a tensile strain in the pavement to analyse the crack propagation.

As discussed in the previous chapter tyre movement on the pavement with the presence of water on the surface results in a distribution and reduction of water pressure throughout the pavement thickness. Due to high pressure in the voids within the pavement structure, high tensile

stresses can potentially be generated at the edge of the voids. Therefore it is safe to assume that asphalt deteriorates quicker with a higher pressure in the void. In order to obtain the tensile strain at the edge of the voids with different water pressures, linear elastic cavity expansion solutions will be employed, as briefly introduced in the next section.

6.4 Elastic cavity expansion solutions

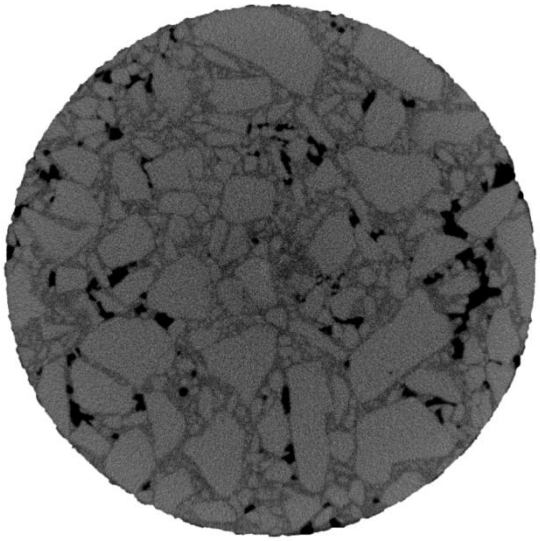

Figure 6-4 Example of asphalt cross-section CT image (the black areas represent voids) (Aboufoul, 2015)

In reality, the size and shape of air voids in the asphalt are not regular (for example as shown in Figure 6.4) and vary with aggregate gradation, mixture type etc. For simplicity, the shapes of voids in a typical section will be treated as circular or elliptical in this research. Although asphalt mixture has viscoelastic properties, nevertheless many researchers, e.g. Majidzadeh et al. (1971), Abdulshafi et al. (1985) and Jacobs et al. (1996), have treated the asphalt mixture as elastic and obtained good

results. Moreover as calculated in the previous chapters, the duration of the water pressure pulse is very short which means the bitumen behaviour will be close to purely elastic. Therefore liner elastic theory is used here. Considering the difference in cavity shapes, corresponding elastic cavity expansion solutions are employed.

6.4.1 Expansion of an elliptical cavity

In the simplified model for an expanding void, it is assumed that an elliptical cavity is subject to a uniform pressure at the inner cavity wall (as shown in Figure 6.5)and that it deforms in a large space (compared to the void size). In addition, compared to the internal water pressure, the influences from other far-field stresses are negligible.

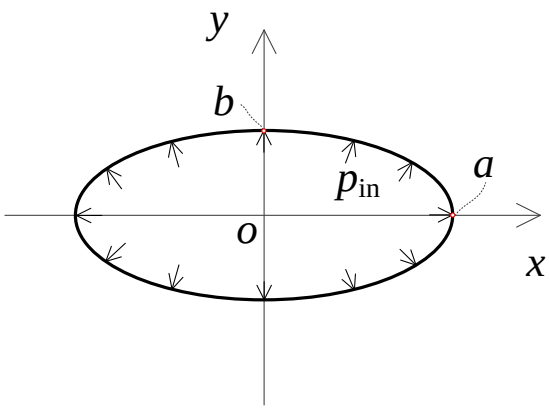

Figure 6-5 Definition of stress boundary condition

According to the defined geometry and stress boundary conditions, this problem can be solved analytically in curvilinear coordinates (Inglis, 1913) or by using the complex variable theory and conformal mapping technique (Muskhelishvili, 1963; Stevenson, 1945) when the solid is described by a linear elastic model. These solutions have been

successfully applied in studying the crack propagation and stress concentration phenomena (Chang and Wu, 1980; Griffith, 1921; Maugis, 1992; Savin, 1970). The solution proposed by Muskhelishvili (1963) on the basis of complex variable theory and conformal mapping technique is followed in this research.

The conformal mapping technique provides a powerful analytical tool for coordinate transformation. It enables us to deal analytically with many boundary value problems with various geometry and stress boundary conditions. $\omega(\zeta)$ represents the conformal mapping function in terms of the complex variable ζ ($\zeta = \xi + i\eta = \rho e^{i\psi}$; $i = \sqrt{-1}$. see Fig.6.6). It is a single-valued transformation relation (as shown in Fig.(6-6)) which maps the points of a region in the physical plane (z-plane) onto points of a region in the phase plane(ζ -plane). The transformation between these two planes is one-to-one and invertible (corresponding inverse transformation $\zeta = \omega^{-1}(z)$), and it preserves angles locally. A conformal mapping relation will be built when these requirements are completely satisfied. More relevant discussions refer to the monographs of Muskhelishvili (1963) and England (2003). It is well-known that the mapping function for an ellipse is

$$z = x + iy = \omega(\zeta) = R(\zeta + \frac{m}{\zeta})$$

Equation 6-19

where $R = (a+b)/2$, $m = (a-b)/(a+b)$. a and b are the semi-major and semi-minor of given ellipse respectively. $\overline{\omega(\zeta)}$ is the conjugate of $\omega(\zeta)$. This becomes

$$\overline{\omega(\zeta)} = R(\frac{\rho^2}{\zeta} + \frac{m\zeta}{\rho^2})$$

Equation 6-20

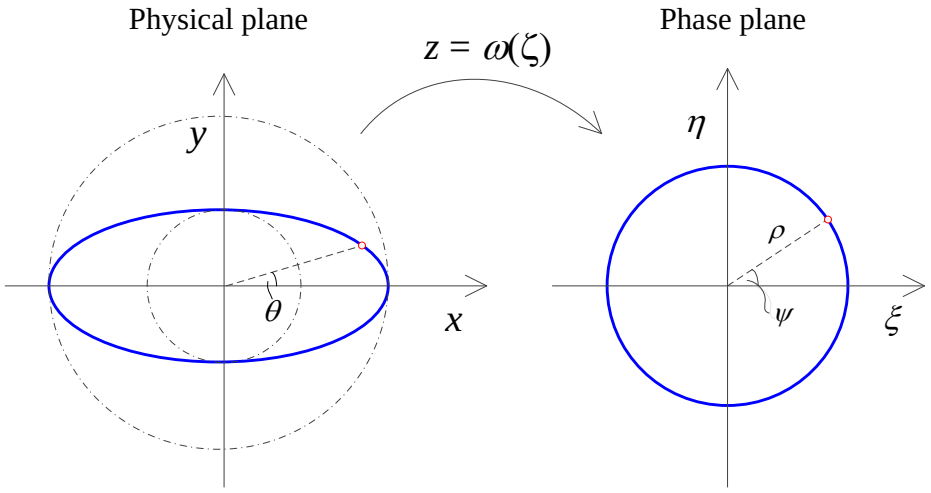

Figure 6-6 Transformation between planes

The corresponding positions of points between the phase plane and the physical plane can be related by Eqs. 6.21 and 6.22.

$$x = R(\rho + \frac{m}{\rho})\cos\psi$$

Equation 6-21

$$y = R(\rho - \frac{m}{\rho})\sin\psi$$

Equation 6-22

With the above conformal mapping function (i.e. Eq.6.19) and the defined boundary condition (i.e. Fig.6.5), the complex potentials of this problem can be readily obtained as

$$\varphi(\zeta) = -\frac{mRp_{in}}{\zeta}$$ Equation 6-23

$$\psi(\zeta) = -Rp_{in}\frac{(1+m^2)\zeta}{(\zeta^2 - m)}$$ Equation 6-24

Then the stress and displacement components of this problem are expressed in terms of the Kolosoff- Muskhelishvili complex potentials.

$$\sigma_x^e + \sigma_y^e = 4\,\mathrm{Re}[\Phi(\zeta)]$$ Equation 6-25

$$\sigma_y^e - \sigma_x^e + 2i\tau_{xy}^e = 2[\frac{\overline{\omega(\zeta)}}{\omega'(\zeta)}\Phi'(\zeta) + \Psi(\zeta)]$$ Equation 6-26

$$2G(u_x^e + iu_y^e) = [\chi\varphi(\zeta) - \frac{\omega(\zeta)}{\overline{\omega'(\zeta)}}\overline{\varphi'(\zeta)} - \overline{\psi(\zeta)}]$$ Equation 6-27

where σ_x^e , σ_y^e and τ_{xy}^e are elastic stress components, and u_x^e and u_y^e are elastic displacement components; $\mathrm{Re}[\cdot]$ means taking the real part; $\Phi(\zeta) = \frac{\varphi'(\zeta)}{\omega'(\zeta)}$, $\Psi(\zeta) = \frac{\psi'(\zeta)}{\omega'(\zeta)}$; $\chi = 3 - 4\nu$ for a plane strain problem; G is the elastic shear modulus; and 'ν' is Poisson's ratio.

With the small strain assumption in elasticity, the strain components for the plane strain problem can be obtained as follows:

$$\varepsilon_x = \frac{1-\nu}{2G}(\sigma_x - \frac{\nu}{1-\nu}\sigma_y)$$ Equation 6-28

$$\varepsilon_y = \frac{1-\nu}{2G}(\sigma_y - \frac{\nu}{1-\nu}\sigma_x)$$ Equation 6-29

$$\gamma_{xy} = G\tau_{xy}$$ Equation 6-30

By now the elastic stress and deformation fields can be readily calculated with Equation 6.23 to Equation 6.30 by separating their real and imaginary parts. These calculations have all been implemented in Matlab 2013(a) (MathWorks).

6.4.2 Expansion of cylindrical and spherical cavities

When the void becomes circular in shape ($a = b$), the above solution can be directly reduced to the required solution with $m = 0$. Alternatively, solutions both for a cylindrical cavity and a spherical cavity can also be established by solving the equilibrium equation and compatibility equation in linear elasticity. Available solutions can be found in numerous studies e.g. Hill, 1950; Timoshenko and Goodier, 1970; Yu, 2000. For an axisymmetric problem, it is convenient to express the stress and strain components in a cylindrical/spherical polar coordinate system. The solution from Yu (2000) is followed here.

$$\sigma_r = -p(\frac{a}{r})^{1+k}$$ Equation 6-31

$$\sigma_\theta = \frac{1}{k} p(\frac{a}{r})^{1+k}$$ Equation 6-32

$$u_r = r - r_0 = \frac{p}{2kG}(\frac{a}{r})^{1+k} r$$ Equation 6-33

$$\varepsilon_r = \frac{1}{M}[\sigma_r - \frac{k\nu}{1-\nu(2-k)}\sigma_\theta]$$ Equation 6-34

$$\varepsilon_\theta^e = \frac{1}{M}\left\{-\frac{\nu}{1-\nu(2-k)}\sigma_r + [1-\nu(k-1)]\sigma_\theta\right\}$$ Equation 6-35

where $k=1$ for a cylindrical cavity and $k=2$ for a spherical cavity; $M = \frac{E}{1-\nu^2(2-k)}$; E is the elastic modulus; a represent the initial cavity radius.

From the solutions for cylindrical (2D) and spherical (3D) voids we can know that, the value of tensile stress at the edge of the spherical void is half of that for cylindrical voids. Therefore when transforming the plane problem for elliptical (2D) voids to spheroid (3D) voids, the corresponded correction factor is also chosen as half of the plane tensile stress.

Based on the above equations, with given tyre pressure, vehicle velocity and asphalt mixture material properties, the tensile strain around the inner cavity can be calculated.

6.4.3 Different shapes of elliptical voids

As can be seen from Figure 6.2, the shapes of voids are varied and there will be different crack propagation rates associated with different void shapes. Therefore the different shapes need to be classified for a typical asphalt in order to determine the different probabilities of crack propagation rate.

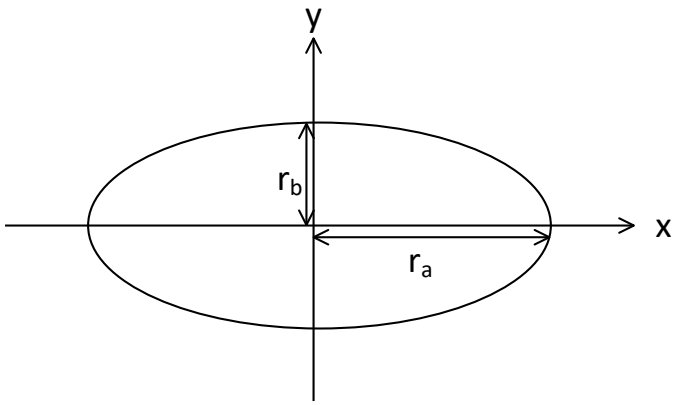

Figure 6-7 Definition of Radius

According to the expansion theory solutions, the stress level is independent of the size of the voids, but relates to the shape of the voids. Hence 19 values of the ratio of x axis radius (r_a) to y axis radius (r_b) (see Figure 6.7) ranging from 0.1 to 10 have been selected to investigate the different shapes of air void, and numbered as 1 to 19 void shape number. These 19 values of r_a to r_b are 0.1, 0.2, 0.3, 0.4, 0.5, 0.6, 0.7, 0.8, 0.9, 1, 1.11, 1.25, 1.43, 1.67, 2, 2.5, 3.33, 5 and 10, respectively (shape number shown in Figure 6.8).

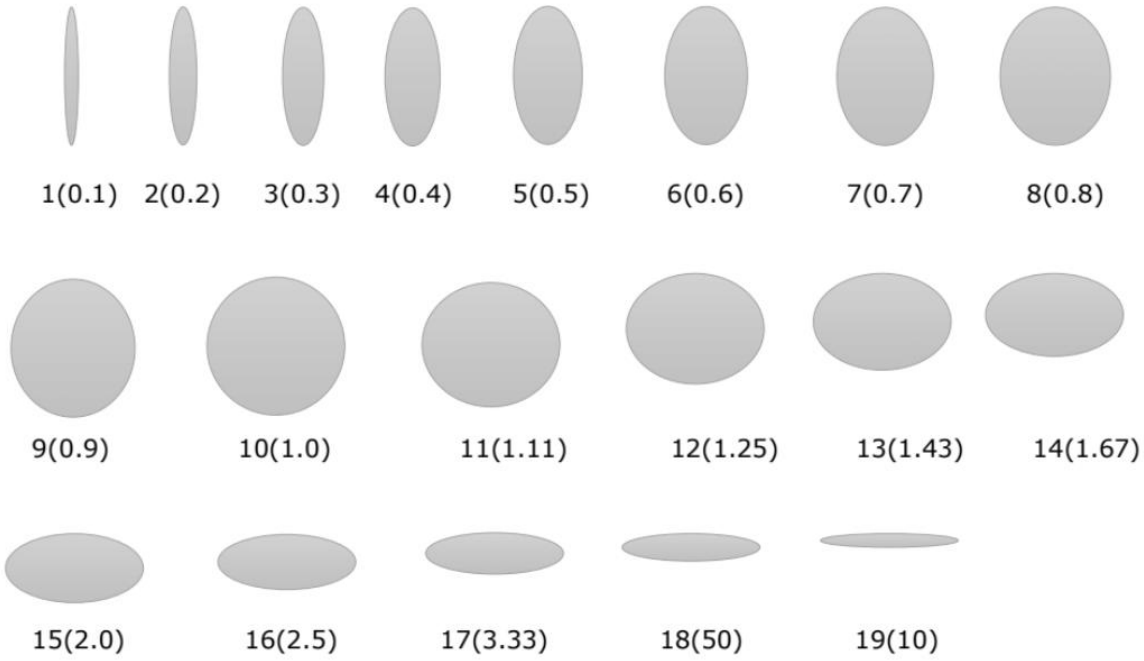

Figure 6-8. Shape number and the related r_a to r_b ratio

Two asphalt specimens with different air voids content (5% and 10%) were analysed. Every visible void in the asphalt specimen has been classified into one of the selected shape numbers according to the ratio of r_a to r_b. After analysis of the two asphalt specimens, a fitted percentage of voids shapes distribution is obtained shown in Figure 6.9. The percentage p_m on the vertical axis for a specific shape m is calculated as the ratio of the number of the voids of this shape to the total number of voids observed in the asphalt specimen.

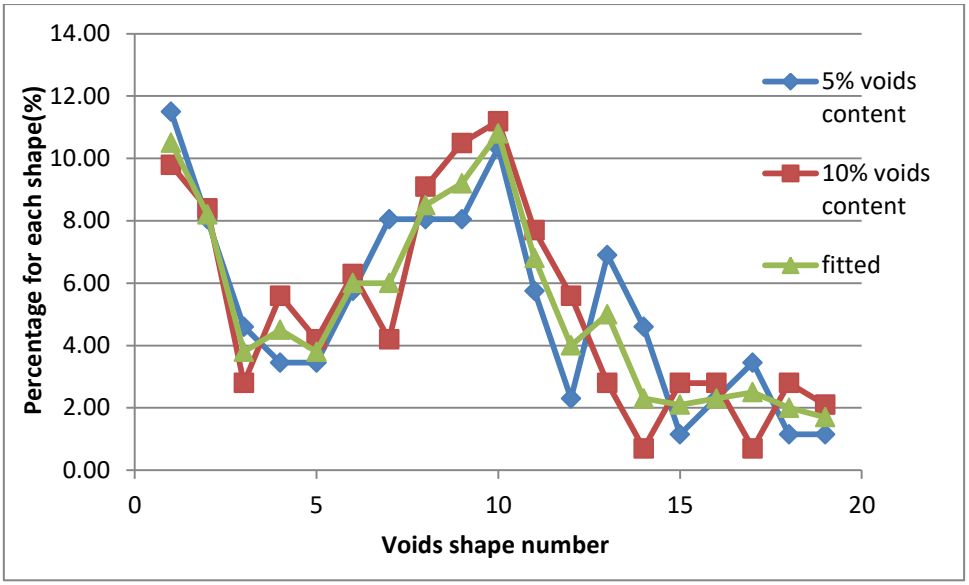

Figure 6-9 Analysed and fitted percentages for different void shapes

However in reality, the orientation of the asphalt is unknown. Therefore to disregard the dependence on an arbitrary x-y system, the number of ellipses having the same ratio of major radius to minor radius are combined together and then evenly distributed to two orthogonal axes. The results are shown below in Figure 6.10.

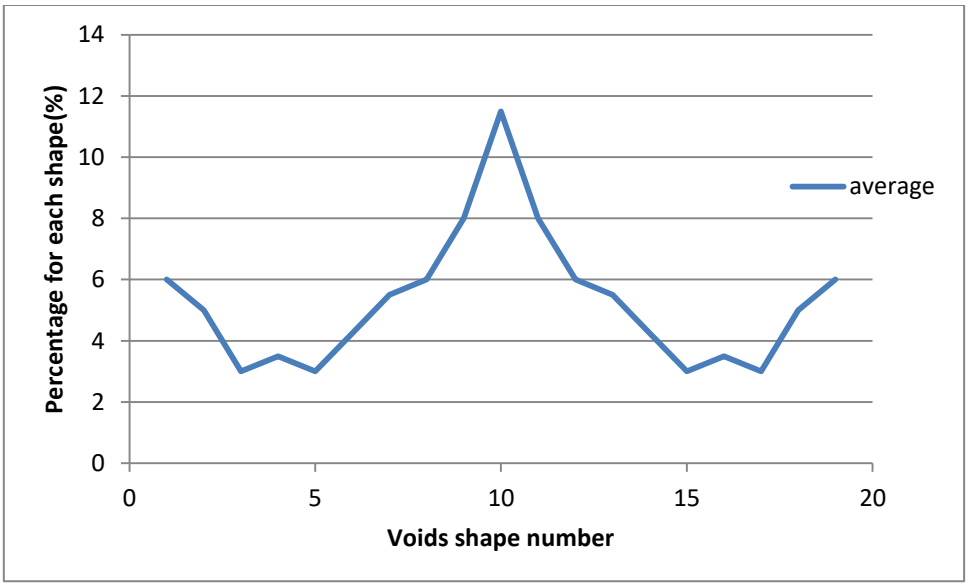

Figure 6-10 Average percentage for each elliptical shape

6.5 Strain-based asphalt crack propagation

According to Equations 25, 26 and 34, the tensile stress at the critical edges of voids with different shapes can be calculated (as seen in Figure 6.11). The water pressure used here is 42.51kPa, which is based on the water pressure in the uppermost voids (0.2mm depth) under 60km/hour vehicle velocity and 1mm protrusion height. Based on the calculations, the edge stress for shape number 17, 18, 19 are negative which means they have been compressed under this water pressure.

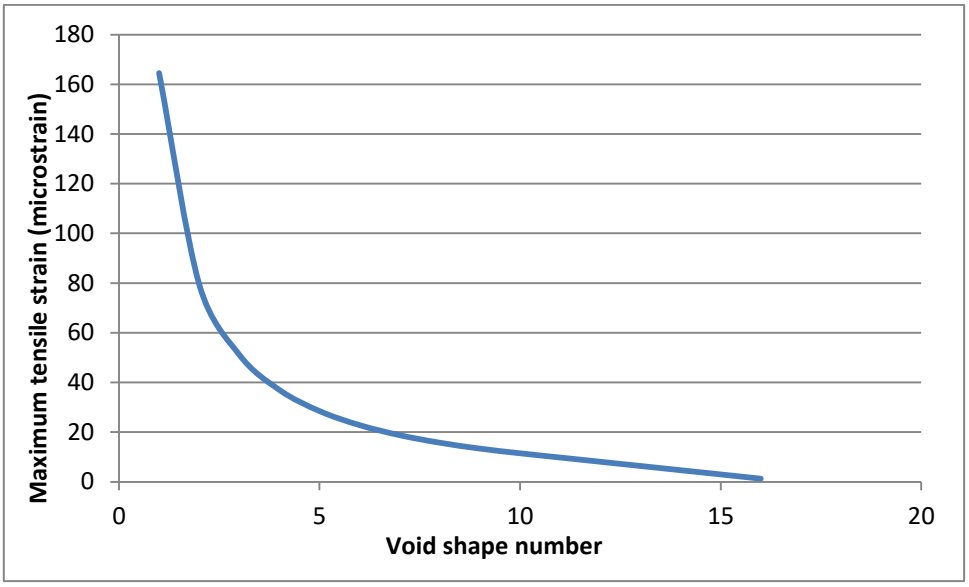

Figure 6-11 Tensile strain at the edge of different voids

Then according to the chosen asphalt cracking propagation law (Equation 11), the crack propagation rate is shown in Figure 6.13 below. The A and n values chosen represent 30/14 HRA. The crack length, shows in Figure 6.12a), assumed here is the distance between the first void and the pavement surface. This corresponds to the ravelling failure on the pavement surface. Moreover, based on the cavity expansion theory, the

tensile strain is only depended on the shape of the voids not on the size of the voids. The crack growth is assumed to be same over the voids as increasing the voids size, therefore, same strain applies as the crack growth.

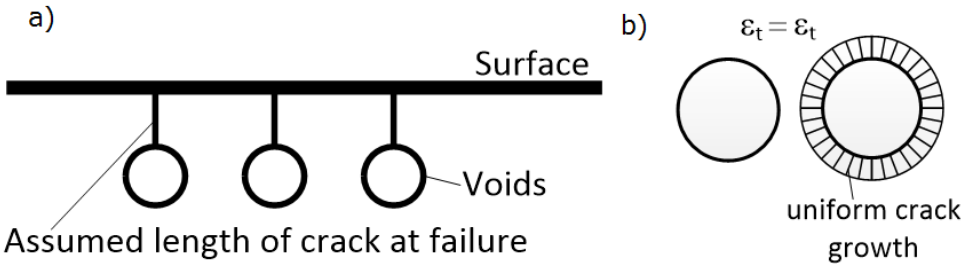

Figure 6-12 a) Definition of crack length; b) crack growth with equal tensile strain at the edge

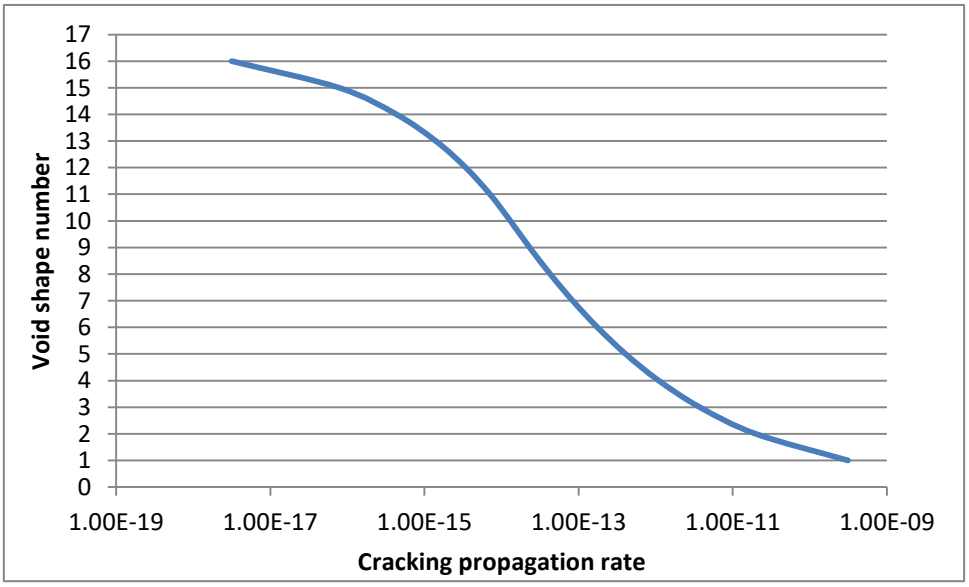

Figure 6-13 Cracking propagation rate under 3D conditions

So for a given crack length to failure, the estimated life can be determined from the crack propagation rates shown in the above figure.

6.6 Results and discussion

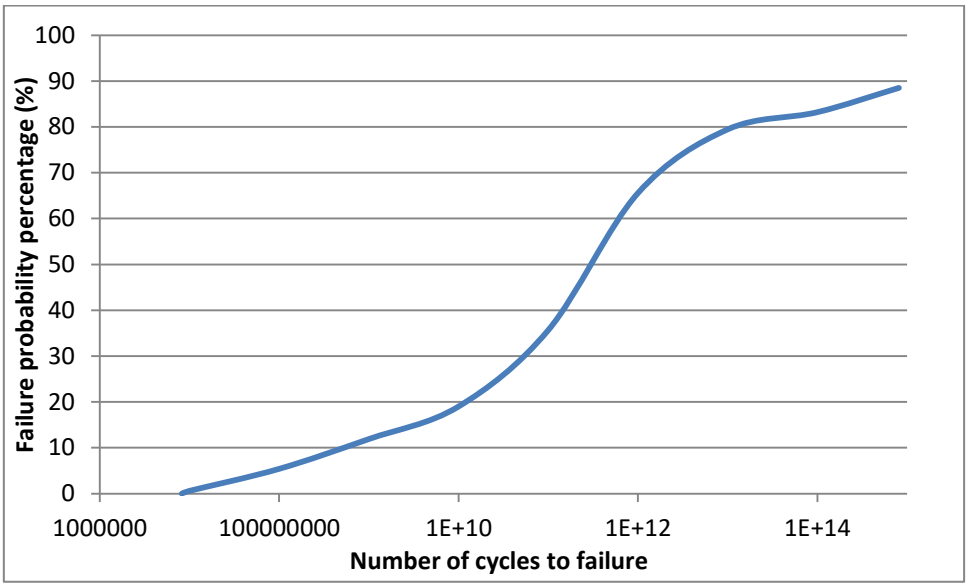

Figure 6-14 Failure probability curve

A significant goal of this research was to obtain a failure probability curve, an example of which is shown in Figure 6.14 (based on the SMA type shown in Table 6.3). The following shows step by step calculations for the failure probability at 10000000 cycles. First the crack length to failure needs to be defined. In this case, it is assumed to be 0.2mm. With the calculated crack propagation rate the number of cycles to failure for each void shape is determined and shown in Figure 6.15.

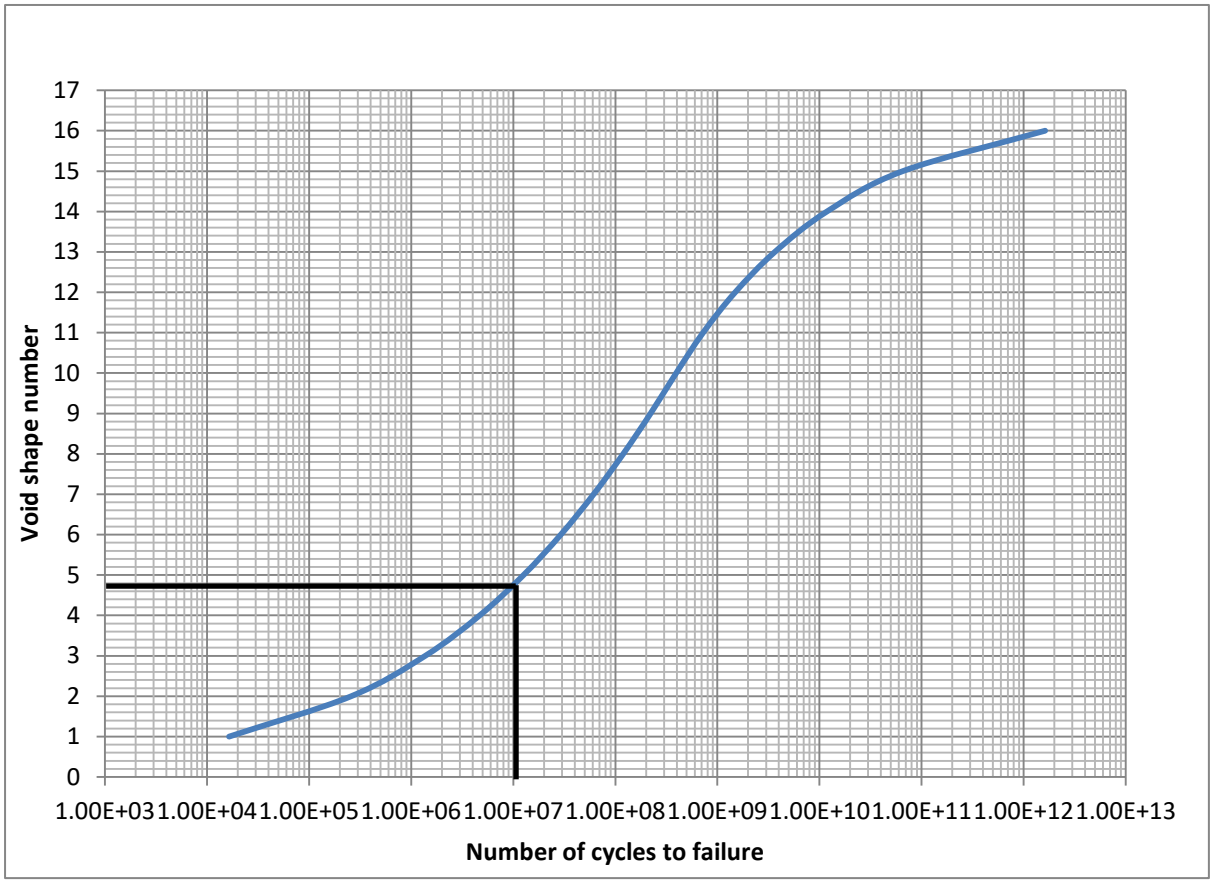

Figure 6-15 Failure life for each shape

To determine the failure probability percentage P_f as a function of the number of cycles to failure N, several values of N were selected and the corresponding P_f values were calculated as follows:

$$\mathrm{P}_f(\mathrm{N}) = \sum_{i=1}^{m} n_i p_i \qquad \text{Equation 6-36}$$

where m is the maximum number of shape corresponding to the number of cycles N; p_i is the percentage of the void number shown in Figure 6.8; n_i ranges from 0 to one and represents the percentage of damage to the i shape void number. An example is given in Figure 6.15 for calculations of P_f corresponding to $\mathrm{N} = 1e^7$. In the first step, a vertical straight line of $\mathrm{N} = 1e^7$ is plotted. Then, the intersection of the vertical straight line and

the failure life curve in Figure 6.15 is marked. A horizontal straight line is plotted, crossing the intersection. Under this horizontal straight line, the maximum void shape number $\mathrm{m} = 4$ is read, and the vertical coordinate of the horizontal line $\mathrm{y} = 4.8$. When subjected to the number of cycles $\mathrm{N} = 1e^7$, 100% of the void shapes 1, 2 and 3 would be damaged, and therefore, n_1, n_2 and n_3 are all equal to 100%. For the void shape number 4, the percentage of damage is simply calculated as $y - m$, i.e. $n_4 = 80\%$. As a result, $\mathrm{P}_f(\mathrm{N} = 1e^7) = 100\% \times p_1 + 100\% \times p_2 + 100\% \times p_3 + 80\% \times p_4$.

Repeat the stated procedure for other numbers of cycles, and then the failure probability curve can be obtained.

Therefore for a given material, the probability of failure can be estimated using this procedure.

Probability of failure before a certain number of cycles (N) is derived numerically by summing the probabilities of those void shapes that give life lower than N.

Therefore for a given material, the probability of failure can be estimated using this procedure.

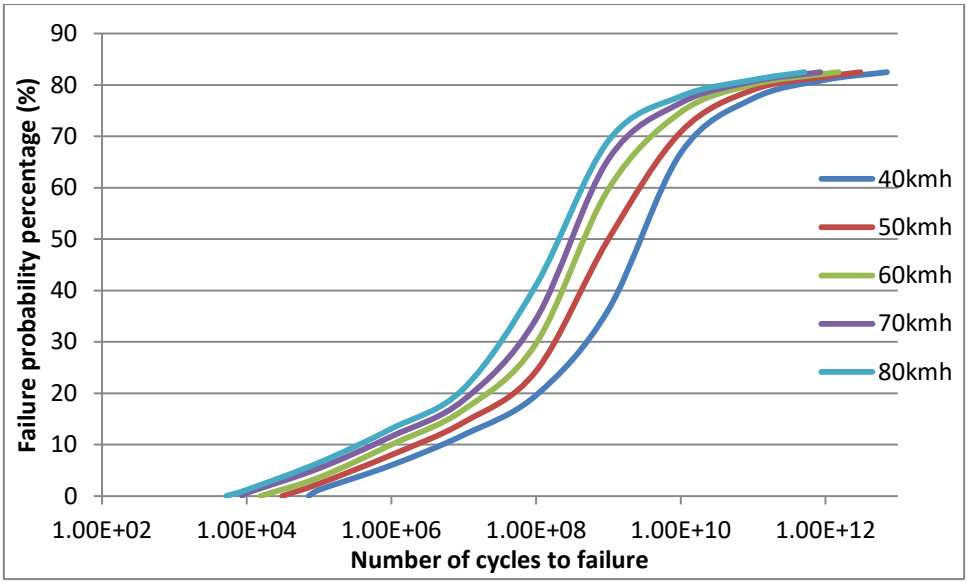

Figure 6-16 Comparison of probability for different vehicle velocities

Figure 6.16 shows the failure percentages for the same material (SMA) using the same input parameters (material, protrusion height, permeability, total air voids content, voids size and crack length which is the the distance to the surface rather than the initial crack lengths) through the calculations apart from differing vehicle velocities. It can be seen that high vehicle velocity gives a shorter life with a significant changings to failure at the same failure probability percentage.

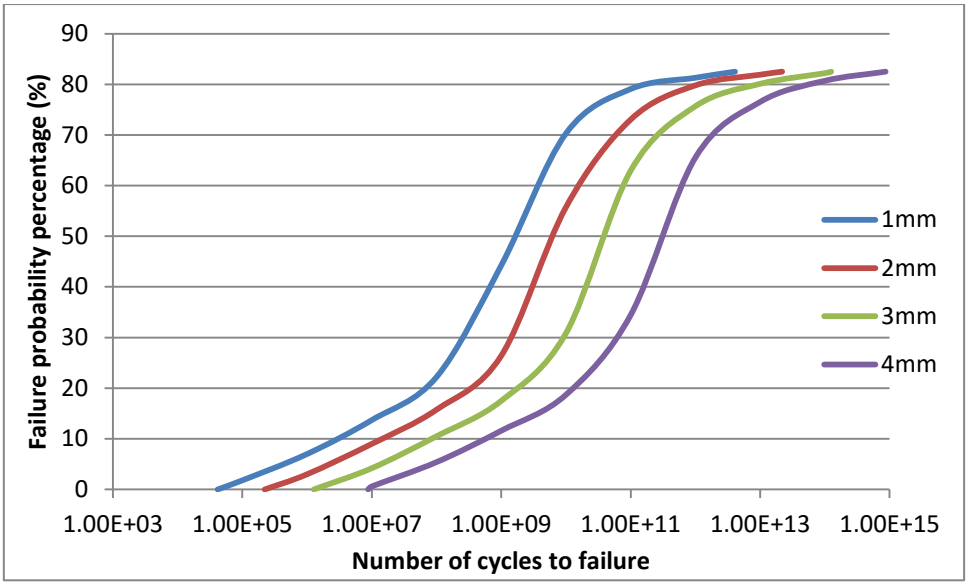

Figure 6-17 Comparison of probability for different protrusion heights

The results shown in Figure 6.17 show the effect of protrusion height while the values of other parameters (vehicle velocity, permeability, total air voids content, voids size, crack length and material) remain the same. It is worth mentioning that the protrusion height is closely related to textured depth (approximant equals to $h_p \times (1-n_2)$ (see explanations for the parameters h_p and n_2 in chapter 4.2.1)) which affects the skid resistance and noise of the road. Compared to the influence of vehicle velocity, the influence of protrusion height is much more significant. The number of cycles to failure at the same failure probability percentage due to surface water pressure increases as the protrusion height (texture depth) increasing.

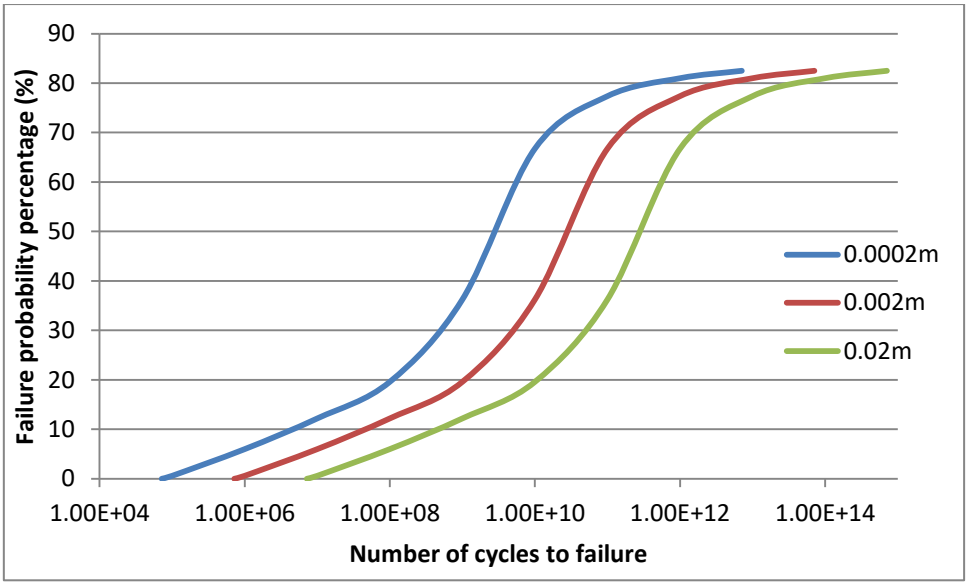

Figure 6-18 Comparison of probability for different crack lengths

Figure 6.18 indicates the failure life for different crack lengths under the same environmental conditions (vehicle velocity, protrusion height, permeability, total air voids content, voids size and material). It can be seen that the ratio of number of cycles to failure equals the ratio of crack length at the same failure probability percentage. However this is due to the assumption that the strain in the crack tip area doesn't change as the crack growth in the cavity expansion theory with a long way from the surface. Although this assumption is crude when the crack approaches the surface, it was used here for simplicity. Further study is required to identify a more appropriate model to simulate realistically the crack propagation near the pavement surface.

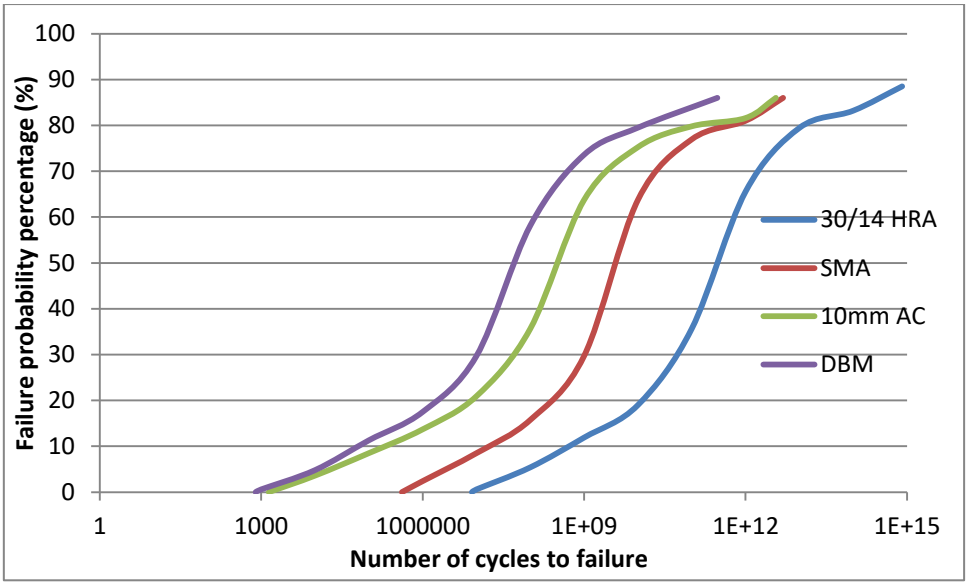

Figure 6-19 Comparison of probability for different asphalt surfaces

Figure 6.19 shows the probability of failure for different asphalt surfaces under the same environmental conditions (vehicle velocity, protrusion height, permeability, total air voids content, voids size and crack length), with the same water pressure assumption. In this case, with the chosen input parameters, this indicates that 30/14 HRA is the best among these four asphalt pavement types followed by SMA, 10mm AC and 20mm DBM, which ties in with UK experience that HRA can last a long time without apparent surface distress. In this prediction, the initiation of cracking occurs after about 10 million load applications for 30/14 HRA which is about 10 times that for SMA. However SMA is cheaper compared to HRA, and it has other useful properties such as relatively good rut resistance, making it popular in the UK (Xue et al. 2009). The performances of AC and DBM are very similar, and they have a considerably poorer performance compared to 30/14 HRA and SMA with respect to crack propagation. AC appears to fail fully at a similar number of load

applications to SMA and has a similar number of load applications for crack initiation to DBM.

6.7 Summary

Two main subjects have been presented in this chapter. The first was to present a method to calculate the loss of bitumen-aggregate adhesion. And this can be extended to calculate the de-bonding between asphalt layers. The calculations gave an insight into the de-bonding mechanism of bitumen to aggregate adhesion and bond strength between layers. The adhesion between bitumen to aggregate is easier to failure under this mechanism compared to the bond strength between asphalt layers. The second subject was to obtain the probability of failure using the parameters calculated in the previous chapters and from the material properties. By changing the different parameters in the calculations, the probability for a large range of asphalt mixtures (like those shown in Figure 6.18) can be defined and compared which can give an idea of how the material will behave in reality.

Chapter 7. Conclusion and recommendations

This chapter contains a brief summary of the research process and major conclusions from the research. Recommendations for future research are also included in this chapter.

7.1 Summary

Moisture damage is recognised as one of the major causes of asphalt pavement deterioration. During its service life, the presence of water can lead to loss of stiffness and strength of an asphalt pavement structure. Apart from that, the presence of water can accelerate the propagation and severity of already existing distress. Fatigue is also considered as one major cause of asphalt pavement distress. It is caused by tensile strains generated in the pavement not only by traffic loading but also by temperature variations and construction practices.

In this research, a series of computer simulations has been developed to model the deterioration process of a pavement under the combination of moisture and fatigue influence in order to predict pavement performance. The first task was to calculate the pavement surface water pressure under a moving tyre. Then the asphalt pavement internal structure (voids distribution) was determined and the water pressure distribution inside pavement structure calculated using the surface water pressure. A ravelling failure probability line was predicted with the help of cavity expansion theory and an asphalt crack propagation law. This simulation

can be used to predict the performance of a specific asphalt mixture by changing the input parameters.

7.2 Conclusions

Conclusions drawn from this research are as follows:

From the site observations, the conclusion that turning and braking can accelerate pavement distress deterioration can be drawn. And severe ravelling and alligator cracking will result in the formation of potholes. In general, evidence from the site observations and literature indicates a strong link between both ravelling ad other forms of surface break-up and both traffic and water effects.

The textured pavement surface assumption gives a reasonably realistic prediction compared to that of a perfectly smooth surface. The results show that the peak water pressure increases with increasing vehicle velocity or reducing textured depth. The permeable pavement surface results indicate that the permeability of the asphalt surface has a secondary effect on the surface water pressure.

There is a significant decrease of water pressure inside an asphalt layer when the voids are partially saturated compared to the fully saturated condition. Moreover the water pressure drops more quickly near to the surface than at depth for partially saturated voids.

A simplified calculation was developed to evaluate the bond strength between bitumen-aggregate and the interlayer bond strength. This method indicates that the adhesion between bitumen to aggregate is easier to fail compared to the bond strength between asphalt layers.

The case study for the performance of four different asphalt types (HRA, SMA, AC, DBM) using the failure probability calculation shows a good correspondence with their real performance, which indicates that this process of predicting failure probability is generally acceptable.

7.3 Recommendations for future work

The proposed simulations capture the moisture, traffic and fatigue influence on pavement deterioration and have the ability to predict pavement performance, but some limitations still exist and should be studied further. Key recommendations for future research are discussed below:

- The tyre vertical velocity equation used in chapter 4 was converted from the indentation velocity at 100km/hour vehicle velocity only. In order to have a more realistic result, the tyre vertical velocity equation needs to be modified using more sources at different vehicle velocities.
- In reality, tyres are designed with different types of tread, each of which is meant for different road conditions and driving styles. Only

a uniform simplified tyre tread shape was used in the simulations. Other tread shapes may also need to be modelled.

- When calculating the water flow into a permeable material, the flow was transformed from 3D to 2D format which resulted in a rather small flow volume. Some other approaches should be tried to confirm the results.
- For the assumption of asphalt internal structure, the tubes and voids were assumed to be vertically connecting and uniformly distributed. However, the tubes and voids may connect in any direction, and they are not evenly distributed. A more realistic order (i.e. more voids at top and bottom of asphalt layer) of voids distribution can be added together with some horizontally connected tubes and voids.
- The assumption that the strain in the crack tip area does not change as the crack growth in the cavity expansion theory with a long way from the surface is crude when the crack approaches the surface. Further study is required to identify a more appropriate model to simulate realistically the crack propagation near the pavement surface.
- To validate the predictions, a long-term pavement performance analysis program will be needed. A laboratory or field pore pressure test needs to be conducted. However this has been found to be difficult. Several laboratory tests have been tried by the author and

another researcher, but no meaningful results or conclusions have get been obtained.

Reference

Abdulshafi, A. A., and Kamran Majidzadeh, 1985. "J-integral and cyclic plasticity approach to fatigue and fracture of asphaltic mixtures." Transportation Research Record 1034 .

Aboufoul, M., 2015. Private communication.

Airey, G.D., Singleton, T.M. and Collop, A.C., 2002. Properties of polymer modified bitumen after rubber-bitumen interaction. journal of materials in civil engineering, 14(4), pp.344-354.

Annual Local Authority Road Maintenance(ALARM) Survey, 2016. http://www.asphaltindustryalliance.com/images/library/files/ALARM%202016/ALARM_survey_2016_full_report.pdf

Al Omari, A. A. M. (2005). Analysis of HMA permeability through microstructure characterization and simulation of fluid flow in X-ray CT images (Doctoral dissertation, Texas A&M University).

Alvarez, A.E., Macias, N. and Fuentes, L.G., 2012. Analysis of connected air voids in warm mix asphalt. Dyna, 79(172), pp.29-37.

Aschenbrener T., 1995. Evaluation of Hamburg wheel-tracking device to predict moisture damage in hot-mix asphalt. Transportation Research Record, 1492: 193-201.

Ascher, D., Wellner, F., 2007. Investigation of the effectiveness of bonding and its influence on the service life of asphalt pavements. Technical University of Dresden, Germany, Report No. 13589 BR/1.pp.100.

Asphalt Industry Alliance, 2016. Annual Local Authority Road Maintenance Survey. London.

Baker, J.J., 2012. Cracking performance of asphalt mixtures containing taconite tailings using traditional and multiple freeze-thaw moisture conditioning methods (Doctoral dissertation, UNIVERSITY OF MINNESOTA).

Baladi, G.Y., Schorsch, M. and Svasdisant, T., 2003. Determining the causes of top-down cracks in bituminous pavements (No. RC-1440).

Bernhard, R., Wayson, R.L., Haddock, J., Neithalath, N., El-Aassar, A., Olek, J., Pellinen, T. and Weiss, W.J., 2005. An introduction to tire/pavement noise of asphalt pavement. Institute of Safe, Quiet and Durable Highways, Purdue University.

Biczysko, S., Taggart, A.,Gibb, M., Walsh, C., Leckie, S., 2010. Research Project 79 – Potholes and Repair Techniques for Local Authorities. ATKINS, UK, pp.7-46.

Bocci M. and Colagrande S., 1993. The adhesiveness of modified road bitumen. Proceeding of the 5th Eurobitumen Congress, Vol 1A, Stockholm.

Bonnaure, F., Gravois, A. and Udron, J., 1980. A new method for predicting the fatigue life of bituminous mixes. In Association of Asphalt Paving Technologists Proceedings (Vol. 49).

Buttlar, W.G. and Roque, R., 1994. Development and evaluation of the strategic highway research program measurement and analysis system for indirect tensile testing at low temperatures. Transportation Research Record, (1454).

Chabot, A., Hammoum, F. and Hun, M., 2016. Mixed-mode debonding approach to evaluate water sensibility in bi-layer composite pavement. In8th RILEM International Conference on Mechanisms of Cracking and Debonding in Pavements (pp. 613-618). Springer Netherlands.

Chang, K.J., Wu, H.C., 1980. Angled elliptic notch problem under biaxial loading. Journal of Applied Mechanics 47, 57-63.

Charmot, S., Romero, P. and Dunning, M., 2005. Forensic analysis of slippage cracking. In Proceeding of the 84th TRB annual meeting. Washington (DC), USA.

Choquet F. and Verhasselt A., 1993. An objective method of measuring bitumen-aggregate adhesion-the boiling water stripping test. Proceeding of the 5th Eurobitumen Congress, Stockholm.

Cocurullo, A., Airey, G.D., Collop, A.C. and Sangiorgi, C., 2008, November. Indirect tensile versus two-point bending fatigue testing. In Proceedings of the Institution of Civil Engineers-Transport (Vol. 161, No. 4, pp. 207-220). Thomas Telford Ltd.

Collop, A., and Cebon, D.,(1995), "A Theoretical Analysis of Fatigue Cracking in Flexible Pavements", Proceedings of the Institution of Mechanical Engineers. Part C, Vol-209, No. 5, pp. 345-361.

Collop, A.C., Sutanto, M.H., Airey, G.D. and Elliott, R.C., 2009. Shear bond strength between asphalt layers for laboratory prepared samples and field cores. Construction and Building Materials, 23(6), pp.2251-2258.

Cooley, L.A., Prowell, B.D. and Brown, E.R., 2002. Issues pertaining to the permeability characteristics of coarse-graded Superpave mixes. ASPHALT PAVING TECHNOLOGY, 71, pp.1-29.

Copeland, A.R., 2007. Influence of moisture on bond strength of asphalt-aggregate systems (Doctoral dissertation, Vanderbilt University).

Cox, B., 1978. Pavement maintenance management. Developments in Highway Pavement Engineering-2, pp. 115-157

CROW(2000),"Standard RAW Requirements", C. R. O. W., Ede (in Dutch).

CUI, X.Z. and JIN, Q., 2008. The dynamic response of saturated asphalt pavement under wheel loads [J]. Journal of Shandong University (Engineering Science), 5, p.006.

Dawson, A. ed., 2008. Water in road structures: movement, drainage & effects (Vol. 5). Springer Science & Business Media.

England, A.H., 2003. Complex variable methods in elasticity. Dover Publications, Inc, Mineola, New York.

Federal Highway Administration (FHWA).2009.Pavement Distress Identification Manual for the NPS Road Inventory Program, USA.pp.4-30. [URL: http://www.wistrans.org/mrutc/files/Distress-ID-Manual.pdf]

Garber, N.J. and Hoel, L.A., 2014. Traffic and highway engineering. Cengage Learning.

Griffith, A.A., 1921. The phenomena of rupture and flow in solids. Philosophical transactions of the royal society of london. Series A, containing papers of a mathematical or physical character, 163-198.

Hachiya, Y. and Sato, K., 1997. Effect of tack coat on binding characteristics at interface between asphalt concrete layers. In Eighth International Conference on Asphalt Pavements (No. Volume I).

Hakim, B.A., 2002, August. The importance of good bond between bituminous layers. In Ninth International Conference on Asphalt Pavements.

Hamed, F.K.M., 2010. Evaluation of fatigue resistance for modified asphalt concrete mixtures based on dissipated energy concept.

Hassan, N.A., Airey, G.D. and Hainin, M.R., 2014. Characterisation of micro-structural damage in asphalt mixtures using image analysis. Construction and Building Materials, 54, pp.27-38.

Hefer, A.W., Little, D.N. and Lytton, R.L., 2005. A synthesis of theories and mechanisms of bitumen-aggregate adhesion including recent advances in quantifying the effects of water. Journal of the association of asphalt paving technologists, 74, pp.139-196.

Hill, R., 1950. The mathematical theory of plasticity. Oxford University Press, London.

http://www.potholes.co.uk/

IAT, 2000. IAT. Asphalt professionals in the 21st century. The Institute of Asphalt Technology, 2000.

Inglis, C.E., 1913. Stresses in a plate due to the presence of cracks and sharp corners. Spie Milestone series MS 137, 3-17.

Jacobs, M. M. J., P. C. Hopman, and A. A. A. Molenaar, 1996. "Application of fracture mechanics principles to analyze cracking in asphalt concrete (with discussion)." Journal of the Association of Asphalt Paving Technologists 65.

Kandhal, P.S., 1992. Moisture susceptibility of HMA mixes: identification of problem and recommended solutions (No. NCAT 92-1,). National Asphalt Pavement Association.

Kandhal, P.S., 1994. Field and laboratory investigation of stripping in asphalt pavements: State of the art report. Transportation Research Record, (1454).

Kanitpong, K. and Bahia, H.U., 2003. Role of adhesion and thin film tackiness of asphalt binders in moisture damage of HMA. In Association of Asphalt Paving Technologists Technical Sessions, 2003, Lexington, Kentucky, USA (Vol. 72).

Kennedy, T.W., 1977. Characterization of asphalt pavement materials using the indirect tensile test. In Association of Asphalt Paving Technologists Proc (Vol. 46)

Kennedy, T.W., Roberts, F.L. and Lee, K.W., 1982. Evaluation of moisture susceptibility of asphalt mixtures using the Texas freeze-thaw pedestal test. In Association of Asphalt Paving Technologists Proceedings (Vol. 51).

Khodary Moalla Hamed, F., 2010. Evaluation of fatigue resistance for modified asphalt concrete mixtures based on dissipated energy concept(Doctoral dissertation, TU Darmstadt).

Kiggundu, B.M. and Roberts, F.L., 1988. Stripping in HMA mixtures: State-of-the-art and critical review of test methods (No. NCAT Report No. 88-2). Auburn, AL: National Center for Asphalt Technology.

Kim, Y.R. and Lutif, J.S., 2006. Material selection and design consideration for moisture damage of asphalt pavement (No. P564). University of Nebraska-Lincoln.

Kringos, N., 2005. Simulation of combined mechanical-moisture induced damage in asphaltic mixes. In International Workshop on Moisture Induced Damage of Asphaltic Mixes.

Kringos, N., 2007. Modeling of combined physical-mechanical moisture induced damage in asphaltic mixes (Doctoral dissertation, TU Delft, Delft University of Technology).

Kringos, N., Scarpas, A. and Kasbergen, C., 2007. Three Dimensional Elasto-Visco-Plastic Finite Element Model for Combined Physical-Mechanical Moisture Induced Damage in Asphaltic Mixes (With Discussion). Journal of the association of asphalt paving technologists,76.

Liljedahl, B., 1992. Mix design for heavy duty asphalt pavements. The Asphalt Yearbook 1992, pp.18-24.

Liu, Y., Apeagyei, A., Ahmad, N., Grenfell, J. and Airey, G., 2014. Examination of moisture sensitivity of aggregate–bitumen bonding strength using loose asphalt mixture and physico-chemical surface energy property tests. International Journal of Pavement Engineering,15(7), pp.657-670.

Lottman R.P., 1982. Laboratory test methods for predicting moisture-induced damage to asphalt concrete, Transportation Research Record, 843: 88-95.

Lu, Q. and Harvey, J.T., 2007. Inclusion of moisture effect in fatigue test for asphalt pavements. In Transportation Research Board 86th Annual Meeting (No. 07-2060).

Lytton, R.L., Masad, E.A., Zollinger, C., Bulut, R. and Little, D.N., 2005.Measurements of surface energy and its relationship to moisture damage(No. FHWA/TX-05/0-4524-2).

Majidzadeh, K. and Brovold, F.N., 1968. State of the art: Effect of water on bitumen-aggregate mixtures. Highway Research Board, National Research Council.

Majidzadeh, K., E. M. Kauffmann, and D. V. Ramsamooj, 1971. "Application of fracture mechanics in the analysis of pavement fatigue." Association of Asphalt Paving Technologists Proc. Vol. 40..

Mansura D., 2015, A Novel Multi-Scale Numerical Model for Prediction of Texture-Related Impacts on Fuel Consumption

Masad, E., Jandhyala, V.K., Dasgupta, N., Somadevan, N. and Shashidhar, N., 2002. Characterization of air void distribution in asphalt mixes using X-ray computed tomography. Journal of materials in civil engineering, 14(2), pp.122-129.

Mathews D.H. and Colwill D. M, 1962. The immersion wheel-tracking test. Journal of Applied Chemistry: 505-509.

Matsuno, and Nishizawa, T., (1992),"Mechanism of Longitudinal Surface Cracking in Asphalt Pavement",Proceedings of 7th International Conference on Asphalt Pavements, Vol-2, pp. 277-291.

Maugis, D., 1992. Stresses and displacements around cracks and elliptical cavities: exact solutions. Engineering fracture mechanics 43, 217-255.

Michigan Department of Transportation (MDOT), 2011. www.michigan.gov/mdot/potholes

Miner, M.A., 1945. Cumulative damage in fatigue. Journal of applied mechanics, 12(3), pp.159-164.

Monismith, C. L., 1992. Analytically Based Asphalt Pavement Design and Rehabilitation. Transportation Research Record 1354, Transportation Research Board, Washington, D.C., pp 5-26

Muench, S.T., Moomaw, T. and Trainer, R.C., 2008. De-bonding of hot mix asphalt pavements in Washington State: an initial investigation (No. WA-RD 712.1). Washington State Department of Transportation, Office of Research & Library Services.

Muslich, S., 2010. Assessment of bond between asphalt layers (Doctoral dissertation, University of Nottingham).

Muskhelishvili, N.I., 1963. Some basic problems of the mathematical theory of elasticity (4th Ed.). P. Noordhoff, Groningen, Netherlands.

Naveed Ahmad, 2011. Asphalt Mixture Moisture Sensitivity Evaluation using Surface Energy Parameters, PhD Thesis, University of Nottingham, Nottingham, UK, pp.1-36.

Paris, P.C., Gomez, M.P. and Anderson, W.E., 1961. A rational analytic theory of fatigue. The trend in engineering, 13(1), pp.9-14.

Pell, P.S. and Cooper, K.E., The effect of testing and mix variables on the fatigue

Perdomo, D., and Nokes, B.,(1993), "Theoretical Analysis of the Effects of Wide-Base Tires on Flexible Pavement Using CIRCLY", Transportation Research Record 1388, Transportation Research Board (TRB), (Washington D.C.), 108-119.

Performance of bituminous materials, Annual Meeting of AAPT, Phoenix, Arizona (1975).

Raab, C. and Partl, M.N., 2004. Interlayer shear performance: experience with different pavement structures. In PROCEEDINGS OF THE 3RD EURASPHALT AND EUROBITUME CONGRESS HELD VIENNA, MAY 2004(Vol. 1).

Raab, C., Partl, M.N. and Abd El Halim, A.O., 2012, August. Effect of moisture on interlayer bonding of asphalt pavements. In Seventh International Conference on Maintenance and Rehabilitation of Pavements and Technological Control (No. 00055).

Rababaah, H., Vrajitoru, D. and Wolfer, J., 2005, June. Asphalt pavement crack classification: a comparison of GA, MLP, and SOM. In Proceedings of Genetic and Evolutionary Computation Conference, Late-Breaking Paper.

Read, J.M., 1996. Fatigue cracking of bituminous paving mixtures (Doctoral dissertation, University of Nottingham)

Read, J. and Whiteoak, D., 2003. The shell bitumen handbook. Thomas Telford.

Rodrigues, R.M., 2000. A model for fatigue cracking prediction of asphalt pavements based on mixture bonding energy. International Journal of Pavement Engineering, 1(2), pp.133-149.

Santucci. L, 2002. Moisture Sensitivity of Asphalt Pavements: technology transfer program. Institute of Transportation Studies, UC Berkeley Institute of Transportation Studies, USA.

Savin, G.N., 1970. Stress distribution around holes. National Aeronautics and Space Administration, Washington, D.C.

Schultz J. and Nardin M. Theories and mechanisms of adhesion. In A. Pizzi and K.L. Mittal (Eds.), Handbook of Adhesive Technology. New York: Marcell Dekker, Inc. 1994.

Shaat, A.A., 1992. Investigation of slippage of bituminous layer in overlaid pavement in Northern Ireland. Consultancy Report Submitted for the DOE in Northern Ireland, Belfast, UK.

Shen, S. and Carpenter, S., 2007. Development of an asphalt fatigue model based on energy principles. Asphalt Paving Technology-Proceedings, 76, p.525.

Sorum, N. G., Guite, T., & Martina, N. (2013). Pavement distress: a case study. International Journal of Innovation Research in Science, Engineering and Technology, 3(4), 274-284.

Stevenson, A.C., 1945. Complex potentials in two-dimensional elasticity. Proceedings of the Royal Society of London. Series A. Mathematical and Physical Sciences 184, 129-179.

Sutanto, M.H., 2009. Assessment of bond between asphalt layers.Nottingham: University of Nottingham.

Svasdisant, T., Achorsch, M., Baladi, G.Y. and Pinyosunun, S**.,** 2002. Mechanistic Analysis of Top-Down Cracking in Asphalt Pavements. 81st

Transportation Research Board Annual Meeting. Proceedings CD-Room. Washington D.C..

Tashman, L., Masad, E., D'Angelo, J., Bukowski, J. and Harman, T., 2002. X-ray tomography to characterize air void distribution in superpave gyratory compacted specimens. International Journal of Pavement Engineering, 3(1), pp.19-28.

Taylor, M.A. and Khosla, N.P., 1983. Stripping of asphalt pavements: State of the art (discussion, closure) (No. 911).

Thom, N., 2006. Asphalt cracking: a Nottingham perspective. Engenaria Civil/Civil Engineering, 26, pp.75-84.

Thom, N., 2008. Principles of pavement engineering.

Timoshenko, S.P., Goodier, J.N., 1970. Theory of elasticity (3rd Ed.). McGraw-Hill, Inc., London.

Tom, V.M. and Krishna Rao, K.V., 2007. Introduction to transportation engineering. Marshall mix design, national programme on technology enhanced learning (NPTEL), Indian Institute of Technology, India.

Traffic counts reports from UK government department of transport: http://www.dft.gov.uk/traffic-counts/cp.php?la=Nottingham#57924

Tunnicliff, D.G. and Root, R.E., 1982. ANTISTRIPPING ADDITIVES IN ASPHALT CONCRETE--STATE-OF-THE-ART 1981. In Association of Asphalt Paving Technologists Proceedings (Vol. 51).

Tunnicliff D.G. and Root R.E, 1984. Use of antistripping additives in asphalt concrete mixtures, NCHRP 274, Transportation Research Board, Washington DC.

Vuorinen M.J. and Valtonen J.P., 1999. A New Ultrasonic Method for Measuring the Resistance to Stripping, Proceeding of the Eurobitumen Workshop 99, Paper No. 023, Luxembourg.

Walsh G., Jamieson I., Thornton J. and O"Mahony M., 1996. A modified SHRP net adsorption test. Proceeding of Eurosphalt & Eurobitumen Congress, Starsbourg.

White, F.M., 1999. Fluid mechanics, WCB. ed: McGraw-Hill, Boston.

Whiteoak D. The Shell Bitumen Handbook. Thomas Telford, 1991.

Xue, Y., Hou, H., Zhu, S. and Zha, J., 2009. Utilization of municipal solid waste incineration ash in stone mastic asphalt mixture: pavement performance and environmental impact. Construction and Building Materials, 23(2), pp.989-996.

Yu, H.S., 2000. Cavity expansion methods in geomechanics. Kluwer Academic Publishers, The Netherlands.

Zhang, J., Apeagyei, A.K., Airey, G.D. and Grenfell, J.R., 2015. Influence of aggregate mineralogical composition on water resistance of aggregate–bitumen adhesion. International Journal of Adhesion and Adhesives, 62, pp.45-54.

Zhang, J., 2016. Moisture damage of aggregate-bitumen bonds (Doctoral dissertation, University of Nottingham).